X-ray properties of NGC 300 point sources detected with *XMM-Newton* and their optical counterparts

Dissertation
zur Erlangung des Grades eines
Doktors der Naturwissenschaften
der Fakultät für Mathematik und Physik
der Eberhard Karls Universität Tübingen

vorgelegt von

Stefania Carpano

aus Etterbeek (Brüssel)
2006

Tag der mündlichen Prüfung:	8 März 2006
Dekan:	Prof. Dr. Schmid
1. Berichterstatter:	Priv.-Doz. Dr. J. Wilms
2. Berichterstatter:	Prof. Dr. Klaus Werner

Abstract

Studies of the X-ray population of spiral galaxies other than our Galaxy are of importance especially for the understanding of X-ray binaries and other X-ray emitting sources. The X-ray population of spiral galaxies is mainly composed of supernova remnants (SNRs), low-mass X-ray binaries (LMXBs), high-mass X-ray binaries (HMXBs), and other sources for which the nature is still not clear. The latter are mainly supersoft sources (SSSs), characterized by very soft spectra and luminosities in the range of 10^{36}–$10^{39}\,\mathrm{erg\,s^{-1}}$, and ultraluminous X-ray sources (ULXs), characterized by a luminosity $>10^{39}\,\mathrm{erg\,s^{-1}}$.

In this thesis, I study the X-ray population of the nearby spiral galaxy NGC 300, using ~66 ksec *XMM-Newton* data obtained during the observations of 2000 December/ 2001 January. A total of 86 sources inside the D_{25} were detected above a maximum likelihood threshold of 10, in the 0.3–6 keV band. I derived for these sources, global properties as X-ray colors and fluxes. Using optical data taken with the 2.2m MPG/ESO telescope, and cross-correlating with the SIMBAD catalogue of known objects, I attempted to classify the sources, mainly from the color-color diagram, and compared with other nearby spiral galaxies. I also performed a deeper analysis of the four brightest sources, for which spectral fitting was possible, and show their light curve.

Deutsche Zusammenfassung

Studien der Röntgenpopulation von Spiralgalaxien außerhalb unserer Milchstraße sind von großer Bedeutung für das Verständnis von Röntgen-Doppelsternen und anderer Röntgenstrahlung emittierender Quellen. Die Röntgenpopulation von Spiralgalaxien setzt sich hauptsächlich zusammen aus Supernova-Überresten, Röntgendoppelsternen mit Begleitern niedriger Masse, Röntgendoppelsternen mit Begleitern hoher Masse und anderen Quellen, deren Natur nicht immer bekannt ist. Zu den letzteren gehören insbesondere die "supersoft sources", die durch ein besonders weiches Spektrum und Röntgenleuchtkräfte im Bereich von 10^{36}–10^{39} erg s^{-1} gekennzeichnet sind, sowie die "ultraluminous X-ray sources", die durch extrem hohe Leuchtkräfte von mehr als 10^{39} erg s^{-1} gekennzeichnet sind.

Die vorliegende Dissertation ist Studien zur Röntgenpopulation der nahen Spiralgalaxie NGC 300 gewidmet. Diese Untersuchungen basieren auf ∼66 ksec langen *XMM-Newton*-Beobachtungen in Dezember 2000 und Januar 2001. In den 0.3–6 keV Daten wurden insgesamt 86 Quellen innerhalb der D_{25}-Scheibe entdeckt mit einem "maximum likelihood" Wert oberhalb von 10. Für diese Quellen werden globale Eigenschaften, wie Röntgenfarben und -flüsse bestimmt. Unter Verwendung optischer Daten des 2.2 m MPG/ESO-Teleskops, unter Zuhilfenahme von Korrelationen mit SIMBAD und unter Benutzung von Röntgen-Farb-Farb-Diagrammen wird versucht, die Quellen zu klassifizieren und die Röntgenpopulation mit der anderer Spiralgalaxien zu vergleichen. Zudem wurde eine tiefere Analyse der vier hellsten Quellen durchgeführt, einschließlich einer Spektralanalyse und einer Untersuchung ihres zeitlichen Verhaltens.

Contents

1 X-ray missions and *XMM-Newton* 10

1.1 History of X-ray astronomy 10
1.2 The *XMM-Newton* mission 13
1.2.1 Main elements of the XMM payload 13
1.2.2 Basic features of *XMM-Newton* 15
1.2.3 EPIC cameras 17
1.2.4 XMM analysis software- the Science Analysis System (SAS) 18
1.2.5 XMM Sciences results 19

2 X-ray sources in normal galaxies 20

2.1 Close binary stars and X-ray binaries 21
2.2 Supernova remnants (SNRs) 23
2.3 Supersoft Sources (SSSs) 27
2.4 Ultraluminous X-ray Sources (ULXs) 27
2.5 X-ray sources in nearby normal galaxies 28
2.5.1 The Milky Way 28
2.5.2 The Local group 28
2.5.3 Other normal galaxies 31

3 Optical and X-ray observations of NGC 300 35

3.1 Introduction to NGC 300 35
3.2 Optical studies of NGC 300 36
3.2.1 Cepheids in NGC 300 and the cosmic distance scale . . . 36
3.2.2 Star formation in NGC 300 36
3.2.3 Wolf-Rayet Stars and Supernova Remnants 38
3.2.4 Optical observations used for this study 39
3.3 X-ray studies of NGC 300 40
3.3.1 X-ray observations used in this study and data reduction . 41

4 X-ray source properties **46**
4.1 Source detection . . . 46
4.2 Color-color diagram and X-ray fluxes . . . 48
4.3 Variability of the sources . . . 52
4.4 Identification of the sources . . . 52
4.4.1 Comparison with other galaxies . . . 57
4.4.2 Conclusions . . . 61
4.5 The luminosity function of NGC 300 . . . 63
4.6 The central diffuse emission region . . . 66

5 Optical counterparts **72**
5.1 Summary tables . . . 76

6 The brightest sources **86**
6.1 Spectral fitting with XSPEC . . . 86
6.1.1 C(I): The Observed Spectrum . . . 87
6.1.2 R(I,E): The Instrumental Response . . . 87
6.1.3 $f(E)$: The Model Spectrum . . . 88
6.2 mechanisms for generating X-rays . . . 88
6.2.1 Thermal bremsstrahlung . . . 88
6.2.2 Synchrotron radiation . . . 89
6.2.3 Blackbody radiation . . . 89
6.2.4 Compton scattering . . . 89
6.3 Spectral fits of the brightest sources . . . 91
6.3.1 XMM J005509.9−374212, source #1 . . . 92
6.3.2 XMM J005510.8−374834, source #3 . . . 93
6.3.3 XMM J005450.2−373849, source #7 . . . 94
6.3.4 XMM J005510.8−373854, source #8 . . . 95
6.4 Light curves of the brightest sources . . . 97

7 Conclusions and future work **107**
7.1 Conclusions . . . 107
7.2 Future work . . . 109

A Optical counterpart images **111**

B Epoch folding and Bayesian methods **118**
B.1 Epoch folding method 118
B.2 Introduction to Bayesian inference 118
B.2.1 Frequentist and Bayesian view 119
B.2.2 Bayes' Theorem 119
B.2.3 Parameter estimation and marginalization 120
B.2.4 Model comparison and Ockham's razor 121
B.2.5 Application 122
B.3 Application on simulated data 123

Introduction

The population of the X-ray sources in NGC 300 using *XMM-Newton* data is studied in this work.

NGC 300 is a normal galaxy belonging to the Sculptor galaxy group. Due to its small distance (~1.88 Mpc; Gieren et al. 2005), this SA(s)d dwarf galaxy is an ideal target for the study of the entire X-ray population of a typical normal quiescent spiral galaxy. These studies are even more simplified by the galaxy's almost face-on orientation and its low Galactic column density ($N_{\rm H} = 3.6\times10^{20}\,{\rm cm}^{-2}$; Dickey & Lockman 1990).

The first X-ray population study of NGC 300 was performed between 1991 and 1997 with a total of five *ROSAT* pointings (Read & Pietsch 2001). In these observations, 29 sources were discovered within the D_{25} disk, the brightest being a black hole candidate with $L_{\rm X} = 2.2 \times 10^{38}\,{\rm erg\,s}^{-1}$ in the 0.1–2.4 keV band. Later, NGC 300 was observed with *XMM-Newton* on 2000 December 26 during *XMM-Newton*'s revolution 192 and 6 days later during revolution 195. Some previous results of these observations were presented by Kendziorra et al. (2001) and Carpano et al. (2004). A deeper analysis of the X-ray population can be found in Carpano et al. (2005). In addition to these X-ray data, observations with the 2.2 m MPG/ESO telescope in La Silla were performed and archival images in the broad band B, V, and R filters are used for this work.

The scope of this study is to characterize, classify and when possible, identify the X-ray population belonging to the galaxy. It is organized as follows. In Chapter 1, I briefly review the history of the several X-ray missions and describe in more details the *XMM-Newton* satellite, its scientific instruments and give some informations about the XMM analysis software. In Chapter 2, I review the classes of objects expected in normal galaxies. These include mainly X-ray binaries (low mass and high mass), supernova remnants, supersoft sources and ultraluminous sources, for which the nature has still not be determined. I also describe the X-ray population of normal galaxies belonging to the Local Group and beyond. Chapter 3 describes in detail the galaxy NGC 300 and summarizes the previous studies that have been performed using optical, radio and X-ray data. I also describe the *XMM-Newton* data of the galaxy and the data reduction using the XMM analysis software.

In Chapter 4, I try to characterize the X-ray population of the galaxy, using the *XMM-Newton* observations. I first describe how the source catalogue is derived and give global X-ray properties. This includes the analysis of the color-color diagram and the source flux calculation. I also attempt to classify and identify the source population. This is done via the color informations, the study of variability, the comparison with other galaxies as well as the $\log N$–$\log S$ diagram. Moreover, I performed the spectral analysis of the galactic central diffuse emission region.

In Chapter 5, I search for optical counterparts of the X-ray sources using the ESO observations, after that I have corrected the X-ray positions for the systematic shift between the X-ray and the optical coordinates. The position and magnitude in the B, V and R band for all optical counterparts are measured. I then cross-correlate the sources with several catalogues, which helps in the identification of the sources.

Chapter 6, is dedicated to the spectral and temporal analysis of the four brightest sources. I first describe how the XSPEC software performed the spectral fitting of the data and enumerate the possible physical processes that can generate X-rays in the kind of sources found. From the spectral fitting I also derive the luminosities of the brightest sources, separately for both revolutions and, analyse their light curves.

Conclusions and future perspectives are described at the end of this work.

Chapter 1

X-ray missions and *XMM-Newton*

1.1 History of X-ray astronomy

X-ray astronomy is the study of celestial highly energetic objects by means of the X-rays they emit. The study of astronomical objects in X-rays really began in 1962 (before then, we only knew that the Sun was a powerful source in this waveband). The reason is that X-ray astronomy can only be carried out at very high altitudes because of the photoelectric absorption of X-rays by the atoms and molecules of the Earth's atmosphere (see Fig. 1.1). Thus rocket flights, balloons or satellites, which could lift scientific instruments above the atmosphere, were necessary for the exploration of the X-ray sky.

The first rocket flight which successfully detected a powerful cosmic source of X-radiation was launched in 1962 by a group at American Science and Engineering (AS&E), led by Riccardo Giacconi. During this 5-min observation, the experiment discovered a very bright source, which was called 'Scorpius X-1' (Sco X-1): the first X-ray source discovered in the constellation Scorpius (Giacconi et al. 1962). This mission also found that the earth is bathed in diffuse X-rays coming from all directions.

Since then, the sensitivity of X-ray observations has increased rapidly, starting with the instrumentation of the X-ray satellites of the 1970's. In 1970, the *Uhuru* satellite was the first one dedicated entirely to celestial X-ray astronomy. It provided the first comprehensive view of the entire X-ray sky. The final *Uhuru* X-ray catalogue contains 339 objects, which are primarily binary stellar systems, supernova remnants, active galaxies and clusters of galaxies (Forman et al. 1978).

From 1977 to 1981, NASA launched a series of larger scientific payloads called 'High Energy Astronomy Observatories (HEAO)'. Two of these missions were dedicated to X-ray astronomy: HEAO-1 a survey mission and HEAO-2, named *Einstein* after launch, an imaging mission. The Large Area Sky Survey (LASS) experiment of HEAO-1 yielded a comprehensive catalogue of 842 X-ray sources (1–20 keV) in a

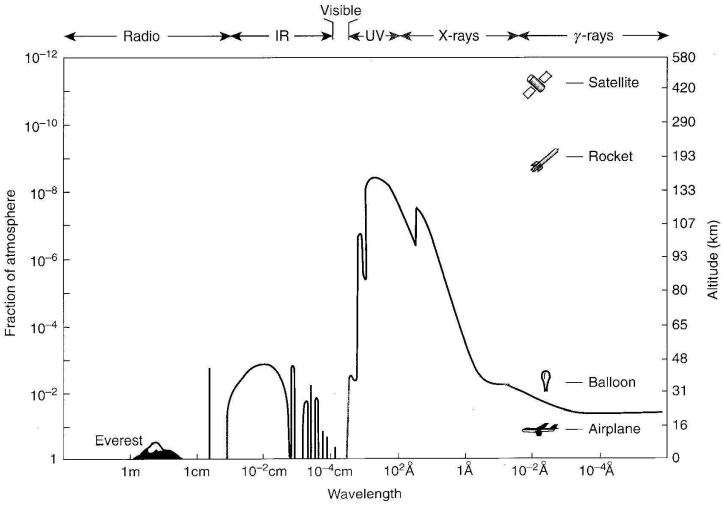

Figure 1.1: Transmission of the electromagnetic radiation by the atmosphere (Charles & Seward 1995).

systematic all-sky survey (Wood et al. 1984).

During the 1980s, the European, Russian and Japanese space agencies continued to launch successful X-ray astronomy missions, such as the X-ray Observatory satellite (*EXOSAT*), *Granat, The Kvant module, Tenma* and *Ginga.* These missions were more modest in scale than the HEAO programs in the 1970s and were directed towards in-depth studies of known phenomena.

In 1990, *ROSAT* (Röntgen Satellite) detected more than 100,000 X-ray objects in its initial survey. It was designed to obtain a deep all-sky survey in soft X-rays during the first six months of the mission and then to continue with two years of pointed observations. It, in fact, had a lifetime of nine years of pointed observations. The principal instrument, an X-ray telescope, was built for high sensitivity below 2.4 keV and the effective area for the X-ray collection was twice that of *Einstein.*

In 1995, NASA launched the *Rossi X-ray Timing Explorer* (RXTE), designed for high resolution X-ray timing, to study variations in emission of such X-ray sources as black hole candidates, active galactic nuclei, X-ray pulsars, neutron stars and other high-energy sources. RXTE played a key role in the discovery in 1996 of a 'bursting pulsar' located near the center of the Milky Way (Finger et al. 1996).

The Italian-Dutch *BeppoSAX* (Satellite per Astronomia X, 'Beppo' in honour of

Giuseppe Occhialini), launched in 1996 (and switched off in 2002), observed the X-ray sky in the 0.1–200 keV energy band. It recorded the first X-ray afterglows for the most energetic bursts of gamma radiation ever detected, providing an identification of the source (Costa et al. 1997).

The *Chandra* X-ray Observatory was launched by the NASA's Space Shuttle Columbia into a high earth orbit on July 23, 1999. It combines an efficient high resolution X-ray telescope with advanced imaging and spectroscopic instruments (see 'The *Chandra* Proposers' Observatory Guide', version 7, `http://cxc.harvard.edu/proposer/POG/html/`). The High Resolution Mirror Assembly consists of a nested set of four paraboloid-hyperboloid (Wolter-1) grazing-incidence X-ray mirror pairs, with a focal length of 10 m. It produces images with a Full Width at Half Maximum of the point spread function (PSF) smaller than 0.5 arcsec, and an effective area at 0.25 keV of 800 cm^2 (400 cm^2 at 5.0 keV). Both grating systems (Low Energy Transmission Grating and High Energy Transmission Grating) have resolving powers ($E/\Delta E$) well in excess of 500 over much of their bandwidth (0.1 to 10 keV). The satellite focusses on such objects as black holes, quasars and high-temperature gases, e.g. in clusters of galaxies.

And finally, also launched in 1999, the X-ray Multi-Mirror Mission (*XMM-Newton*), an ESA satellite, carries three parallel mounted X-ray telescopes, together with an optical/UV telescope, to observe X-ray phenomena. The next section will provide more information about the *XMM-Newton* mission. Further details about X-ray missions can be found in Bradt et al. (1992) and in the book by Charles & Seward (1995). More informations about the *XMM-Newton* satellite are available in the ESA bulletin number 100 (ESA 1999) and in the 2001 Astronomy & Astrophysics special issue (A&A, vol. 365).

1.2 The XMM-Newton mission

The *XMM-Newton* (X-ray Multi-Mirror) satellite honouring Sir Isaac Newton, is a project of the European Space Agency. It has been launched from Kourou, French Guiana, on 10 December 1999, with an Ariane V rocket and is expected to operate for 10 years. The primary scientific objective of XMM is to perform high throughput spectroscopy of cosmic X-ray sources over a broad band of energies ranging from 0.1 to 10 keV.

XMM is designed to investigate in detail the spectra of cosmic sources down to a limiting flux of $10^{-15}\,\mathrm{erg\,cm^{-2}\,s^{-1}}$ and to detect X-ray sources down to a few times $10^{-16}\,\mathrm{erg\,cm^{-2}\,s^{-1}}$ (ESA 1999). With *XMM-Newton*, it is possible to routinely perform such measurements.

1.2.1 Main elements of the XMM payload

XMM-Newton is equipped with 6 scientific instruments (Ehle et al. 2004a):

- The European Photon Imaging Camera (EPIC), produced by a consortium of ten Institutes in four nations: the UK, Italy, France and Germany. These are 3 detectors based on cooled Charge Couple Devices (CCD): 2 MOS (Metal Oxide Semi-conductor) and 1 pn, operating in a photon-counting mode for X-ray imaging, X-ray photometry, and spectroscopy with a moderate spectral resolution, as well as timing studies. See section 1.2.3 for more details.

- The Reflection Grating Spectrometers (RGS) are two essentially identical spectrometers for high resolution X-ray spectroscopy. The reflection grating behind two of the mirrors disperses the various wavelengths at different angles, so that the spectrum can be collected and analysed by a strip of CCD detectors. It has a high spectral resolution, with a resolving power $E/\Delta E \sim 200 - 800$ in the 0.35 – 2.5 keV soft X-ray band.

- The Optical Monitor (OM), co-aligned with the main X-ray telescopes, is a conventional but very sensitive Optical/UV (180 – 600 nm) Monitor which can observe simultaneously the same regions of the sky as the X-ray telescopes. This 30 cm Cassegrain telescope has a field of view of 17 arcmin, with an angular resolution of $\sim$ 1 arcsec through the use of photon-counting detectors. The instrument is well suited for observing faint stars and can detect sources down to a magnitude of 20.7 with a time resolution of 0.5 s.

Fig. 1.2 gives a sketch of the *XMM-Newton* payload. Three Mirror Modules (left), co-aligned with the OM telescope, and equipped with the two RGS grating assemblies, lie at the heart of the XMM telescope. Each Mirror Module, consisting of 58

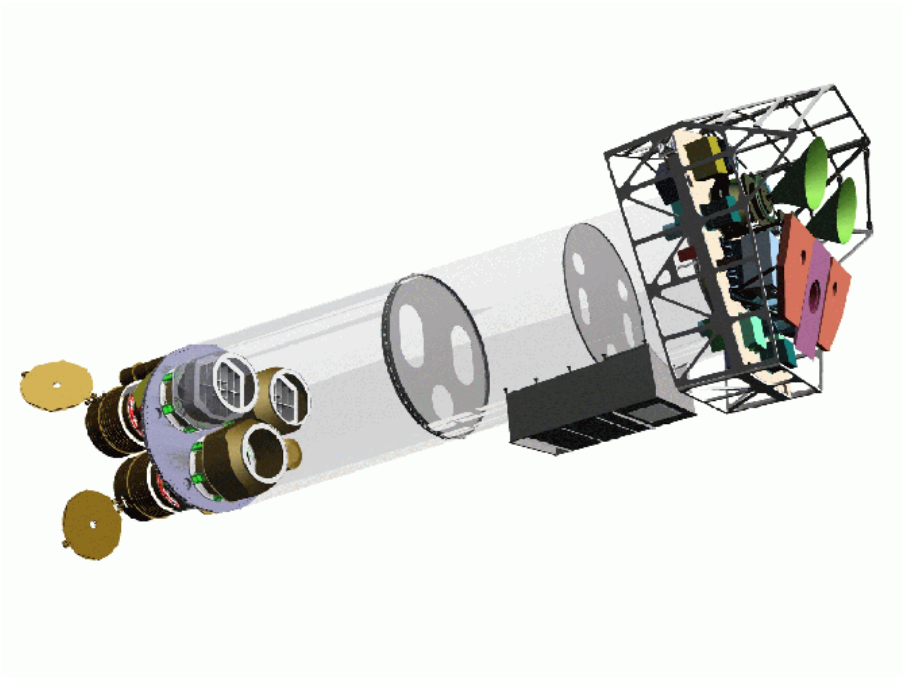

Figure 1.2: Sketch of the XMM payload. The mirror modules, two of which are equipped with gratings, are visible at the lower left. At the right end of the assembly, are shown the focal X-ray instruments and the two RGS detectors (Ehle et al. 2004a).

nested Wolter-I-type grazing incidence mirrors, with a focal length of 7.5 m (ESA 1999), is designed to operate in the X-ray energy band between 0.1 and 10 keV.

The XMM payload is completed by three EPIC cameras, placed in the foci of the three Mirror Modules, and by the two RGS cameras, placed directly behind two of the three Mirror Modules, in front of the two EPIC MOS cameras, and each intercepting about 50% of the converging beams. These instruments are visible at the right part of the Fig 1.2. The pn-CCD detector is located behind the fully open third telescope.

The telescope tube, which is equipped with two aperture stops for stray-light suppression and with an outgassing baffle for cleanliness and decompression purpuses, separates the cameras from the Mirror Modules.

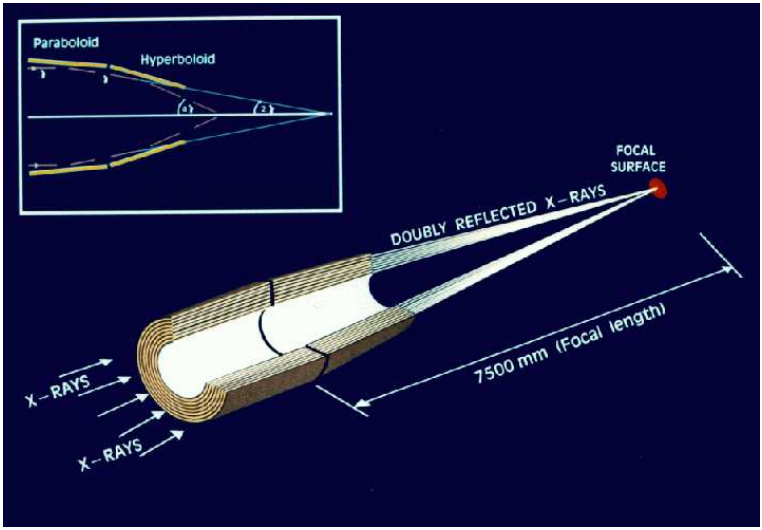

Figure 1.3: The light path of the X-ray telescope having the pn camera in the focus (Ehle et al. 2004a).

1.2.1.1 The X-ray telescopes

As X-rays do not reflect on mirrors at normal incidences, X-ray telescopes are different from optical telescopes. X-rays can be reflected by a mirror only if they have a grazing incidence angle. Wolter telescopes, honoring the German physicist Hans Wolter, use this principle and are composed by several nested mirrors to maximize the effective collecting area. The *XMM-Newton* telescopes are of this type. The combination of the reflection on a first paraboloid surface with a second hyperboloid surface will focus the X-rays on the focal plane. One of the three has a straight light path, as shown in figure 1.3 and two others have grating assemblies in their light paths, diffracting part of the incoming radiation onto their secondary focus (see Fig 1.4).

1.2.2 Basic features of XMM-Newton

The basic features of *XMM-Newton* are (Ehle et al. 2004a):

- Simultaneous operation of all instruments: if not prohibited by target constraints, all six XMM science instruments operate simultaneously. They work independently (i.e., exposures of the individual instruments do not start and end at the same time).
- Good angular resolution. This parameter reflects the ability of the mirror to

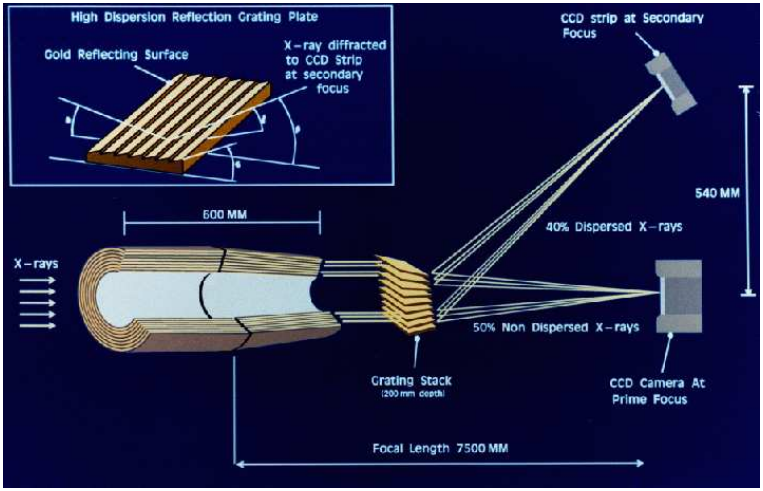

Figure 1.4: The light path of the two X-ray telescope with grating assemblies (Ehle et al. 2004a).

focus photons. This high sensitivity is achieved by the use of 58 thin nested mirror shells in each X-ray telescope. The resulting point spread function (PSF) has a full width at half maximum (FWHM) on axis of the order of 6″. The PSF of the X-ray telescope depends on the source off-axis angle, i.e., its distance from the center of the field of view (FOV). The PSF at large off-axis angles is asymmetric, having a kind of 'bean' shape.

- High sensitivity: *XMM-Newton* carries the telescopes with the largest effective area of a focussing X-ray telescope ever. The total mirror geometric effective area (which reflects the ability of the mirrors to collect radiation at different photon energies) at 1.5 keV is about 1550 cm^2 for each telescope and 4650 cm^2 in total. The effective area of the mirror does not only depend on the energy but is also function of the off-axis angle within the mirror 30′ field of view (FOV). With increasing off-axis angle, fewer of the photons entering the telescopes reach the focal plane. This effect is called 'vignetting'.

- Moderate to high spectral resolution: the EPIC CCD cameras have moderate spectral resolution (with a resolving power, $E/\Delta E \sim 20 - 50$). The RGS spectrometers offer much higher spectral resolution (see section 1.2.1).

- Simultaneous optical/UV with X-ray observations. This allows the monitoring and identification of X-ray sources by the X-ray telescope as well as an optical

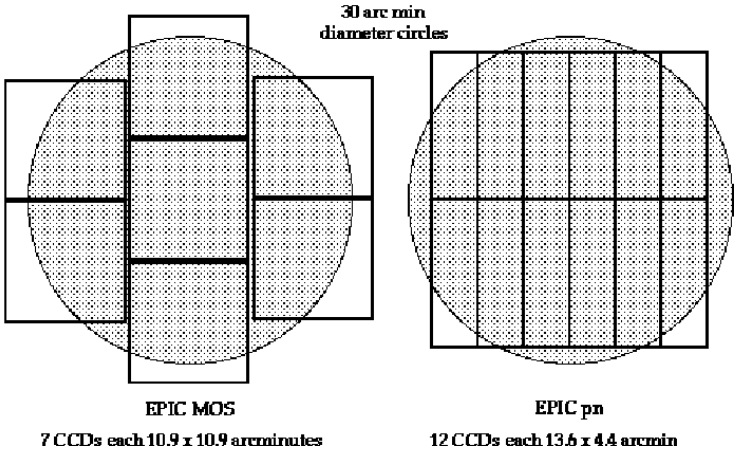

Figure 1.5: Comparison of focal plane organisation of EPIC MOS and pn cameras (Ehle et al. 2004a). Note that the two EPIC MOS cameras are rotated by 90° with respect to each other.

imaging of the surrounding field.

1.2.3 EPIC cameras

Two of the three EPIC cameras consist of an array of seven metal-oxide (MOS) CCDs covering the 30 arcmin field of view. Each MOS CCD features an imaging area of 600×600 pixels, 40×40 μm^2 in size, capable of detecting X-rays in an energy band ranging from 0.1 to 12 keV, with a maximum timing resolution of 1.5 ms. In the standard observation mode, the full focal plane, consisting of the seven CCDs, is read out in 2.6 s. More informations on EPIC MOS cameras can be found in Turner et al. (2001).

The third camera is a set of twelve back-illuminated CCDs, generated on a single 10 cm-diameter Si wafer. Each of them is organised as a 64×200 matrix of 150 micron-sized ($4\farcs1$) pixels. The use of p-n technology has resulted in high quantum efficiency and full-frame readout times of 73.4 ms can be achieved (200 ms in extended full frame mode), with a maximum time resolution of 30 μs (7 μs in burst mode). More informations on EPIC pn camera can be found in Strüder et al. (2001).

Fig. 1.5 shows the focal plane of the two types of EPIC cameras: MOS and pn. The shaded circle depicts the $30'$ diameter field of view. The most important characteristic of the EPIC cameras are given in Table 1.1 (Ehle et al. 2004a).

All EPIC CCDs operate in photon counting mode with a fixed read-out frequency, producing event lists, that are tables with one entry line per received event, listing

Table 1.1: Basic characteristics of the EPIC cameras (Ehle et al. 2004a).

Instruments	EPIC MOS	EPIC PN
Bandpass	0.15–12 keV	0.15–15 keV
Field of view (FOV)	30′	30′
PSF (FWHM)	5″	6″
Pixel size	40 μm (1.″1)	150 μm (4.″1)
Time resolution	1.5 ms	0.03 ms
(fast data acquisition mode)		
Spectral resolution at 1 keV	~ 70 eV	~ 80 eV
Spectral resolution at 6.4 keV	~ 150 eV	~ 150 eV

(among others) attributes of events such as the position at which they were registered, their arrival time and their energies.

The EPIC cameras allow several modes of data acquisition. The data-handling units select and control the various operating modes of the cameras (Ehle et al. 2004a):

- Full-Frame mode (and 'extended full frame mode' for pn camera only) allows the readout of all CCDs and thus the full FOV is covered.
- In the Partial-Window mode, the central CCD of MOS cameras is read out only partially, while for the pn camera, only half of the area in all 12 CCDs is read out.
- In the Fast/Timing mode no two-dimensional imaging is performed, but data from a predefined area on the pn CCD1 chip are collapsed into a one-dimensional row to be read out at high speed (see Table 1.1).
- And finally there is the Burst mode, which is a special flavour of the timing mode of the EPIC pn camera, with very high time resolution, but very low duty cycle (~3%).

1.2.4 XMM analysis software- the Science Analysis System (SAS)

The analysis of *XMM-Newton* data is supported by the Science Analysis System (SAS) software package, which at the time of writing was available in version 6. It allows the reduction and the analysis of the XMM science data from all science instruments, EPIC MOS & pn, RGS and OM, and the extraction of standard data products such as event files, images, spectra, light curves, and source lists from the X-ray event lists, as well as the generation of the appropriate response matrices (Ehle et al. 2004a).

XMM SAS has been developed by a team of scientists located at the ESA XMM SOC and the XMM Survey Science Center (SSC).

The derivation of accurate calibration data, and the proper incorporation of this knowledge into the SAS software is a continuing process. The produced spectra can then further be analysed by standard X-ray astronomy spectral analysis packages. The status of the EPIC calibration can be found at `http://xmm.vilspa.esa.es/docs/documents/CAL-TN-0018-2-4.pdf`.

1.2.5 XMM Sciences results

In April 2003, the first version of the *XMM-Newton* source catalogue has been released (http://xmmssc-www.star.le.ac.uk/newpages/xcat_public.html). This was generated by the Survey Science Center (SSC; PI: M. Watson, Leicester, UK). More than 80 % of the entries have never been reported previously as X-ray sources, and the catalogue is expected to become a significant astronomical resource. The catalogue contains 33026 X-ray sources detected with a maximum likelihood threshold of 8. Their positional accuracy is generally $\sim 0\farcs5 - 2''$ (68 % confidence radius).

Thanks to these observations, real improvements have been made in the comprehension of X-ray objects like stars, SNRs, neutrons stars, gamma-ray bursts, AGNs, cluster of galaxies, X-ray background, etc. More details about these results can be found in the ESA's report to the 35th COSPAR meeting (ESA 2004).

Chapter 2

X-ray sources in normal galaxies

A normal galaxy is a galaxy which does not have an active nucleus nor it is unusually luminous at any wavelength. Our galaxy, the Milky Way, is a good example of a normal spiral galaxy.

X-ray emission from normal galaxies comes from discrete objects and a faint central diffuse emission region which can be truly diffuse or due to faint unresolved sources.

Because normal stars are very inefficient X-ray emitters (their coronal X-ray luminosities range from 10^{26} and $10^{33}\,\mathrm{erg\,s^{-1}}$), the brightest X-ray sources in normal galaxies can be split into 2 groups: supernova remnants (SNRs) and compact X-ray sources. A large fraction of compact X-ray sources are members of close binary systems, for which gravitational potential energy is efficiently converted into radiation. They have luminosities between 10^{37} and $10^{38}\,\mathrm{erg\,s^{-1}}$. They often operate close to the Eddington limit where the pressure of the infalling material is balanced by the pressure of outflowing radiation. Supernova remnants are also strong X-ray sources with X-ray luminosities in the range 10^{35} to $10^{37}\,\mathrm{erg\,s^{-1}}$.

By studing the X-ray population of normal galaxies from X-ray images, one has also to take into account another kind of object seen in a galaxy field: the "interlopers". These are sources in the field, which are not members of the galaxy being observed. These are usually much closer than or much more distant than the galaxy. These can be foreground galactic stars or background nuclei of active galaxies or quasars. Active Galactic Nuclei (AGN) and Quasi-stellar Objects (QSOs) together form the large population of objects known as active galaxies. It is generally accepted that active galaxies are primarily powered by the accretion of matter onto a central supermassive black hole.

External galaxies, and in particular galaxies in the Local Group, are better laboratories to study global properties of X-ray binaries, SNRs, pulsars and stellar associations than our own galaxy. They present some advantages (Lewin et al. 1995):

- The sources within a galaxy do not suffer from the distance uncertainty that affects galactic X-ray sources.

- Except for very edge-on galaxies, these sources are not affected by large line-of-sight absorption, as are, for example, galactic bulge sources.
- In external galaxies it is easy to associate sources with different galactic components (e.g. bulge, disk, spiral arms).
- Finally, different galaxies provide different sites in which to test theories of Galactic source formation and evolution for different metallicity/stellar population, star formation activity, galaxy structure.

2.1 Close binary stars and X-ray binaries

A binary star is a system composed of two stars which orbit around their common center of mass. A binary system composed of a compact object (white dwarf, neutron star or black hole) and a normal star can produce X-ray (and other) emissions if the stars are close enough together that material is transferred from the normal star onto the dense, collapsed star, thereby releasing a large amount of gravitational energy in the form of radiation.

A special class of close binary stars are the 'X-ray binaries', so-called because they emit strong X-ray radiation. They contain either a white dwarf, a neutron star or a black hole accreting material from a companion star. The X-rays come from the area around the collapsed star where the material that is falling toward it is heated to very high temperatures. The gravitational potential of a neutron star or a black hole can yield very high luminosities from a relatively small amount of infalling material. If dM/dt is the rate of accreted material of a compact object of mass M and radius R, then the luminosity is (Charles & Seward 1995):

$$L = \eta \frac{dM}{dt} c^2. \tag{2.1}$$

Typical values of η are 0.1 for neutron stars, 0.06–0.42 for black holes and 0.001 for white dwarfs.

If the compact object is a neutron star, it is important to derive the strength of its magnetic field. When the magnetic field is very strong ($\sim 10^{12}$ G), this will disrupt the accretion flow from the companion object, which will then funnel onto the magnetic pole (Pringle & Rees 1972; Davidson & Ostriker 1973; Lamb et al. 1973). If the magnetic axis is misaligned with respect to the rotation axis, then one will observe X-ray pulsations when the beamed emission from the magnetic poles rotates through the line of sight (Mészáros et al. 1980; Nagel 1981a,b; Wang & Welter 1981). If the magnetic field of a neutron star is weak ($< 10^6$ G), the accretion disk can come close to the neutron star surface. Then the emission will primarly come from the inner

accretion disk and the boundary layer between the disk and the neutron star (Mitsuda et al. 1984). If, on the other hand, the compact object is a black hole, the X-rays are emitted from the inner disk, resulting from viscous heating (Shakura & Sunyaev 1973).

Instabilities in the emission or the accretion flow in X-binaries, can be responsible for rapid fluctuations or quasi-periodic flucuations. These can also give rise to X-ray bursts or flares.

One of the most reliable characteristics that distinguish a neutron star from a black hole candidate is the mass of the compact object. No stable neutron stars are believed to exist with masses greater than $\sim 3\ M_\odot$. So any compact object with mass greater then $\sim 3\ M_\odot$ is usually assumed to be a black hole (Rhoades & Ruffini 1974; Kalogera & Baym 1996). Another difference is the presence or absence of a solid surface. For example, a black hole will never produce X-ray bursts.

Binaries which have a white dwarf and a normal companion star are called 'cataclysmic variables' (CVs). The companion star loses material onto the compact object. Since this object is small, the gravitational potential energy is high (but still low compared to neutron stars and black holes) and is converted into X-rays during the accretion process. These are fairly faint in X-rays: X-ray luminosities of CVs have been measured e.g. by *ROSAT* during the All Sky survey and they are not higher than $10^{32}\,\mathrm{erg\,s^{-1}}$ (Verbunt et al. 1997). For that reason they cannot be visible in external galaxies.

Many X-ray binaries are transient sources. They appear suddenly at locations where no source had be seen before and become extremely bright. They have fairly rapid rise in intensity followed by a gradual decline. Typically transients reach their maximum intensity within few days and decline back to undetectability many tens or hundreds of days (White et al. 1984; van Paradijs & Verbunt 1984) and the change in intensity is typically a factor of 10^4–10^5. Many transients are seen to recur on timescales from days to tens of years; some recur periodically, others randomly. These transient episodes may result from an instability in the accretion disk, or a mass ejection episode from the companion. A large fraction of black hole candidates are X-ray transients (Lewin et al. 1995).

X-rays binaries constitute the brightest class of X-ray sources in the sky. An optical identification is crucial to establish the nature of the mass-donating companion star. The mass of the companion object determines the mode of mass transfer to the compact object. There are two basic classes of X-ray binaries (here white dwarfs are not included): High-Mass X-ray Binaries (HMXB) and Low-Mass X-ray Binaries (LMXB). Catalogues containing 130 known HMXBs and 150 LMXBs can be found in Liu et al. (2000) and Liu et al. (2001), respectively.

2.1.0.1 High-Mass X-ray Binaries (HMXB)

In High-Mass X-ray Binaries (HMXBs), the companion star is a giant or supergiant O or B star (mass above $\sim 10\ M_\odot$). It has a substantial stellar wind, with a mass loss rate between 10^{-6} and $10^{-10}\ M_\odot\ yr^{-1}$. If a neutron or black hole has a relatively close orbit, it will capture a significant fraction of the wind, sufficient to power the X-ray source. The X-ray luminosity is either powered by pure stellar wind accretion or, in the case of the brighter systems, by Roche-lobe overflow via accretion disk (Liu et al. 2000). Optically we see only the early-type star because it is luminous: the optical luminosity is often higher than the X-ray one (which comes from the compact object). The ratio of their X-ray to optical luminosities ranges from 10^{-3} to 10^{1}. Typical orbital periods are in the range of 5h to 200 days and luminosities are in the range of 10^{31}–10^{39} erg s^{-1} (Lewin et al. 1995).

2.1.0.2 Low-Mass X-ray Binaries (LMXB)

They have many properties in common with cataclysmic variables. The primary star is a main sequence star (type A or later) with mass $\lesssim 1\ M_\odot$. A late type star does not have a natural wind strong enough to power the observed X-ray source. In this case the companion star has evolved to fill its Roche lobe (surface of equal gravity) and is transferring material through a funnel point, the inner Lagrangian point L_1, onto the compact object (see Fig. 2.1). Because of the angular momentum of the material as it leaves the star, it cannot fall directly onto the compact object, but must instead go into the orbit around it, thereby forming an accretion disk due to its viscosity. The material in this accretion disk does then slowly spiral inwards toward the compact object (Shakura & Sunyaev 1973).

LMXBs are luminous X-ray sources ($> 10^{34}$ erg s^{-1}). The X-ray heating of the accretion disk and the companion star dominates the optical light where LMXBs appear as faint blue stars. Except for transient sources, their X-ray to optical luminosities ranges from 10^{2}–10^{4} (Lewin et al. 1995) and their orbital light curves can exhibit X-ray eclipses. Members of this class are often refered to as 'Galactic-bulge sources' because they have the same distribution as the galactic bulge and are associated with the old stellar population.

2.2 Supernova remnants (SNRs)

A supernova remnant (SNR) is what remains after a supernova explosion. Most of the energy of the supernova explosion is carried away as kinetic energy, the shell of the ejected material expands rapidly. The outer parts of the star are expelled at velocities of 5000–10000 km s^{-1} (Fabian et al. 2004). The supersonic outflow of the stellar ejecta cools quickly after the explosion and a low density region is left in the

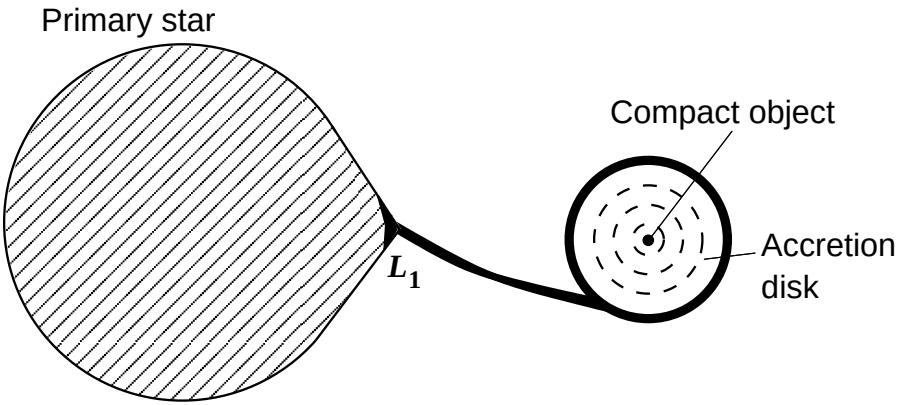

Figure 2.1: Mass transfer from the primary star onto the compact object via the inner Lagrangian point L_1 (Warner 1995).

interior. Over time-scales of years, this outflow sweeps up the surrounding interstellar medium and heats it to X-ray temperatures. The swept-up material progressively retards the motion of the expelled mater which causes another shock, moving this time in a backward direction. This shock will also produce X-rays. After the expansion phase, the remnant looks like an extended diffuse region of X-ray emitting plasma where temperatures are up to several millions Kelvin (Fabian et al. 2004). The X-rays are thermal, they are generated by bremstrahlung, i.e., fast electrons colliding with positive ions, or by electron-ion recombinations. The SNR stays in a 'radiative' phase, for about 10^5 years, where most of the internal energy is radiated away (Charles & Seward 1995). The shell then coasts through interstellar space, it becomes fainter and fainter until it is undistinguishable from the surrounding medium.

Some SNRs contain a rapidly rotating neutron star with a strong magnetic field, which is observable as X-ray pulsar if its emission is beamed in our direction. The radiation is produced by synchrotron process and extends throughtout the electromagnetic spectrum, from radio waves to gamma rays. Because the injected energy comes from the pulsar, the surrounding SNR is not 'shell-like' but 'plerion-like' ('filled-in'). In the X-ray wavelengths, this synchrotron radiation dominates over thermal radiation.

Most remants have been discovered as spatially extended sources in radio surveys. Old SNRs ($> 10^4$ yr) are several times larger in size than the young remnants ($< 10^3$ yr) and can have intrinsic diameters exceeding 20 pc. X-ray emission of the older SNRs occurs at lower energies (below 2 keV) than the younger ones (Giacconi & Gursky 1974). The temperature of this plasma is of $\sim 10^6$ K or higher.

SNRs are important to study for several points: they are powerful mechanisms for energizing and chemically enriching the interstellar medium of a galaxy; by analyzing this debris we can learn a lot about the progenitor star, the explosion and so about supernovae; they also have an important role in star formation, as the remnant shocks can trigger the collapse of dense molecular clouds.

SNRs show a variety of sizes, structures and types, depending on what caused them, their age and their distance with respect to the Earth. High resolution images of SNRs show a rich structure of X-ray emitting filaments, and their X-ray spectra are generally dominated by bright emission lines of highly ionized elements from C through to Fe or Ni (Fabian et al. 2004). A catalogue of 231 known Galactic SNRs can be found in Stephenson & Green (2002). They range in angular size from few arcmin to several degrees, with most being between 10 arcmin and 1 degree. Their physical sizes are ranged from a few to $\sim$ 100 parsecs in diameter. Because of the Galactic absorption of optical and X-ray radiation, most Galactic SNRs have been discovered at radio wavelengths (only 30% of these have also been detected in X-ray and 20% in the optical).

Nearby galaxies, which are nearly face-on oriented and located at high Galactic latitude are better choices for SNR searches because they have low Galactic and intrinsic absorption. It is necessary to perform multi wavelength searches of SNRs since observation through a single spectral window cannot identify all types of SNRs (Pannuti et al. 2000a). The three most common wavelength domains that have been used for SNR survey are the radio, X-ray and optical energy band:

- Electrons gyrating in the SNR's magnetic field produce synchrotron radiation at radio frequencies (Duric et al. 1995),
- The expanding SNR shock heats the surrounding interstellar medium to temperatures of 10^6–10^7 K producing X-ray emission (Itoh & Masai 1989). The low absorption in external galaxies makes it possible to detect emission lines from highly ionised ions from O, Ne, Mg, Si, S and Fe, which are visible in the 0.5–3 keV band (van der Heyden et al. 2004),
- A SNR can also be detected optically by emission from collisionally ionized elements as well as Hα recombination emission (Pannuti et al. 2000a).

The degree to which a SNR becomes a radio, X-ray, or optical emission line source depends on the environment and evolutionary stage of the SNR. Figure 2.2 shows a color composite image of the SNR Cassiopeia A (Cas A), taken in infrared, optical and X-ray band.

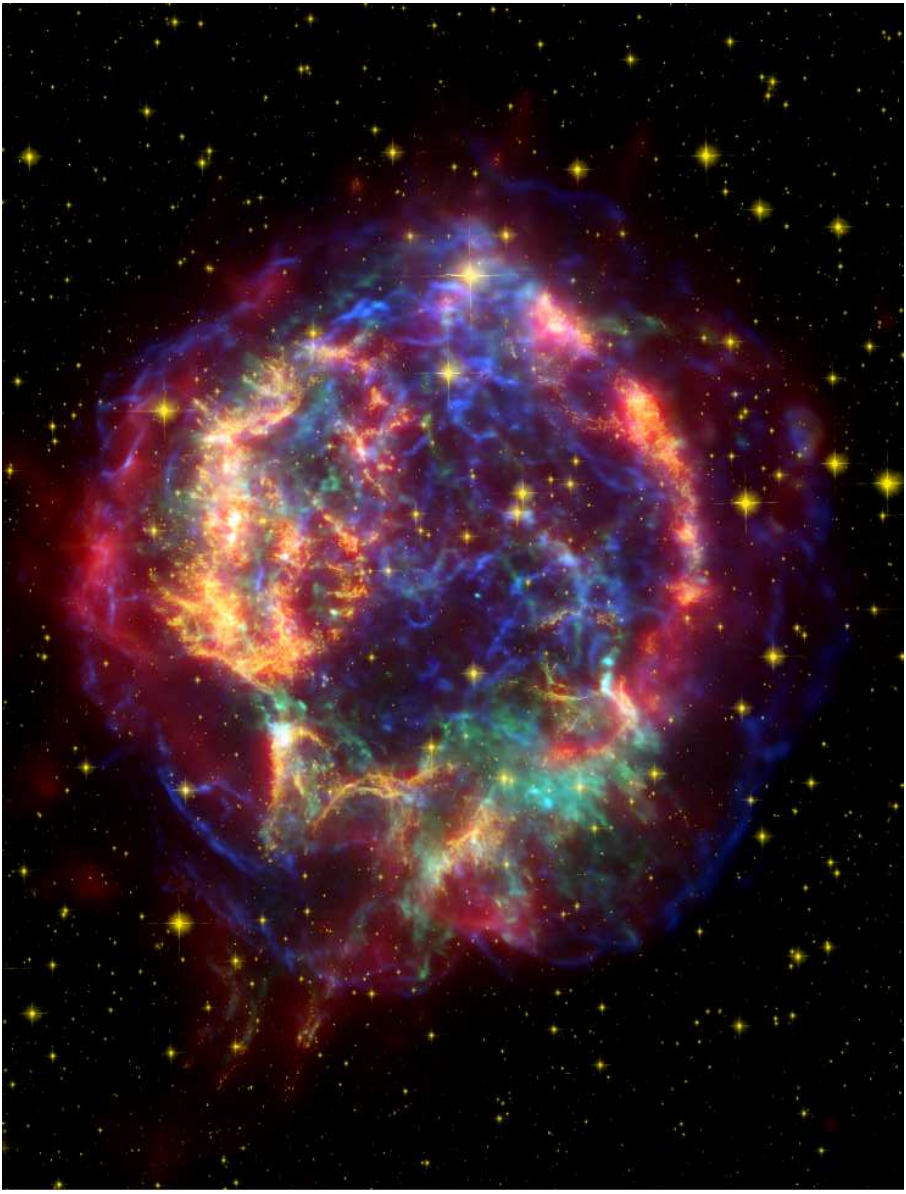

Figure 2.2: Color composite image of the SNR Cas A. Infrared data from the Spitzer Space Telescope are colored red; optical data from the Hubble Space Telescope are yellow; and X-ray data from the *Chandra* X-ray Observatory are green and blue (http://chandra.harvard.edu/photo/2005/casa/index.html).

2.3 Supersoft Sources (SSSs)

Supersoft sources were first discovered in the Large Magellanic Cloud (amongst others the two prototypes CAL83 and CAL87) with the *Einstein* Observatory (Long et al. 1981). SSSs are hard to be detected in the Galactic plane due to high interstellar absorption. Later, *ROSAT* discovered many other supersoft sources in the Galaxy, the Magellanic Clouds (Trümper et al. 1991; Kahabka et al. 1994) and in M31, and astronomers thus established, in the early 1990s, luminous SSSs as a new class of objects. They are characterised by a very soft spectra (typically $kT < 100$ eV) and they have luminosities in the range of 10^{36} –10^{39} erg s^{-1}.

According to van den Heuvel (1999), some 37 SSSs have been discovered with *ROSAT*: 16 in the Andromeda Galaxy (M31), 11 in the Magellanic Clouds, 9 in our galaxy and 1 in NGC55. Since 1997, some of the brightest SSSs have been observed by *BeppoSAX* satellite (Parmar et al. 1997, 1998).

Several of these objects have been optically identified with close binary systems. The most promising model to explain the flux emitted from the brightest SSSs has been proposed by van den Heuvel et al. (1992). They suggest that these ultrasoft X-ray emission can be explained by steady nuclear burning of hydrogen accreted onto white dwarfs with masses in the range of 0.7–1.2 $M_\odot$. The required mass transfer rates, between $\sim 10^{-7}$ and 4×10^{-7} $M_\odot yr^{-1}$, can be obtained in short period binaries ($P < 1$–2^d) by Roche-Lobe overflow from a companion that is more massive (1.4–2.2 $M_\odot$) than the white dwarf. However, some of the SSS are transient sources, or associated with hot nuclei of young planetary nebula, symbiotic systems, or recent novae. This suggests that the SSS class is likely including objects of several different types.

Recently, *Chandra* and XMM reobserved external galaxies with high resolution. Greiner et al. (2004) pointed out that a large fraction (30%) of SSSs found in M31 are transient sources, with turnoff and turnon times on the order of a few months. Swartz et al. (2002) observed M81 and detected nine luminous supersoft X-ray sources, gave their spectral properties and light curves. Numerous deep observations of the nearby galaxies have been performed by *Chandra* and XMM, but the discovery of supersoft sources has been reported for only few galaxies (see section 2.5 for more details concerning the number of SSSs found in nearby galaxies).

2.4 Ultraluminous X-ray Sources (ULXs)

Ultraluminous X-ray sources are defined by an intrinsic luminosity $> 10^{39}$ erg s^{-1}, which exceeds the Eddington luminosity of a 1.4 $M_\odot$ neutron star by a factor of $\gtrsim 5$. The nature of these sources is still unclear. A first model is an accreting binary with an intermediate mass black-hole (M>10–1000 $M_\odot$). A second model is that of a

binary system with beamed emission, which involve normal mass accretors (neutron star or stellar-mass black hole, see Zezas & Fabbiano (2002) for a review). ULXs are variable and tend to have spectra that can be well modeled with a multitemperature of $\sim$ 1–2 keV, although some of them experience hard/low-soft/high transitions typical of black hole candidate binaries (Makishima et al. 2000).

A survey of ULXs in 313 nearby galaxies within 40 Mpc has been performed by Liu & Bregman (2005), using 467 *ROSAT* HRI observations. 562 extragalactic X-ray point sources have been found in 173 nearby galaxies, with $L_X = 10^{38}$–10^{43} ergs s^{-1} and 216 of which with $L_X > 10^{39}$ ergs s^{-1}. Some of them are associated with supernovae (remnants), H II regions/nebulae, or young massive stars in star-forming regions, and a few ULXs have been identified as old globular clusters. Some ULXs show great variability on timescales from days to up to 10 years.

2.5 X-ray sources in nearby normal galaxies

2.5.1 The Milky Way

X-ray sources from the Milky Way have been observed by the All-Sky Monitor (ASM) aboard the Rossi X-ray Timing Explorer (RXTE) for $\sim$ 5 years, in the 2–10 keV band. The catalogue consists of 340 sources of which 217 galactic, 112 extra galactic and 10 unidentified sources. Grimm et al. (2002) identified 105 LMXBs, 51 HMXBs, 7 SNRs and 10 CVs. The $\log N$–$\log S$ diagram for these sources are shown in Figure 2.3. We see that SNRs and HMXBs can be described, above the completeness limit, with a power law function (the SNR slope being flatter than the HMXB one), while LMXBs are described by a modified power law which takes into account the gradual steepening of the $\log N$–$\log S$ relation towards higher fluxes. In the same paper, these authors show that HMXBs are often associated with the spiral arms of the galaxy, while LMXBs are more concentrated in the galactic center.

2.5.2 The Local group

Our Milky Way and the Andromeda galaxy (M31) dominate the 'Local group' of galaxies. This contains at least 20 members, which are fainter and less massive. The nearest one is the Large Magellanic Cloud (LMC), at a distance of 55 kpc, which contains about one tenth the number of stars in the Milky Way (Charles & Seward 1995). Not far away from it, is the Small Magellanic Cloud (SMC), 63 kpc away, which is about half the size of the LMC. Then comes the Andromeda Galaxy, M31, located at 670 kpc, it has the same size as the Milky Way, containing 1.5 times as many stars. M33, at a distance of 720 kpc; it is a face-on spiral galaxy. These nearby galaxies are close enough that one can identify supernova remnants by their spatial extent. A review of their X-ray population is given below.

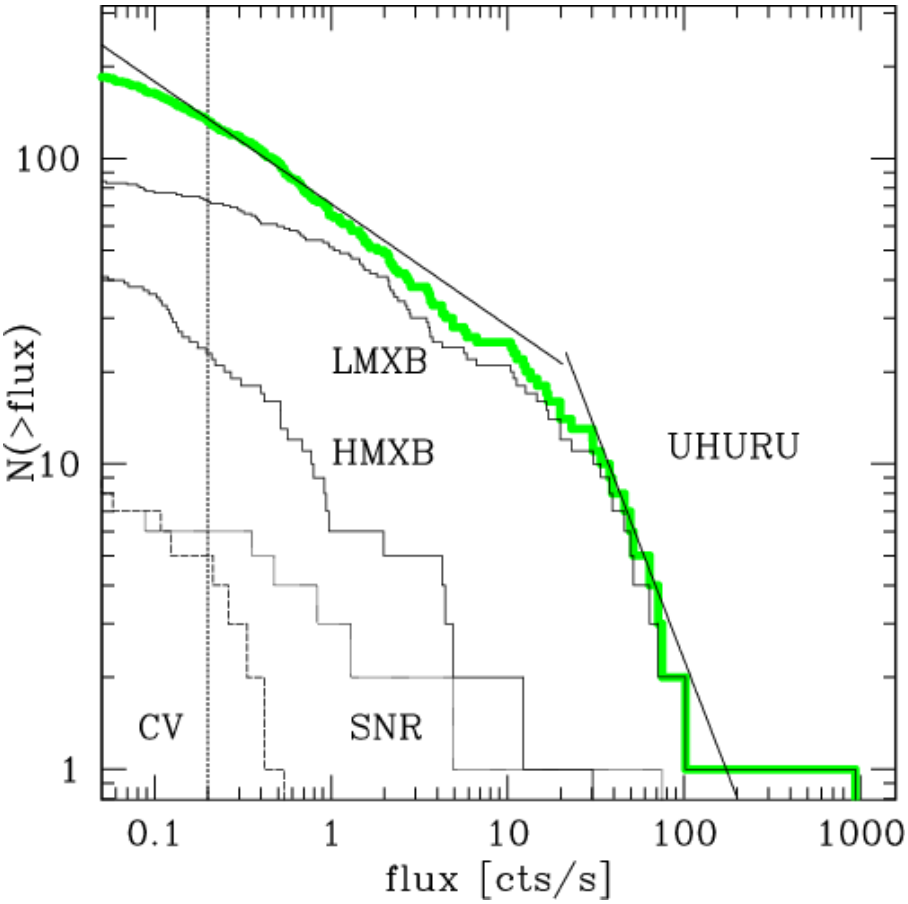

Figure 2.3: log N–log S diagram for all galactic sources derived from the RXTE satellite (thick line), as well as the subsamples: LMXBs, HMXBs, SNRs and CVs. The broken line show the relation obtained by *Uhuru* and the vertical line shows the completeness limit (Grimm et al. 2002).

2.5.2.1 *The Magellanic Clouds*

In the *Einstein* X-ray observations made in the early 1980s, over 120 sources were detected in the LMC and 40 within the SMC. A large number of supernova remnants were identified by their spatial extent as well as a number of fainter (10^{34}–10^{36} erg s^{-1}) unidentified X-ray sources. Wang et al. (1991) reanalysed the *Einstein* database

of the LMC and listed 105 sources, from which 33 were new, and eliminated a number of spurious and/or marginal detections from the previous list. Fifty of these sources were identified optically: 28 of them were SNRs, 13 foreground stars, 3 were background AGNs, and there were 9 X-ray binaries. Based on fluxes, X-ray spectra and deep survey results, Hutchings & Cowley (1991) estimate the remaining 55 unidentified sources to be ∼20 SNRs, 25 background faint AGNs, ∼7 foreground stars and perhaps up to three X-ray binaries. The luminosity limit for the *Einstein* observatory at a distance of the LMC was $\sim 10^{35}$ erg s^{-1}.

According to Lewin et al. (1995), nine X-ray binaries are known in the LMC. This is about what we expect if we scale down the number of galactic X-ray binaries (∼180) by the ratio of the masses: $M_{\rm G}/M_{\rm LMC} \sim 23$ (Binney & Tremaine 1987). Such a kind of scaling is however, not appropriate for the SMC, whose mass is one-tenth of the LMC. This predicts about one X-ray source whereas four are known. Three of the seven HMXBs in the Magellanic Clouds contain X-ray pulsars, which is the same as the galactic fraction (∼45%), and 2 of the seven ones (LMC X-1 and LMC X-3), contain black hole candidates, which is higher than the galactic fraction (∼2%). Four LMXBs are catalogued in the LMC, while none are seen in the SMC.

More recently, a deep analysis of the X-ray population of the Magellanic Clouds, observed by *ROSAT* between 1990 and 1998, has been made by Haberl & Pietsch (1999), Haberl et al. (2000), Sasaki et al. (2000a) and Sasaki et al. (2000b). Here is a summary of their results:

- 758 sources were detected in the LMC by the *ROSAT* PSPC instrument and 397 by the *ROSAT* HRI. 138 of the HRI sources are contained in the PSPC catalogue, while 259 sources are new. Based on positional coincidences with catalogues and on X-ray properties, 114 PSPC (94 HRI) sources were identified with known objects. The PSPC (HRI) catalogue contains: 17 (9) X-ray binaries, 9 (5) SSSs, 46 (24) SNRs or SNR candidates, 57 (39) foreground stars and 15 (9) background extragalactic objects.

- 517 PSPC (121 HRI) X-ray sources were detected in the SMC. 75 of the 121 HRI sources had PSPC counterparts. 158 PSPC (56 HRI) sources were identified, from which: 17 (6) SNRs + 2 candidates, 9 (4) SSSs or suspected ones, 6 (12) X-ray binaries or suspected ones, 46 (1) background AGN, 12 (4) foreground stars + 12 candidates.

2.5.2.2 M31

The Andromeda galaxy, M31, is a spiral galaxy of type Sb. An analysis of the entire set of the *Einstein* observations made by Trinchieri & Fabbiano (1991) has led to

the detection of 108 X-ray sources, with 0.2–4 keV luminosities between 10^{37} and 10^{38} erg s^{-1}. *ROSAT* observations (Supper et al. 1997) in the 0.1–2.4 keV band have more than tripled this number (396 sources), with luminosities in the range of 3×10^{35}–2×10^{38} erg s^{-1}. 43 of these have been identified with foreground stars, 29 with globular clusters, 17 with SNRs, 3 with other galaxies, and 3 with radio sources. With respect to the *Einstein* Survey, 327 sources were newly detected. They also classified 15 objects as SSSs according to their spectral characteristics.

With the *Chandra* satellite, Kaaret (2002) detected 142 point sources with luminosities between 2×10^{35}–2×10^{38} erg s^{-1} in the 0.1–10 keV band. They suggest that the population is likely dominated by LMXBs. Finally, from the *XMM-Newton* observations, Trudolyubov & Priedhorsky (2005) detected 17 X-ray sources having bright radio counterparts and 15 X-ray sources coincident with SNR candidates from optical to radio surveys.

2.5.2.3 M33

M33 is a face-on spiral galaxy of type Sc. This presents an advantage to see where the X-ray sources are located within the spiral structure. The galaxy has been extensively observed with *Einstein*, first by Long et al. (1981) and later by Trinchieri et al. (1988), who detected 13 point sources within the disk and the spiral arms with luminosities between 10^{35}–10^{38} erg s^{-1}. M33 is unique amongst the Local Group, having a very bright ($\sim 10^{39}$ erg s^{-1}) X-ray source (M33 X-8) located at a position consistent with the optical nucleus of the Galaxy. This source dominates the X-ray flux ($\sim$70%) from the galaxy. Another X-ray source (M33 X-7) is an eclipsing X-ray binary pulsar with an orbital period of 3.45 day and pulse period of 0.31 s (Dubus et al. 1999).

Deeper analysis of the brightest X-ray sources has been made more recently by Parmar et al. (2001), using *BeppoSAX* data. The nature of M33 X-8, which shows a transitory intensity modulation of 105.9 days, is still unclear. Many models have been proposed (see Parmar et al. 2001), the authors suggest that the source can be a $\sim$10 $M_\odot$ black hole, accreting from a binary companion. Finally, Pietsch et al. (2004) detected 408 sources down to a 0.2–4.5keV luminosity of 10^{35} erg s^{-1}, using *XMM-Newton* data. 21 of these were SNRs, 23 SNR candidates, 5 were SSSs and 2 X-ray binaries. They also identified 5 foreground stars, 30 foreground star candidates, 12 AGN candidates, one background galaxy and one background galaxy candidate.

2.5.3 Other normal galaxies

Other galaxies, outside the Local group, which are much far away, were also observed in X-rays. Of course, the more distant the galaxy is, the greater is the threshold for X-ray source detection and/or the greater is the observing time. With *Einstein*, at distances greater than a few Mpc, only unusually bright sources, with fluxes above

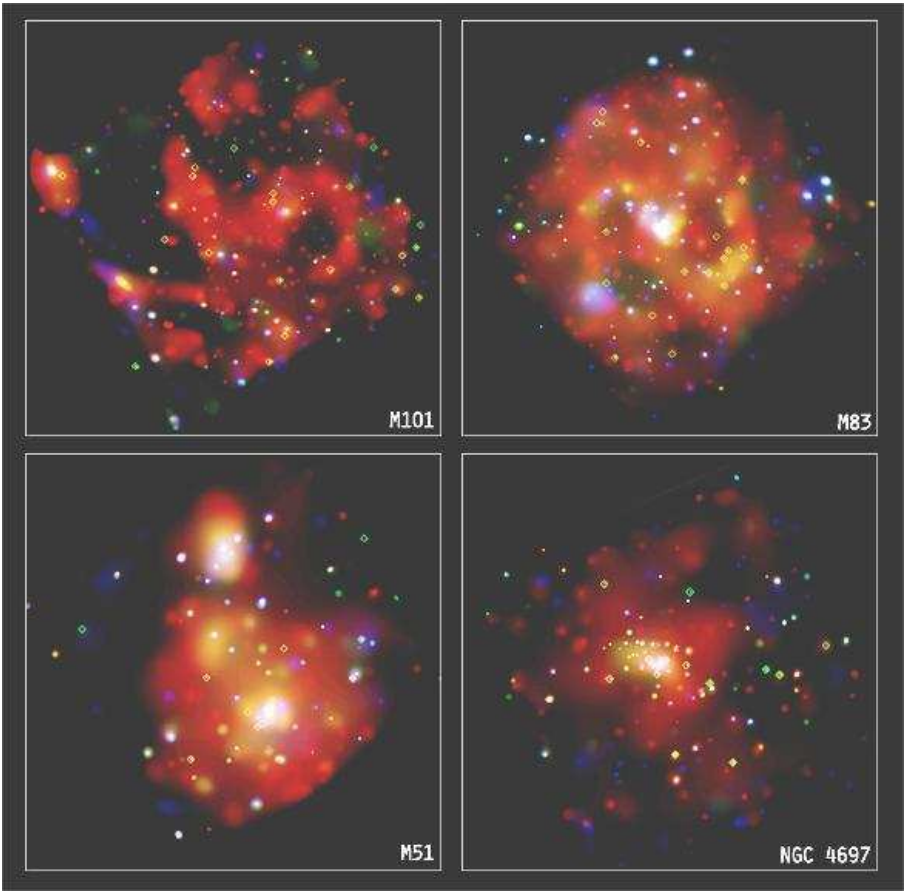

Figure 2.4: *Chandra* observations of the spiral galaxies M101, M83, M51, and NGC 4697 (http://chandra.harvard.edu/photo/2004/m101/more.html).

$\sim 10^{38}$ erg s^{-1} were detectable (Charles & Seward 1995), and most of the bright accretion-powered binaries could not be seen.

The new generation of X-ray telescopes, such as *Chandra* and *XMM-Newton*, have higher angular resolution and flux sensitivity. Now discrete X-ray sources in galaxies beyond the Local Group can be detected and analysed, while the inventory of sources detected inside the Local Group or in external galaxies increased significantly.

2.5.3.1 NGC 2403

Located at a distance of 3.2 Mpc, NGC 2403 is a spiral galaxy which is almost face-on oriented. Before *Chandra*, only 5 discrete sources were known to exist in the Galaxy. Schlegel & Pannuti (2003) analysed the galaxy using *Chandra* data and detected 41 sources having 0.5–10 keV luminosities in the range of 10^{36}–10^{39} erg s^{-1}. The brightest one is a ultraluminous X-ray source (ULX) having a bolometric luminosity of 2×10^{39} erg s^{-1}. One X-ray source is clearly associated with a SNR, for 3 others the association is far less robust.

2.5.3.2 NGC 6946

NGC 6946 is a spiral galaxy at a distance estimated between 5.1 and 5.9 Mpc. Using *Einstein*, *ROSAT* and ASCA data, only 14 X-ray sources were detected. Holt et al. (2003), using *Chandra* observations, detected 72 X-ray sources, from which 10 have 0.5–5 keV luminosities comparable with or in excess of the Eddington luminosity for a 1.4 $M_\odot$ neutron star.

2.5.3.3 M 83

M83 is a spiral galaxy of type SAB(s)c, almost face-on oriented. The last estimate of the distance was of 3.7 Mpc (de Vaucouleurs et al. 1991). Soria & Wu (2003) identified 127 discrete sources, using *Chandra* observations, with a detection limit of 3×10^{36} erg s^{-1} in the 0.3–8.0 keV band. They classified the sources in three groups according to their colors: SSSs, SNRs and X-ray binaries (more informations are given in section 4.4). They analysed the X-ray spectral and time-variability properties of the 20 brightest sources. Two of them are identified with SNR candidates, two with X-ray pulsar candidates and one with a background radio galaxy.

2.5.3.4 M 51

The spiral galaxy NGC 5194 and its companion NGC 5195 together represent M 51. The galaxy, seen almost face-on, is located at a distance of 8.4 Mpc. In *ROSAT* observations 8 individual sources were detected with 0.2–2.2 keV luminosities from 5 to 29×10^{38} erg s^{-1} (Marston et al. 1995). The galaxy has been reobserved with *Chandra* (Terashima & Wilson 2004): 111 sources have been detected, 84 of them in NGC 5194 and 12 in NGC 5195. Nine sources are ultraluminous, with luminosities exceeding 10^{39} erg s^{-1} in the 0.5–8.0 keV band. This number is much higher than what is commonly found in most spiral galaxies.

2.5.3.5 M 101

M 101 is again a face-on galaxy, located at a distance of 7.2 Mpc. 108 X-ray sources were detected by Jenkins et al. (2005) using *XMM-Newton* data. 20 of them are

coincident with H II regions and/or SNRs, 7 have been identified or are candidates for background galaxies, 6 are coincident with foreground stars and one has a radio counterpart. They estimate the X-ray binary population to represent about 60% of the catalogue although there is source contamination for background AGNs. Jenkins et al. (2004) have studied the spectral and temporal properties for the 14 most luminous objects, all having luminosities which are higher than the Eddington luminosity for a 1.4 $M_{\odot}$ neutron star. The nature of these sources have not been identified, however the sources appear to be a heterogeneous population. If the sources were black hole X-ray binaries, their intrinsic luminosities (3.4×10^{38}–3.4×10^{39} erg s^{-1}) imply black hole masses of 2–23 $M_{\odot}$. From the spectral analysis, there is no apparent spectral diferences between those sources above and below the luminosity threshold. This implies that these sources are seen at the extreme high-luminosity end of a 'normal' XRB population.

Chapter 3

Optical and X-ray observations of NGC 300

3.1 Introduction to NGC 300

NGC 300 is a spiral galaxy of type SA(s)d, located at a distance of 1.88 Mpc (Gieren et al. 2005), in the prominent Sculptor group of galaxies in the southern constellation of that name. The Sculptor group is the nearest galaxy group to the Local Group containing five major spiral galaxies (NGC 55, NGC 247, NGC 253, NGC 300 and NGC 7793) and about 20 dwarf galaxies (Cote et al. 1997).

NGC 300 is a big object in the sky, it extends over a diameter of almost 25 arcmin: the major axes of the D_{25} optical disk (defined by the extent over which the blue magnitude is lower than 25 mag) are 13.3 kpc and 9.4 kpc ($22' \times 15'$; de Vaucouleurs et al. 1991). It is a rather bright and nearly face-on. Studies of the galaxy are also simplified by its low Galactic column density ($N_{\rm H} = 3.6 \times 10^{20}\,{\rm cm}^{-2}$; Dickey & Lockman 1990).

Its vicinity and its face-on orientation provide astronomers a wonderful opportunity to study in detail its structure as well as its various stellar populations and the interstellar medium. Some properties of the galaxy are shown in Table 3.1.

Studies of the NGC 300 stellar population improved with optical images obtained with the Wide-field Imager (WFI) on the MPG/ESO 2.2 m telescope at the La Silla Observatory. With its large field of view (34×34 arcmin^2), the WFI is optimally suited to show the full extent of the spiral galaxy NGC 300 and its immediate surrounding in the sky (see Fig. 3.1).

More information as well as the ESO images from the next sections, can be found at `http://www.eso.org/outreach/press-rel/pr-2002/phot-18-02.html`.

Table 3.1: Basic informations of NGC 300

Parameter	Value	References
Type	SAs(d)	de Vaucouleurs et al. (1991)
α_{J2000}	$00^h54^m53\overset{s}{.}8$	de Vaucouleurs et al. (1991)
δ_{J2000}	$-37°40'57\overset{''}{.}$	de Vaucouleurs et al. (1991)
Isophotal major diameter D_{25}	$21'.9$	de Vaucouleurs et al. (1991)
Position angle	$111°$	de Vaucouleurs et al. (1991)
Minor to major axis ratio D_{25}, b/a	0.74	Carignan (1985)
Distance, d	1.88 ± 0.05 Mpc	Gieren et al. (2005)
Inclination	$46°$	Tully (1988)
Galactic column density, N_H	3.6×10^{20} cm^{-2}	Dickey & Lockman (1990)

3.2 Optical studies of NGC 300

3.2.1 Cepheids in NGC 300 and the cosmic distance scale

Cepheids are variable stars that constitute a key element in the measurement of distances in the Universe: their luminosity is correlated with their pulsation period, which can be determined from observations. Comparing the star's flux, F, and luminosity, L, one can obtain the distance, d, to the star by the inverse square law:

$$L = 4\pi F d^2 \tag{3.1}$$

Using this method, Freedman et al. (1992), obtained the distance to NGC 300, 2.1 ± 0.1 Mpc, using 16 known Cepheid variables. Later Freedman et al. (2001) revised the distance to 2.02 ± 0.07 Mpc using the Hubble Space Telescope Key Project Cepheid data. Pietrzyński et al. (2002a) detected 117 Cepheids and 12 Cepheid candidates using the WFI observations. Gieren et al. (2005) recently updated the distance to NGC 300 at 1.88 ± 0.05 Mpc. This last value is assumed in this thesis.

Some Cepheids found by Wolfgang Gieren (Universidad de Concepcion, Chile) and collaborators during the research programme for which the WFI images of NGC 300 are shown at the centre of the markers in Fig. 3.2.

3.2.2 Star formation in NGC 300

Studies of OB associations and H II regions (clouds of ionized hydrogen, important tracers of high-mass star formation) have been performed in NGC 300 (see below). OB associations constitute groups of young massive gravitationally unbound stars, which have been formed in the same molecular cloud. Observations of these objects provide valuable information about regions of recent and/or current star formation, their parent galaxies and star formation in general (Pietrzyński et al. 2001a). The

Figure 3.1: Colour-composite image of NGC 300 and the surrounding sky field, obtained in 1999 and 2000 with the Wide-Field Imager (WFI) on the MPG/ESO 2.2-m telescope at the La Silla Observatory.

large number of OB associations and H II regions (see Fig. 3.3) indicate the presence of numerous and very young stellar populations in NGC 300.

117 OB associations have been found by Pietrzyński et al. (2001a), while Bresolin et al. (2002) detected 70 blue supergiant candidates. Furthermore Deharveng et al. (1988a) presented a catalogue of 176 H II regions in NGC 300, and Soffner et al. (1996a) identified 88 regions in its central part.

Figure 3.2: Cepheid type stars in the spiral galaxy NGC 300 (at the centre of the markers). They were identified by Wolfgang Gieren and collaborators during the research programme for which the WFI images of NGC 300 were first obtained.

3.2.3 Wolf-Rayet Stars and Supernova Remnants

Wolf-Rayet (WR) stars were first discovered by C. Wolf and G. Rayet in 1867 (Wolf & Rayet 1876). These stars are hot, massive and luminous with anomalously strong and wide emission lines. They are believed to have lost their hydrogen envelopes and they are loosing mass through powerful stellar wind. WR stars are often found in binary systems. Schild & Testor (1991) found 40 candidates for WR stars in NGC 300 and Schild et al. (2003a) 58 candidates (from which 22 are confirmed WR stars). Breysacher et al. (1997) also have studied the WR stars detected in five associations.

Studies of supernova remnants (see section 2.2) within NGC 300 in optical, radio and X-ray wavelengths have been performed by Pannuti et al. (2000a), who found 16 new SNR candidates with respect to the previous research from Blair & Long (1997a) in the optical band (who found 28 SNR candidates). Payne et al. (2004a)

Figure 3.3: NGC 300, seen through the narrow optical filter H-alpha. Clouds of ionized hydrogen gas ("H II shells"), produced by the radiation and strong stellar winds of bright and young stars, can be seen in this photo. The "rings" near some of the bright stars are caused by internal reflections in the telescope.

re-investigated these candidates in a multi-frequency study and report 18 SNRs and 3 SNR candidates, which include the 6 SNRs seen by Read & Pietsch (2001) in X-rays.

3.2.4 Optical observations used for this study

For this study I used optical data retrieved from the ESO archive. The observations have been made by the Wide-Field Imager (WFI) on the 2.2 m MPG/ESO telescope on La Silla, Chile, for the ARAUCARIA project (Pietrzyński et al. 2002a). NGC 300 was observed by this instrument between 1999 July and 2000 January.

The reduction of these optical data was performed, in the framework of the Garching-Bonn Deep Survey, by Schirmer et al. (2003), who also comment extensively on the

data reduction. NGC 300 was observed during 34 nights, which resulted in exposure times of 11 hours (110 images), 10.4 hours (105 images), and 4.2 hours (42 images), in the B, V, and R filters, respectively.

The observations were centered on $\alpha_{\rm J2000.0} = 00^{\rm h}54^{\rm m}50^{\rm s}$, $\delta_{\rm J2000.0} = -37°40'00''$ with a field of view of $34' \times 34'$ and the average seeing in the B, V, and R data was $1\farcs1$, $1\farcs1$ and $1\farcs0$, respectively. The absolute astrometric accuracy of the optical images is about 0.25 arcsec and the relative astrometry accuracy is about 10 times better.

3.3 X-ray studies of NGC 300

Studies of the X-ray population of spiral galaxies other than our Galaxy are of special importance for the understanding of the formation of X-ray binaries and other X-ray emitting sources.

The first X-ray population study of NGC 300 was performed between 1991 and 1997 with a total of five *ROSAT* pointings. The total exposure time of these data, which were reported by Read & Pietsch (2001), was 46 ksec in the *ROSAT* Position Sensitive Proportional Counter and 40 ksec in the *ROSAT* High Resolution Imager, all with a nominal pointing position of $\alpha_{\rm J2000.0} = 00^{\rm h}54^{\rm m}52\fs0$ and $\delta_{\rm J2000.0} = -37°41'24\farcs0$. In these observations, a total of 26 sources was discovered within the D_{25} disk, the brightest being a black hole candidate with $L_{\rm X} = 2.2 \times 10^{38}\,{\rm erg\,s^{-1}}$ in the 0.1–2.4 keV band. They also identified a highly variable supersoft source and other bright sources coincident with known SNRs and H II regions. The luminosity of the residual X-ray emission, probably due to unresolved sources and genuine diffuse gas, has been estimated to be $L_{\rm X} = 1.2 \times 10^{38}\,{\rm erg\,s^{-1}}$ (Read & Pietsch 2001).

More recently, NGC 300 was observed with *XMM-Newton* on 2000 December 26 during *XMM-Newton*'s revolution 192 and 6 days later during revolution 195. Some previous results of these observations were presented by Kendziorra et al. (2001) and Carpano et al. (2004). Data on the luminous supersoft X-ray source XMMU J005510.7−373855 in the center of NGC 300 were presented by Kong & Di Stefano (2003a). From their research, this source appears to be very soft (kT ∼ 60 eV) and very luminous (10^{38} –$10^{39}\,{\rm erg\,s^{-1}}$). Their study also reveals that the source went from a "high" state to a "soft" state in 6 days. During the low state they observed a periodicity of 5.4 hr. A white dwarf, neutron star and black hole models are considered to explain the nature of that source.

Global properties of the X-ray sources detected in NGC 300's field, using *XMM-Newton* data, and their optical counterparts are given in Carpano et al. (2005). Some of the results are included in this thesis.

3.3.1 X-ray observations used in this study and data reduction

Data of NGC 300 X-ray sources contained in this dissertation have been extracted from the *XMM-Newton* data. During orbits 192 and 195 NGC 300 has been observed for 37 ksec and 47 ksec, respectively. For both observations, all three EPIC cameras were operated in their full frame mode with the medium filter. The aimpoint of the EPIC-pn camera was centered on NGC 300, using the same position as that of the earlier *ROSAT* data. Fig 3.4 shows the merged X-ray raw image from both orbits and all three EPIC cameras in the 0.3–6.0 keV energy band.

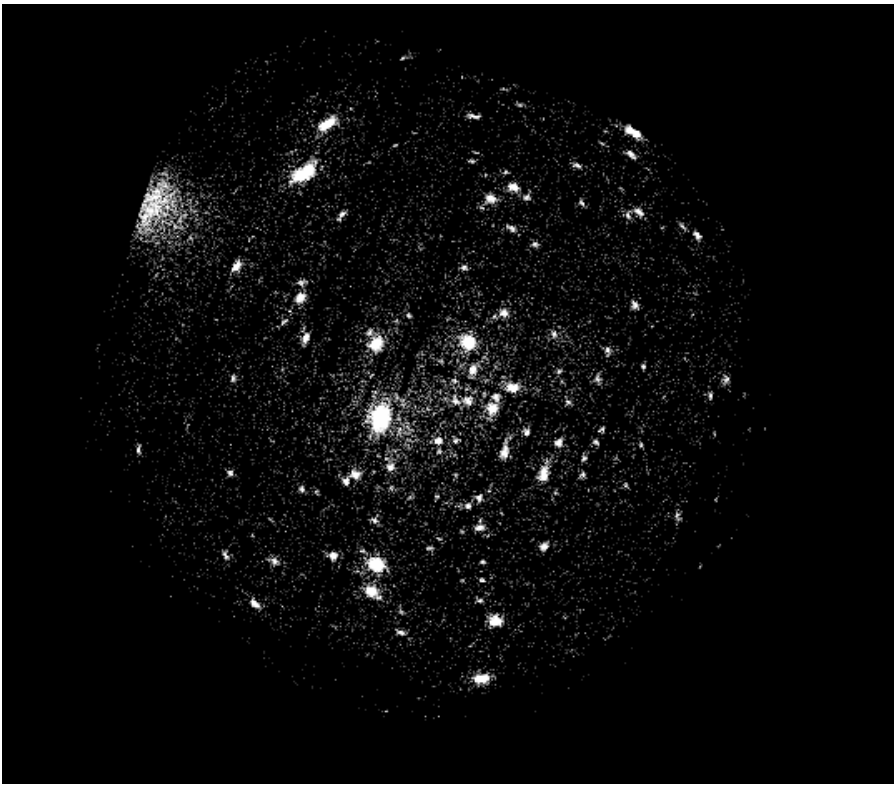

Figure 3.4: Merged X-ray raw image from both orbits and all three EPIC cameras in the 0.3–6.0 keV energy band.

In revolution 192, *XMM-Newton* was exposed to a high low energy proton flux, increasing the background in the pn camera by more than a factor of 15 (with respect

to the low background) during the last third of the observation. A light curve in the MOS1 was generated (Fig 3.5), and all time intervals with more than 140 counts (slightly larger than the quiet background level) were excluded from further analysis. The good-time-intervals extracted from the MOS light curve for revolution 192 were also used to filter the event list of the pn-camera, leaving 30 ksec of low background data for each of the three cameras. The particle background during revolution 195 was low, resulting in net observing times of 43 ksec for the two MOS cameras and 40 ksec for the pn-camera.

I reduced the data using the standard *XMM-Newton* Science Analysis System (SAS), version 6.1.0, using the `epchain` task for the EPIC-pn and `emchain` for the MOS cameras. These scripts process all first-level EPIC PN and MOS tasks, respectively, to produce calibrated event lists for all selected exposures.

Spectra, images and light curves were extracted using `evselect`, which filters the event lists by user-specified selection criteria, and extracts images, spectra, and time series from the filtered event list. I only consider events measured in regions away from the CCD borders or bad pixels, and only single and double events for the pn camera and single to quadruple events for the MOS cameras. The different possible patterns defined by an event, striking one single pixel or several adjacent pixels, are shown in Fig 3.6 and Fig 3.7 for MOS's and pn cameras, respectively.

Analysis of EPIC spectra is performed by the software XSPEC (Arnaud 1996). More informations can be found in section 6.1. The spectral fitting technique used by XSPEC requires a characterization of the EPIC detector response to simulate an output spectrum. This response function can be calculated as a product of a Redistribution (or Response) Matrix File (RMF) by an Auxiliary (or Ancilliary) Response File (ARF). The RMF and ARF files are created with the `rmfgen` and `arfgen` tasks using the newest available calibration files.

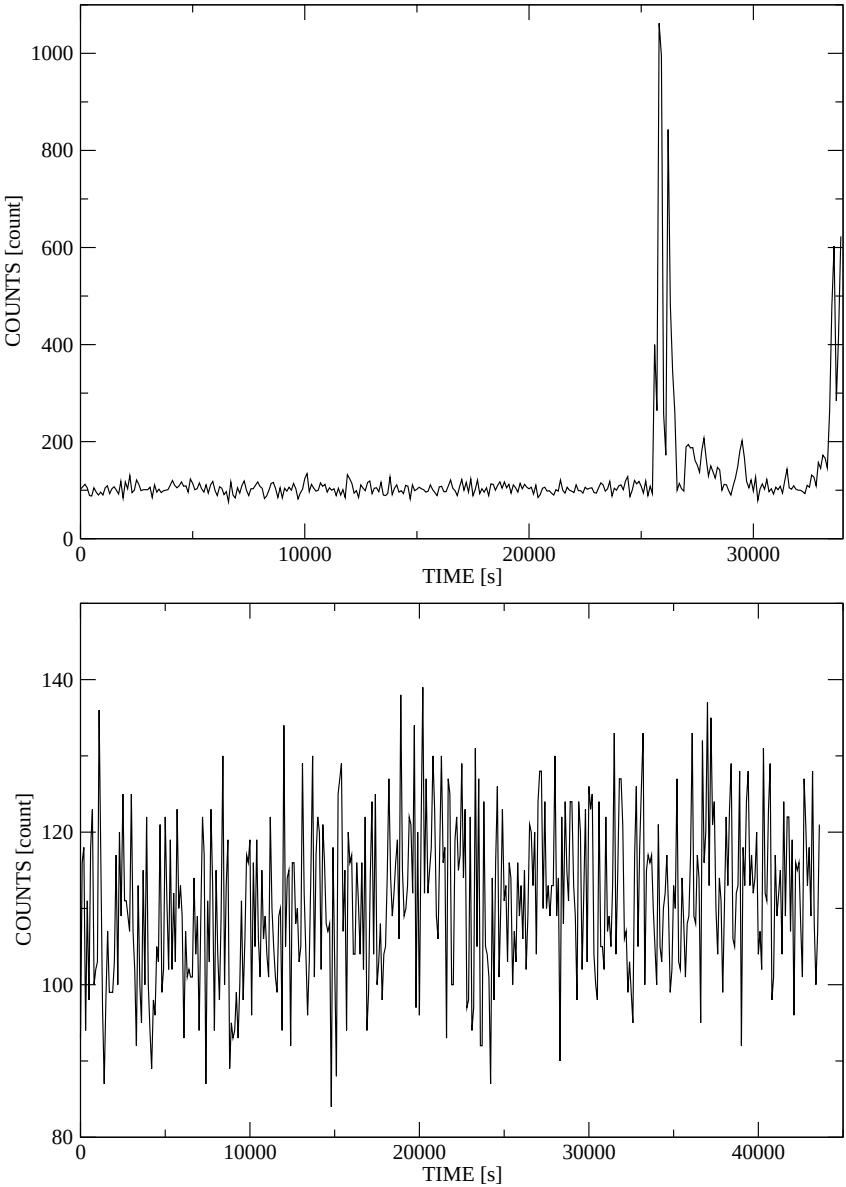

Figure 3.5: Light curve of the full MOS1 image, in the 0.3–6.0 keV band, with a binning size of 100 sec, during revolution 192 (top) and revolution 195 (bottom). High energy proton flux are observed during revolution 192 around 26000 sec and 34000 sec from the beginning of the observation.

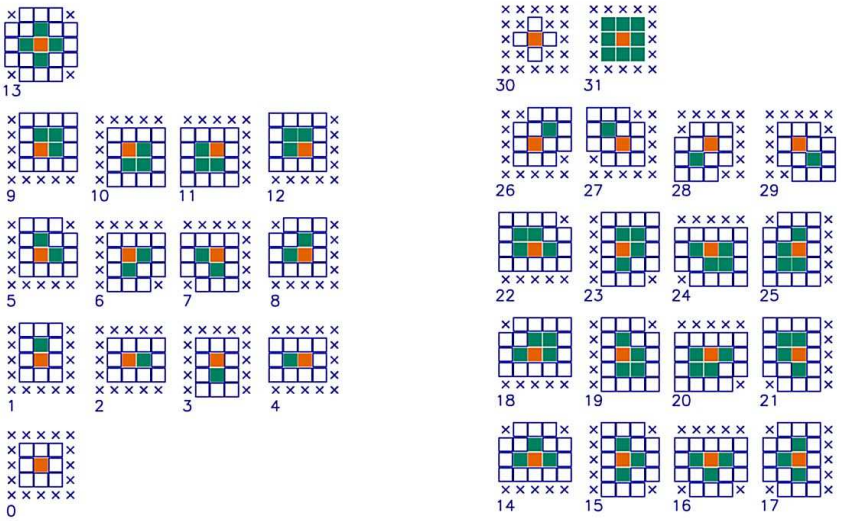

Figure 3.6: List of the EPIC-MOS patterns: each pattern is included in a 5 x 5 matrix and is centered on the pixel of highest charge. This central pixel is colored in red, the other pixels above the threshold in the pattern are colored in green, all pixels below the threshold are in white, and the crossed pixels are indifferent. The best patterns should contain the highest charge in the center, surrounded by pixels below the threshold (patterns 0-25). Patterns 26-29 are called diagonal patterns and are not expected from a genuine X-ray event (Ehle et al. 2004b).

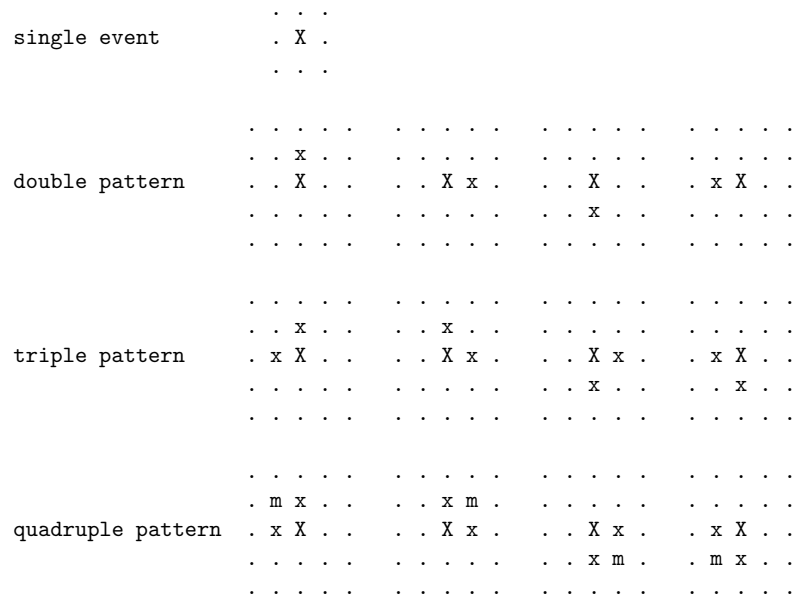

Figure 3.7: List of the valid EPIC-pn patterns (see Fig.3.6 for more details). The "." mark indicates a pixel without an event above the threshold, "X" corresponds to the pixel with the maximum charge, "x" with a non-maximum charge, and "m" is the pixel with the minimum charge. These 13 figures refer to the SAS PATTERN codes 0 (singles), 1-4 (doubles), 5-8 (triples) and 9-12 (quadruples), respectively (Ehle et al. 2004b).

Chapter 4

X-ray source properties

4.1 Source detection

The first step of the analysis consists of searching for all possible X-ray point sources in the NGC 300 data. Event and attitude files of each instrument were merged for both orbits 192 and 195 using the `merge` task, which merges EPIC event lists and attitude files from two observations if the two pointings are close enough (the accuracy of the reprojection degrades with the offset between the two pointings). This approach is valid since both observations have the same pointing direction and the difference in position angles between the two observations is very small and consequently the effect of the varying point spread function of *XMM-Newton* on the resulting image is small.

Point source detection was then performed using a maximum likelihood approach as implemented by the SAS-tool `edetect_chain`. The output is a merged source list in FITS format which lists, for each detected source: the source identification number, the instrument and energy band where it was detected, the source counts, source position and extent, source flux and count rate as well as hardness ratios.

I ran this tool simultaneously on the three cameras, setting a maximum likelihood (ML) threshold of 10 in the 0.3–6.0 keV band. This correspond to the probability $P = 1 - \exp(-\mathrm{ML}) = 0.999955$ for the existence of the source and a Gaussian significance of 4.0σ. After removing sources associated with the galaxy cluster CL 0053−37, a total of 163 sources were found, of which 86 sources are within the D_{25} optical disk (Carpano et al. 2005). As will be shown in section 4.5, the detection limiting flux in the 0.3–6.0 keV energy band is $F_{0.3-6} \sim 1 \times 10^{-15}\,\mathrm{erg\,cm^{-2}\,s^{-1}}$ for sources inside the optical disk.

I adaptively extract source and background regions with the SAS `region` task, which is using an elliptical locus to approximate the spatially varying point spread function. The procedure uses an analytical model of the PSF which gives an elliptical shape for the flux contours of the form (`http://xmm.vilspa.esa.es/sas/`

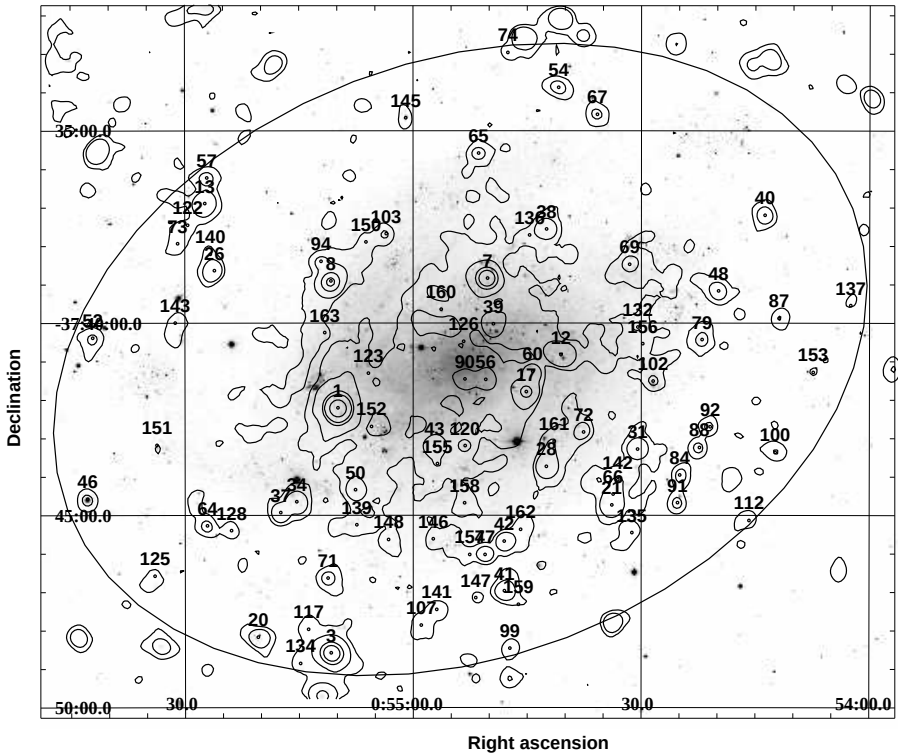

Figure 4.1: Optical image of NGC 300 in the visible band overlaid by a contour map of the merged 0.3–6.0 keV raw X-ray image from all three EPIC cameras and from both orbits. The D_{25} optical disk and the sources detected inside the disk are also shown.

current/doc/region/node8.html):

$$\mathrm{PSF}(x,y) = A\,\exp\left(-\frac{x^2+[y/s]^2}{2\sigma^2}\right) + \frac{(1-A)}{(x^2+[y/s]^2)^{\alpha}} \tag{4.1}$$

where A, σ, s and α depend on the source position in the field of view (FOV).

Fig. 4.1 shows the V band optical image of NGC 300, from the ESO archive of the Garching-Bonn Deep Survey and the contour map of the merged X-ray raw image from both orbits and all three EPIC cameras in the 0.3–6.0 keV energy band. The D_{25} optical disk and the sources detected inside the disk, which are numbered in order of decreasing X-ray count rate as determined by the `edetect_chain`, are also shown.

A summary of the properties of these detected sources as well as their possible optical counterparts is given in Section 5.1.

4.2 Color-color diagram and X-ray fluxes

Any classification of the detected sources as well as the determination of the source flux require an understanding of the spectral shape of the sources. Due to the low count rates of most detected sources, formal spectral modeling is only possible for a few of the brightest sources (these fits will be shown in section 6.3). I therefore rely on X-ray color-color and hardness ratio diagrams in the determination of the flux and the spectral shape.

In order to determine these quantities, I first derive the background-subtracted count rate from

$$\mathrm{CR}(I) = \frac{C(I)_{\mathrm{src}}}{T_{\mathrm{src}}} - \frac{C(I)_{\mathrm{back}} B_{\mathrm{src}}}{T_{\mathrm{back}} B_{\mathrm{back}}}, \tag{4.2}$$

where $C(I)$ is the total number of counts in channel I, T is the exposure time and B is the area from which the source and background data were extracted, as given by the `BACKSCAL` keyword, which is defined by the geometric area of the source extraction region minus the bad pixels or CCD gaps laying within that source region. The subscripts 'src' and 'back' denote the source and background, respectively.

For sources that are bright in one single energy band (e.g. for SSSs), the background-substracted total count rate in one of the three energy bands (soft, medium or hard) can sometimes be negative. If the absolute value of this negative count rate is less than 5% of the total count rate in the full energy band, then the value is set to zero and data are kept. If the absolute value is higher than 5%, the data coming from that instrument for that revolution are excluded from the hardness ratio calculation. To obtain the total count rate in each band, I average the valid count rates from all three EPIC instruments. The X-ray colors are then defined by:

$$\mathrm{HR}_{\mathrm{hard}} = \frac{H - M}{H + M + S}, \quad \text{and} \quad \mathrm{HR}_{\mathrm{soft}} = \frac{M - S}{H + M + S} \tag{4.3}$$

where S, M, and H are the total count rates in the soft (0.3–1.0 keV), medium (1.0–2.0 keV), and hard (2.0–6.0 keV) energy bands.

The uncertainty of the hardness ratio ($\Delta\mathrm{HR}^2_{\mathrm{hard}}$, $\Delta\mathrm{HR}^2_{\mathrm{soft}}$) and the source count rate ($\Delta\mathrm{CR}^2$) is determined from error propagation (unless otherwise noted, all uncertainties are at the 68% level.):

$$\Delta\mathrm{CR}^2(I) = \frac{C(I)_{\mathrm{src}}}{T^2_{\mathrm{src}}} + \frac{C(I)_{\mathrm{back}} B^2_{\mathrm{src}}}{T^2_{\mathrm{back}} B^2_{\mathrm{back}}}, \tag{4.4}$$

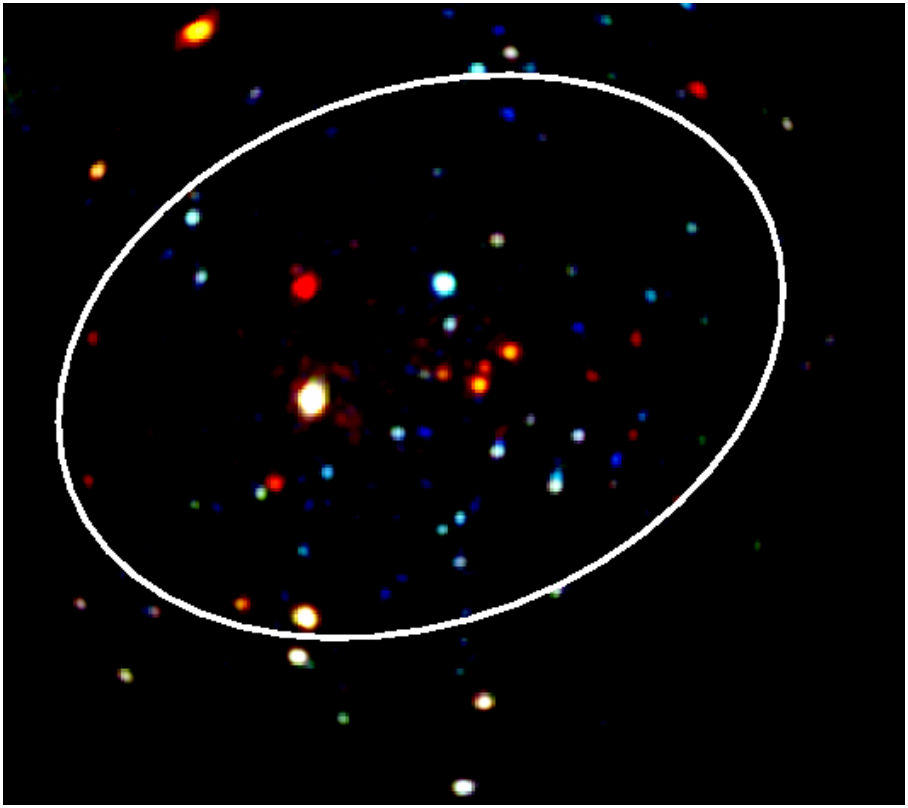

Figure 4.2: Color-composite image of the smoothed X-ray data. The soft band (0.3–1 keV) is colored in red, the medium one (1–2 keV) in green and the hard one (2–6 keV) in blue.

$$\Delta \mathrm{HR}^2_{\mathrm{hard}} = \frac{\Delta H^2 + \Delta M^2 + \Delta \mathrm{TOT}^2 (H - M)^2 / \mathrm{TOT}^2}{\mathrm{TOT}^2}, \tag{4.5}$$

$$\Delta \mathrm{HR}^2_{\mathrm{soft}} = \frac{\Delta M^2 + \Delta S^2 + \Delta \mathrm{TOT}^2 (M - S)^2 / \mathrm{TOT}^2}{\mathrm{TOT}^2} \tag{4.6}$$

with

$$\mathrm{TOT} = H + M + S \qquad \text{and} \qquad \Delta \mathrm{TOT}^2 = \Delta H^2 + \Delta M^2 + \Delta S^2,$$

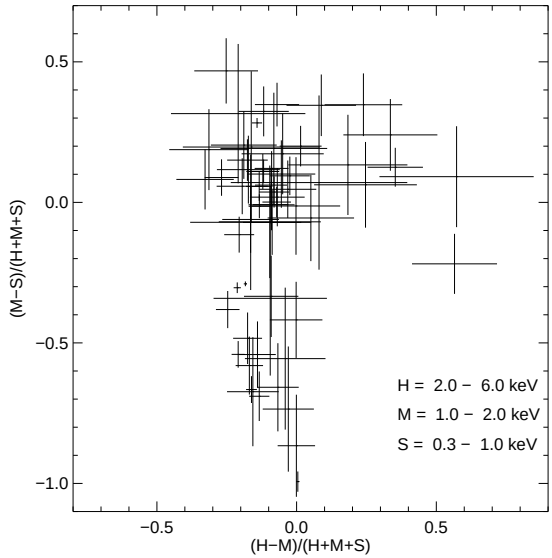

Figure 4.3: Color-color diagram of sources detected inside the D_{25} optical disk.

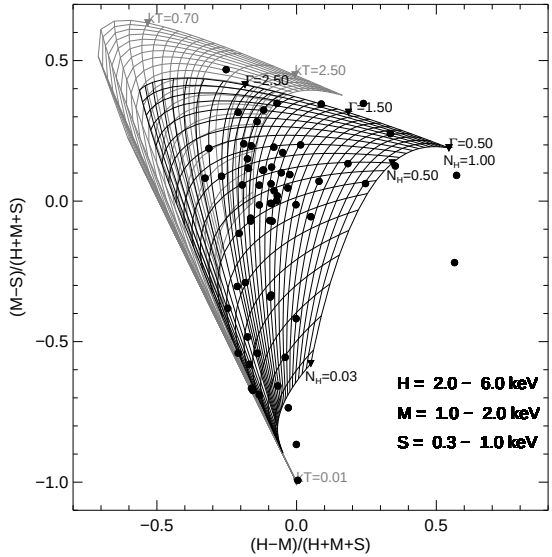

Figure 4.4: Color-color diagram of the sources detected inside the D_{25} optical disk and color-color contours for bremsstrahlung and power law plus 0.2 keV bremsstrahlung component. The equivalent hydrogen column, $N_{\rm H}$, is given in units of 10^{22} cm^{-2} and is associated to the lines that are mainly 'horizontal'. The temperature of the bremsstrahlung spectrum, kT, is given in keV and, as the Γ parameter, are associated to lines that are mainly 'vertical'. The triangles indicate the lines to which the parameter value is associated.

and

$$\Delta X^2 = \sum_{I=1}^{N_X} \Delta \mathrm{CR}^2(I)$$

where X can be H, M, or S and N_X is the number of channels for the corresponding energy range.

Fig. 4.2 shows a color-composite image of the smoothed X-ray data. The soft band is colored in red, the medium one in green and the hard one in blue. Fig. 4.3 shows the resulting color-color diagram for the X-ray sources inside the D_{25} optical disk, excluding sources having less than 20 net counts. In Fig. 4.4, I compare these data with empirical color-color diagrams. I simulated two sets of spectra following a simple bremsstrahlung model and a two component source spectrum consisting of a soft bremsstrahlung (with a fixed temperature of kT=0.2keV) and a hard power law component (colors derived from simple power law models were not sufficient to describe the data). I then calculated the hardness ratio for these theoretical spectra as I did for the observed ones and plotted the results in the color-color diagram using a grid format. In these models the equivalent hydrogen column N_{H}, expressed in units of $10^{22}\,\mathrm{cm}^{-2}$, is running from 0.03 to 1.0. In the simple bremsstrahlung model the temperature kT, expressed in keV, goes from 0.01 to 5.0, and in the second model the photon index Γ from 0.5 to 4.5, keeping the temperature at 0.2 keV. Both models are sufficient to describe the data, however, the N_{H} values inferred are generally larger than the pure Galactic N_{H} in the direction to NGC 300 (which is $3.6 \times 10^{20}\,\mathrm{cm}^{-2}$, Dickey & Lockman 1990), indicating intrinsic absorption within NGC 300 and also pointing towards a possible contamination of the source sample by background AGNs. From the 2–10 keV AGN $\log N$–$\log S$-diagram of Ueda et al. (2003) (see Fig 4.5), ∼30 AGN with $F_{2-10} \geq 10^{-14}\,\mathrm{erg\,cm^{-2}\,s^{-1}}$ are expected within the D_{25}-disk, however, the identification of AGNs in the sample requires X-ray spectral analysis which is only possible for the brightest sources and dangerous in itself due to the similarity of AGN and XRB spectra.

The color-color diagram analysis shows that for all sources except one it is possible to find a best matching bremsstrahlung or power law plus bremsstrahlung model. The spectrum of the one non-matching source (#120), which is in a very complex region, is peculiar and has been excluded from the subsequent analysis.

From this best matching spectral model it is then possible to determine the flux of a source by appropriately scaling the flux determined from the spectral model to the source count rate. Note that such an approach gives generally more believable flux estimates than the more commonly used approach of assuming one fixed spectral shape for all detected sources, while not limiting one to determining spectral fluxes only for sources with sufficient counts to enable formal spectral model fitting (see also Humphrey & Buote 2004).

The uncertainties of the flux are derived as follows. I first determined the error associated with the flux, considering only Poisson noise. I then estimated the error of the flux due to the position of the source in the color-color diagram. This was done by calculating the flux associated with the minimum and maximum values of each hardness ratio. The range over which the source flux can vary is thus determined by the minimum and maximum values of the 6 fluxes determined in the two previous steps.

Fig. 4.6 shows the source fluxes versus both hardness ratios defined by Eq. (4.3). For comparison, a source with a luminosity of $1.82\times10^{38}\,\mathrm{erg\,s^{-1}}$, close to the Eddington limit for a 1.4 $M_\odot$ object, has a flux of $4.30\times10^{-13}\,\mathrm{erg\,cm^{-2}\,s^{-1}}$ at the distance of NGC 300.

The brightest source, source 1, is found with a luminosity of $1.48\times10^{38}\,\mathrm{erg\,s^{-1}}$, which is close to the Eddington limit for a 1.4 $M_\odot$ object. The source, coincident with the previously known *ROSAT* source P42 (Read & Pietsch 2001), has been found to have a slightly lower luminosity than in the *ROSAT* observations. From its high intrinsic luminosities, this source is akin to $\sim$10 $M_\odot$ black hole in its soft state such as LMC X-1 or LMC X-3 (Nowak et al. 2001; Wilms et al. 2001). There are no clear super-Eddington X-ray sources detected in NGC 300. Finally, also note that both hardness ratios do not depend significantly on flux.

4.3 *Variability of the sources*

All sources detected inside the optical disk, for which a flux was determined, were checked for variability.

Fig. 4.7 shows the 0.3–0.6 keV flux of sources having more than 0.001 net counts $\mathrm{sec^{-1}}$ in all EPIC cameras, for both revolutions (192 in black and 195 in red). My criterium of variability is:

$$|F_{192} - F_{195}| \geq 3\sigma(F_{192} - F_{195}) \tag{4.7}$$

where F_{192} and F_{195} are the source fluxes associated to revolutions 192 and 195 respectively, and $\sigma(F_{192} - F_{195})$, is the error associated with their differences. Two sources have been found to be variable, their ID numbers are: 1 and 7.

Source #1 is the only source for which colors (hard and soft hardness ratio) are changing significantly (more than 3 σ) between revolution 192 and 195.

4.4 *Identification of the sources and comparison with other galaxies*

Fig. 4.8 (top) shows the color-color diagram for the sources detected inside the optical disk and, when available, a label indicating the counterparts found in SIMBAD,

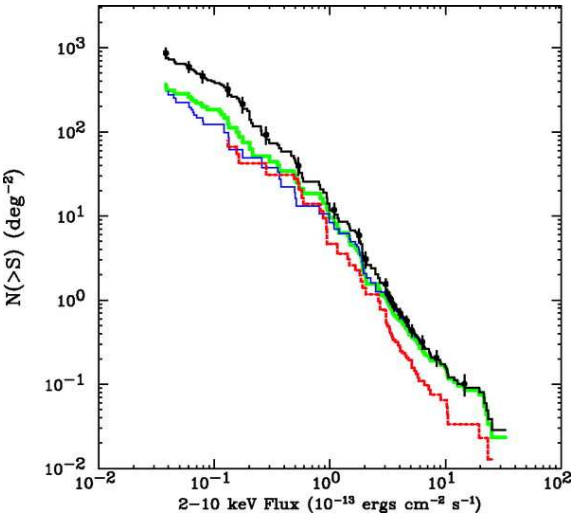

Figure 4.5: The logN–logS relation for a sample of 247 AGNs following Ueda et al. (2003) (topmost black line).

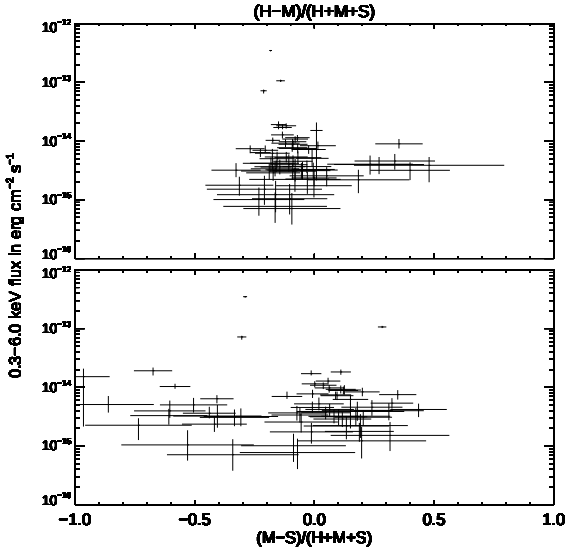

Figure 4.6: Fluxes of the sources detected inside the D_{25} optical disk as a function of the harder (top) and softer (bottom) hardness ratio defined by equation (4.3).

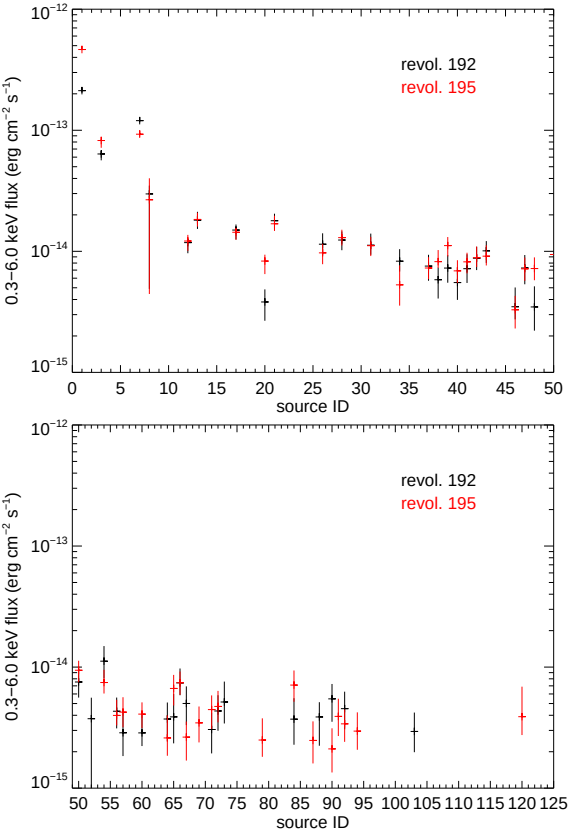

Figure 4.7: 0.3–0.6 keV flux for the brightest 50 sources (top), and for sources 50 until 125 (bottom) detected inside the optical disk, having more than 0.001 net counts sec^{-1} in all EPIC cameras, for both revolutions separately (192 in black and 195 in red).

USNO and radio catalogues (see Section 5.1 for more details about these cross-correlations). SNR are labeled with a 'S', radio sources with a 'R', H II regions with a 'H', Cepheid stars with a 'C', association of stars with a 'A', NGC 300's stars with a 'ST', Wolf-Rayet stars with a 'WR' and sources from the USNO catalogue with a 'U'. I also include the label 'SSS' to indicate the position of our supersoft source. Sources having a $\log(F_X/F_{vis}) < -1$ are labeled with a 'O'. Following Maccacaro et al. (1988) these are candidates for galactic stars, and they defined this ratio by: $\log(F_X/F_{vis}) = \log(F_X) + m_{vis}/2.5 + 5.37$ (where m_{vis} is the visual magnitude). For

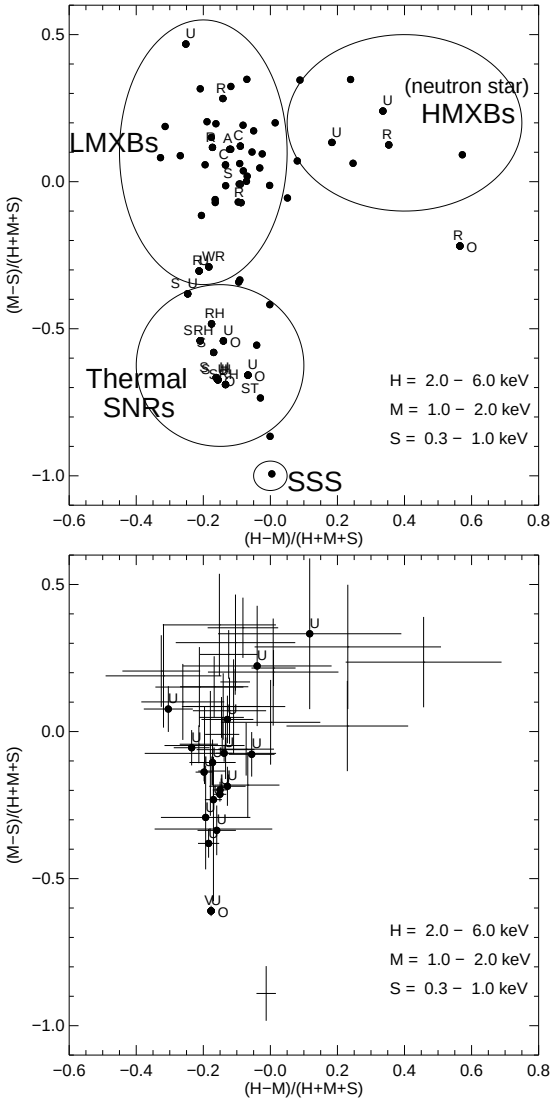

Figure 4.8: Color-color diagram for sources inside (top) and outside (bottom) the optical disk (see text for more details).

Table 4.1: Criteria used to tentatively classify the sources detected in the NGC 300 optical disk.

Source type	Criteria
fg Star	$\log(F_X/F_{vis}) < -1$ and $HR_{soft} < -0.5$ and no SNR from catalogue
AGN	$HR_{soft} > -0.35$ and radio counterpart
SSS	$HR_{soft} < -0.9$
SNR	$(-0.9 < HR_{soft} < -0.35$ and not a fg Star) or SNR from catalogue
LMXB	$-0.45 < HR_{hard} < 0.05$ and $-0.35 < HR_{soft} < 0.55$ not SNR from catalogue
NS HMXB	$0.05 < HR_{hard} < 0.75$ and $-0.10 < HR_{soft} < 0.50$

clarity, the 'S' labels are slightly shifted to the left with respect to the source, the 'H' and 'U' to the right, the 'ST' label is below the source and the 'O' label to its right.

From this diagram, we see that, except for one source, all SNR are located in a same region. SNRs dominated by non-thermal emission (Crab-like objects) are expected to have harder spectra than thermal SNRs. The brightest source (associated with a WR star), and the second brightest source (associated with a radio source just at the left, in the diagram, of the WR star), are slightly above the SNR group. Candidates for foreground stars, soft sources labeled with a 'O', are slightly on the right of the SNR region and overlap with it. The SSS is at the very bottom of the diagram and all harder sources, mainly composed of X-ray binaries and background AGNs, are spread over a large region in the upper part of the diagram. Following Prestwich et al. (2003), neutron star HMXBs are expected to be the hardest sources of this group and LMXBs the softer ones.

Fig. 4.8 (bottom) shows the same color-color diagram but for sources outside the optical disk. A foreground variable star is labeled with a 'V', and other sources have USNO counterparts. Note that the X-ray to visible flux ratio has not always been computed for foreground star candidates, as these are often so bright that the source profile cannot be determined. One source is found to be very soft and is at the bottom of the diagram.

This diagram is mainly composed of foreground stars, which are expected to be the softer sources, and by background AGNs, which are the harder sources. I also expect to find several objects belonging to NGC 300, as the X-ray disk is often extending beyond the D_{25} optical disk.

Using all these considerations I attempt to give some classification for the sources detected inside the optical disk, using the criteria given in Table 4.1. Of course this classification will only give a rough idea of each source type, as there can be over-

Table 4.2: Results of the classification according to criteria from Table 4.1. Source labels refer to the ones of Table 5.1.

Group	# of sources	Source label
fg Star	2	46, 88
AGN	6	3, 7, 54, 69, 91,120
SSS	1	8
SNR	14	12, 17, 20, 34, 52, 56, 60, 72, 79,103,112,123,126,151
LMXB	39	1, 3, 7, 13, 21, 26, 28, 31, 37, 38, 39, 40, 41, 42, 43, 47, 48, 50, 57, 64, 65, 66, 67, 69, 71, 73, 87, 90, 91, 94, 99,100,117,125,136,146,147,148,155
NS HMXB	9	74, 84, 92,107,128,132,139,142

laps between the different categories in the color-color diagram due to similar spectra and/or because of absorption. Strongly absorbed SSS can go to the SNR group, strongly absorbed SNRs can go to the LMXB group, etc. The different source types I define are: foreground stars (fg Star), background AGNs (AGN), supersoft sources (SSS), supernova remnants (SNR), low-mass X-ray binaries (LMXB) and neutron star high-mass X-ray binaries (NS HMXB).

The number of sources falling in each category as well as the corresponding source label, are given in Table 4.2. Note that 7 of the SNR candidates have SIMBAD counterparts.

4.4.1 Comparison with other galaxies

I compare the hardness ratios with those from sources detected in other spiral galaxies. Fig. 4.9 (top) shows the color-color diagram for the spiral galaxy M83 (Soria & Wu 2003). The colors are defined as in equation 4.3 but the hard energy band is going from 2.0–8.0 keV. In Fig. 4.9 (bottom), I plot the color-color diagram of NGC 300's sources using these energy bands.

Soria & Wu (2003) divided their diagram in 3 regions. Group A is dominated by the SSSs, which have negligible emission in the medium and hard band and are located around (0,−1). Group B includes sources located in a region around $-0.85 < \mathrm{HR_{soft}} < -0.15$. From their study, most of them can be fitted by a spectrum consistent with those for SNRs, although some of the sources have spectra that are also consistent with transient X-ray pulsars or old low-mass neutron star X-ray binary. Time variability is required to distinguish between these different categories. Group C is located at $-0.15 < \mathrm{HR_{soft}} < 0.6$ with a much broader spread in $\mathrm{HR_{hard}}$. They believe that most of the sources in this group are X-ray binaries, although a few hard, highly-absorbed sources may be background AGN. Such kind of division

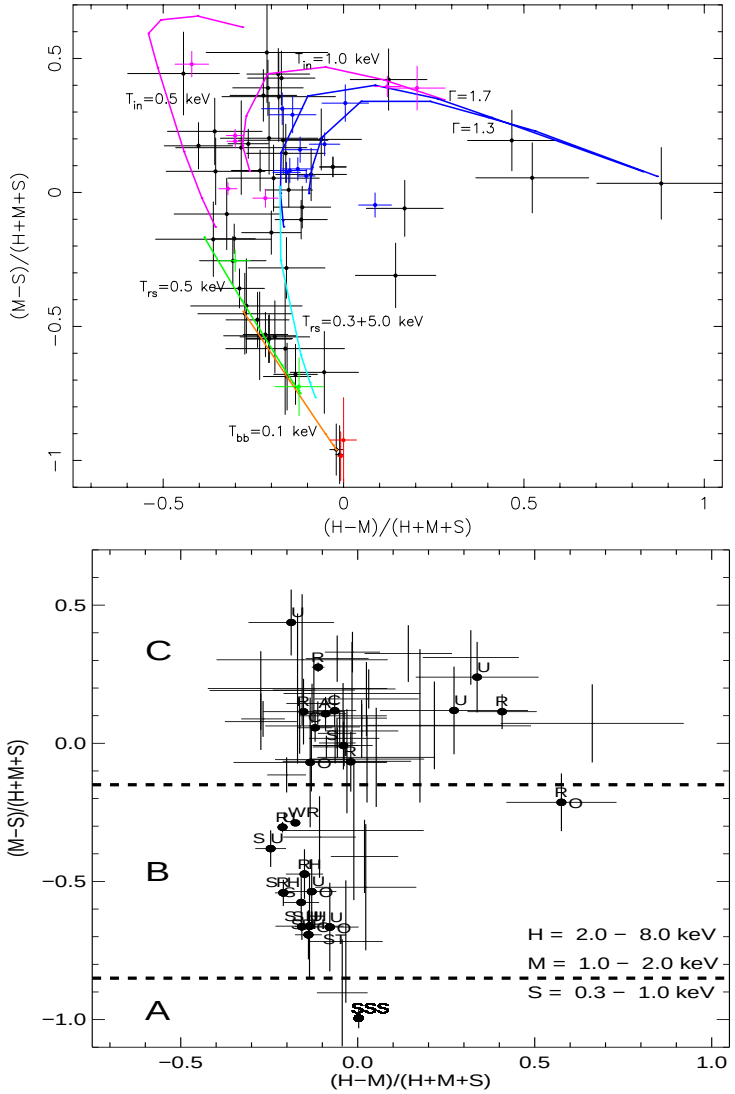

Figure 4.9: Color-color diagram for spiral galaxy M83 (Soria & Wu 2003) (top) and for NGC 300 (bottom) using the same energy bands.

is consistent with my data and correlations from catalogues.

Fig. 4.10 (top) shows the color-color diagram for the spiral galaxy M101 (Jenkins et al. 2005). Their hardness ratio definition is: HR_1=(M−S)/(M+S) and HR_2=(H-M)/(H+M), where the energy bands S, M and H are the same as mine. In Fig. 4.10 (bottom), I plot the hardness ratio of NGC 300's sources using their hardness ratio definition.

Jenkins et al. (2005) classified their sources in 6 groups: supernova remnants (SNR), X-ray binaries (XRB), background sources (BKG SRC), absorbed sources (ABS SRC), indeterminate soft sources (IND SS) and indeterminate hard sources (IND HS), according to the following criteria:

- SNR: $HR_1 < -0.24$ and $HR_2 < -0.10$
- XRB: $-0.24 < HR_1 < -0.57$ and $-0.8 < HR_2 < 0.8$
- BKG SRC: $HR_1 < -0.24$ and $HR_2 > -0.10$
- ABS SRC: $HR_1 > -0.5$
- IND SS: $-0.24 < HR_1 < -0.57$ and $HR_2 < -0.8$
- IND HS: $-0.24 < HR_1 < -0.57$ and $HR_2 > 0.8$

My SNR candidates are located in the same region, while in the XRB group I expect to find also background AGN. From their criteria my 2 brightest X-ray sources (labeled with WR and R,U around $(-0.5, -0.3)$), which are X-ray binary candidates, are not included in the XRB group, and in the background sources region I find one of my AGN candidates (source #120, labeled with R,O). From their simulations of a 175 eV blackbody spectrum, they predict the position of SSSs around $HR_1 = -0.66$ and $HR_2 = -0.98$ which is far away from the location of my SSS.

Prestwich et al. (2003) classified X-ray sources in external galaxies from the color-color diagram. Using the same hardness ratio definition as me, but working in the hard energy band up to 8 keV, they show that there is a difference in the X-ray colors of sources in bulge systems, where all sources are confined in the $-0.4 < HR_1 < +0.4$ and $-0.4 < HR_2 < +0.4$ region, and disk galaxies, where there is also a population of soft and hard sources not seen in bulges. Their sample consists of 2 spiral galaxies (M101 and M83) and three elliptical/bulge systems (NGC 4697, the inner bulge of M31, and the bulge of NGC1291). Fig. 4.11 shows the hardness ratio of all sources found in the sample of galaxies. As the bulge of our Galaxy and M31, as well as sources in elliptical galaxies are dominated by low-mass X-ray binaries, I expect to find them in the $-0.4 < HR_1 < +0.4$ and $-0.4 < HR_2 < +0.4$ region. The soft sources ($-0.9 < HR_1 < -0.4$) present mainly in the spiral galaxies are expected to be thermal SNRs (Crab-like SNRs are expected to have harder spectra) and super soft sources are around $HR_2 = 0$ and $HR_1 = -1$. The hard sources ($HR_2 > 0$) that appear in the disk but not in the bulge are candidates for neutron star high-mass X-ray binaries (black hole high-mass X-ray binaries are expected to have spectra similar to the black hole LMXBs). In that region known binary pulsars are found (Yokogawa

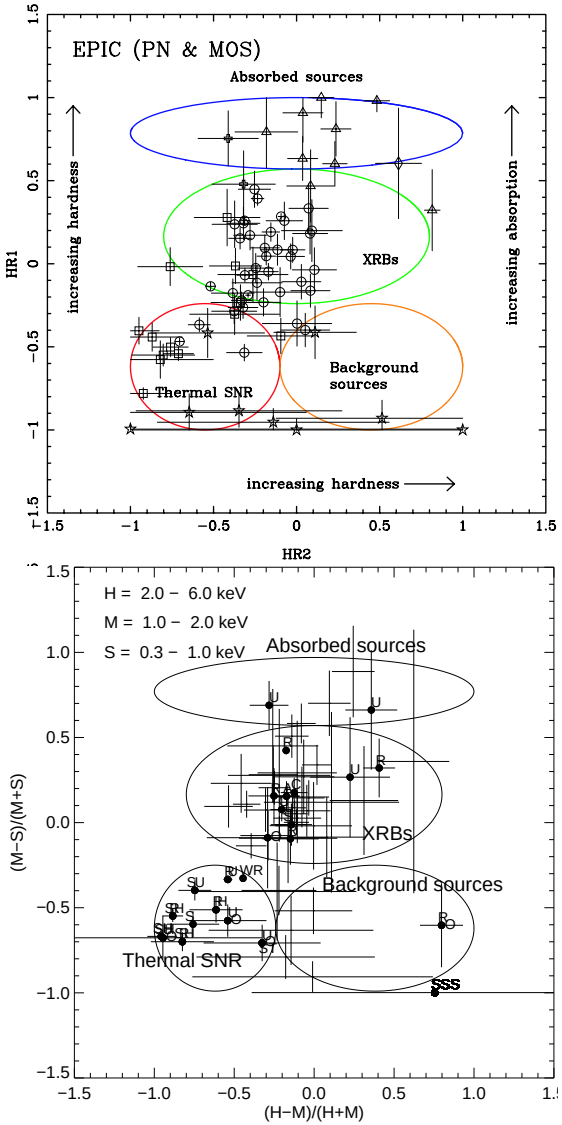

Figure 4.10: Color-color diagram for spiral galaxy M101 (Jenkins et al. 2005) (top) and for NGC 300 (bottom) according to their hardness ratio definition.

et al. 2000). Their classifications from hardness ratio are similar to mine, so we have good agreement with the NGC 300's data.

Fig. 4.12 and Fig. 4.13 show the color-color diagrams for the Local group galaxy M31 (Pietsch et al. 2005) and M33 (Pietsch et al. 2004), respectively. Foreground stars and candidates are marked as big and small stars, galaxies and candidates as big and small X, AGN candidates as crosses, SSS candidates as triangles, SNR and candidates as big and small hexagons and X-ray binaries as squares (see papers for more details). Their hardness ratios are defined by: $HR_i=(B_{i+1}-B_i)/(B_{i+1}+B_i)$, where $i = 1$ to 4 and B_i denotes the count rate in band i. These are defined as: B_1=0.2–0.5 keV, B_2=0.5–1.0 keV, B_3=1.0–2.0 keV, B_4=2.0–4.5 keV and B_5=4.5–12 keV. Fig. 4.14 shows the corresponding color-color diagram for sources in NGC 300.

They use the following criteria for identification of the sources as foreground stars (fg star), AGNs, SNRs, X-ray binaries (XRB), and hard sources (hard), note that small differences exist between M31 and M33 criteria:

- fg Star: $\log(F_x/F_{vis}) < -1$ and $HR_2-EHR_2 < 0.3$ and $HR_3-EHR_3 < -0.4$ or not defined
- AGN: radio sources and not classification as SNR
- SSS: $HR_1 < 0.0$ and HR_2-EHR_2 < -0.99 or HR_2 not defined, HR_3, HR_4 not defined
- SNR: $HR_1 > -0.1$ and $HR_2 < -0.2$ and not a fg Star, or id with optical/radio SNR
- XRB: optical id X-ray variability
- hard: $HR_2-EHR_2 > -0.2$ or only HR_3 and/or HR_4 defined and no other classification

where $\log(F_x/F_{vis}) = \log(F_x) + (m_B + m_R)/(2 \times 2.5) + 5.37$, following Maccacaro et al. (1988), with m_B and m_R being the optical magnitudes in the blue and red band.

Comparing the diagrams with my data, we see that the first plots are well suited for the separation between SSSs, SNRs and harder sources and have correspondance with the diagrams of Pietsch et al. (2004, 2005), while the third plots are not really adequate for my data since the error bars are too large.

4.4.2 Conclusions

All the classification criteria used in these other galaxies are well suited to distinguish between the SSSs, the thermal SNRs (which are the softer sources) and the harder X-ray binaries. Prestwich et al. (2003) went deeper in the classification and separated the hard X-ray binaries in the LMXBs (softer ones) and neutron star HMXBs (harder ones), while Jenkins et al. (2005) found some color criteria to locate the background sources.

My classification criteria are well suited to distinguish between SSSs, thermal SNRs, X-ray binaries and foreground stars. However, as the other criteria, they are

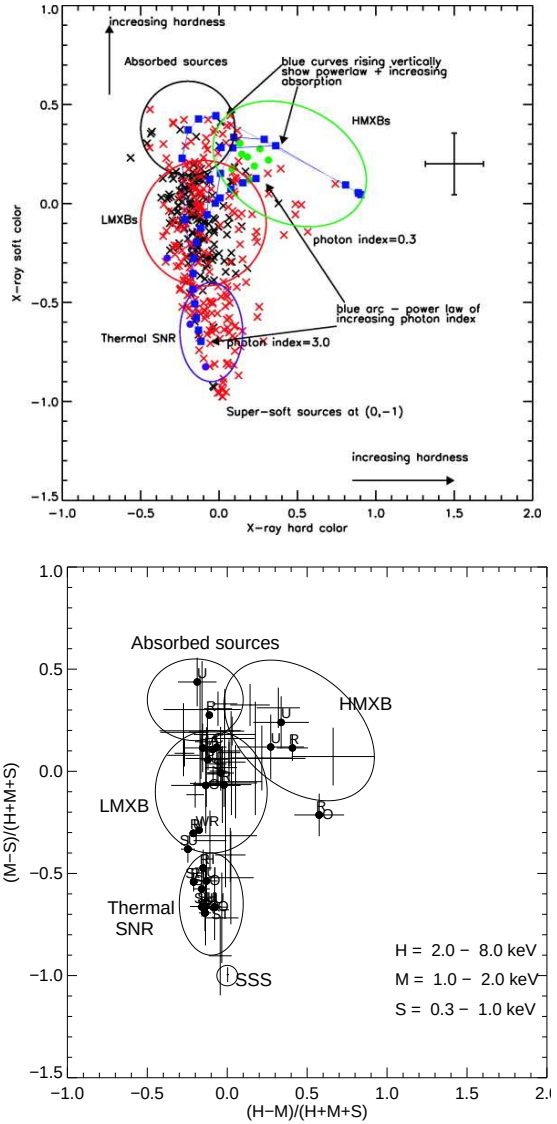

Figure 4.11: Color-color diagram for nearby galaxies (Prestwich et al. 2003) (top) and for NGC 300 (bottom) according to their energy band.

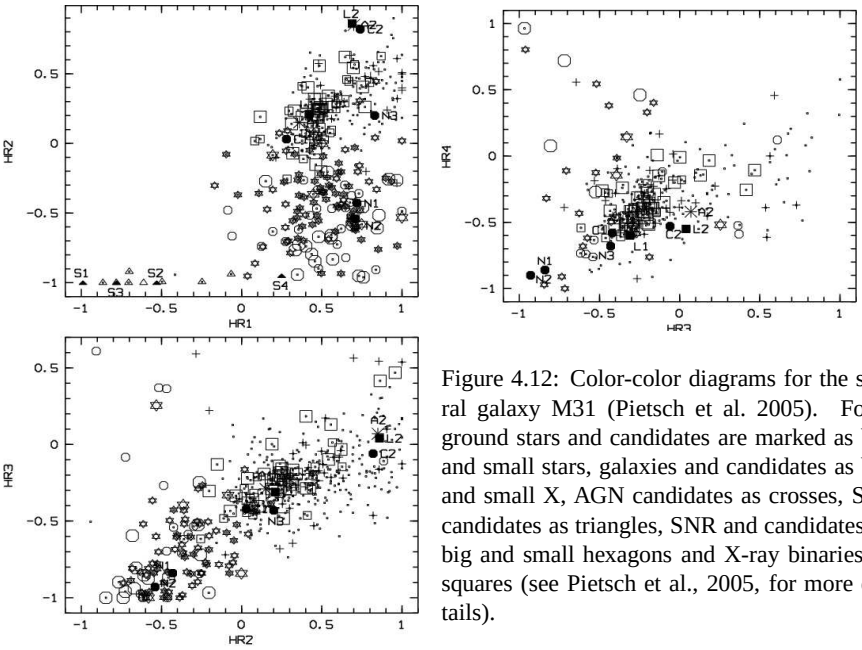

Figure 4.12: Color-color diagrams for the spiral galaxy M31 (Pietsch et al. 2005). Foreground stars and candidates are marked as big and small stars, galaxies and candidates as big and small X, AGN candidates as crosses, SSS candidates as triangles, SNR and candidates as big and small hexagons and X-ray binaries as squares (see Pietsch et al., 2005, for more details).

not able to distinguish X-ray binaries from background AGNs, as they both have hard spectra and association with radio sources. Due to spectral similarities, our criteria, as the ones from the other authors, are not able to distinguish black hole HMXBs from black hole LMXBs (optical data are then necessary). Finally, counterparts from SIMBAD catalogue are required to be able to distinguish between non thermal SNRs and LMXBs.

4.5 The luminosity function of NGC 300

Fig. 4.15 (solid line) shows the $\log N$–$\log S$ diagram for all detected sources that are inside the optical disk of NGC 300 and having more than 20 net counts, expressed as a function of their X-ray luminosity and flux. The 4 brightest sources (including the SSS) have been excluded from the sample as they strongly influence the curve shape. Note that I do not make an attempt to correct for possible background AGN, which could appear as sources which are strongly absorbed by the gas within NGC 300. The *soft sources*, with $\mathrm{HR_{soft}} \leq -0.35$, are shown with a dotted line and the *hard sources*, with $\mathrm{HR_{soft}} > -0.35$, are shown with a dashed line. As we saw from the

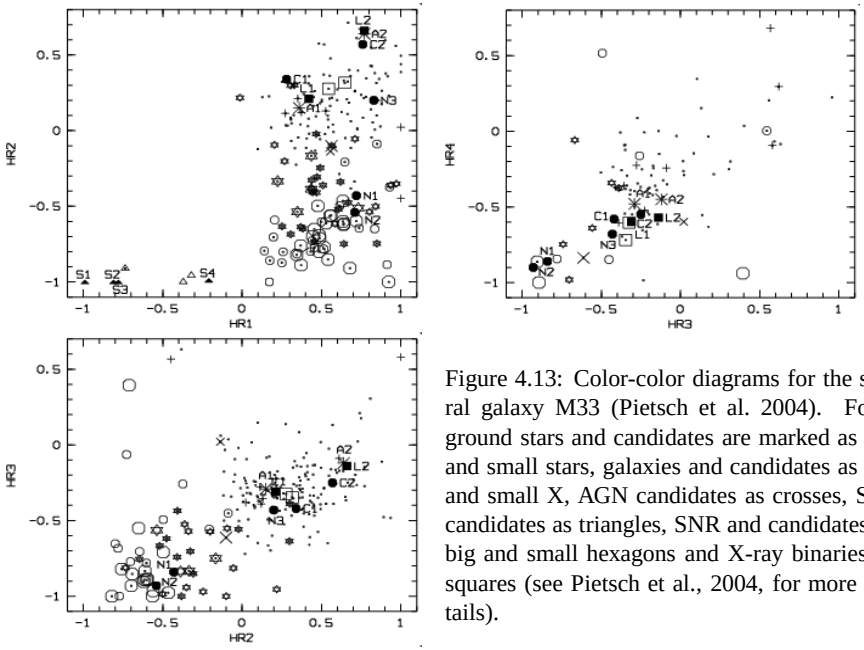

Figure 4.13: Color-color diagrams for the spiral galaxy M33 (Pietsch et al. 2004). Foreground stars and candidates are marked as big and small stars, galaxies and candidates as big and small X, AGN candidates as crosses, SSS candidates as triangles, SNR and candidates as big and small hexagons and X-ray binaries as squares (see Pietsch et al., 2004, for more details).

color-color diagram (Fig. 4.3), the soft sources are mainly composed of SNRs while the hardest ones are expected to be X-ray binaries. Comparing with galactic SNRs, LMXBs and HMXBs (see Fig. 2.3), I can conclude that, as the galactic one, my SNR curve is well represented by a power law above the completeness limit (at $F_{0.3-6} \sim 3\times10^{-15}\,\mathrm{erg\,cm^{-2}\,s^{-1}}$). Describing the luminosity function above this limit by a pure power law, $N \propto L^{-\alpha}$, I use a Maximum-Likelihood method of the form suggested by Crawford et al. (1970) and find a slope of $\alpha = 1.68 \pm 0.49$. My curve for the X-ray binaries, on the other hand, has a more complex shape and is similar to the Milky Way LMXB luminosity function. Grimm et al. (2002) described it by a modified power law which takes into account the gradual steepening of the $\log N$–$\log S$ relation towards higher fluxes. This indicates that LMXBs in NGC 300 is the dominant class of objects. I attempted to fit to that curve 2 power law functions, one from $F_{0.3-6} \sim 3\times10^{-15}\,\mathrm{erg\,cm^{-2}\,s^{-1}}$ to $F_{0.3-6} \sim 7.5\times10^{-15}\,\mathrm{erg\,cm^{-2}\,s^{-1}}$ and the other from $F_{0.3-6} \sim 7.5\times10^{-15}\,\mathrm{erg\,cm^{-2}\,s^{-1}}$ to the end. Due to the low number of sources in the sample, I was not able to fit a power law for the first part but only for the second one, and found a slope of $\alpha = 3.51 \pm 1.06$.

Fig. 4.16 shows the $\log N$–$\log S$ diagram for sources inside (solid line) and outside (dotted line) the optical disk. Sources outside the optical disk are expected to

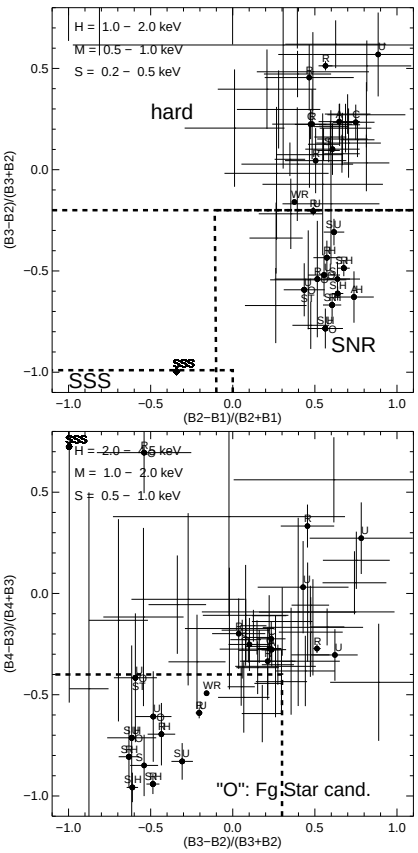

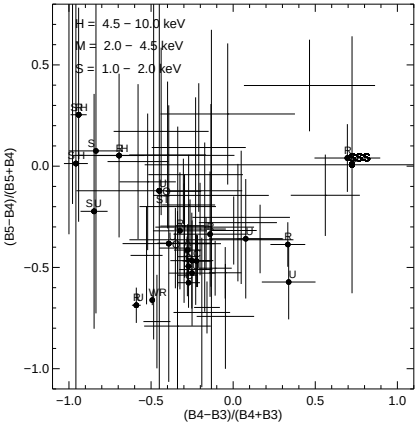

Figure 4.14: Color-color diagrams for NGC 300 according to the hardness ratio and energy band definition of Pietsch et al. (2004, 2005).

be mainly background AGNs, with some foreground stars and probably also some NGC 300 X-ray binaries, as the X-ray confinement of galaxies can be larger than the optical one. The latter can be responsible of the curved shape of the line at luminosities above $L_{\rm X} \sim 1 \times 10^{37}\,{\rm erg\,s^{-1}}$. Describing the luminosity function above the completeness limit by a pure power law, I find a slope of $\alpha = 1.15 \pm 0.17$ and $\alpha = 0.91 \pm 0.16$, for sources inside and outside the optical disk, respectively. The slope of the NGC 300 luminosity function is similar to the slope of the disk population in several other nearby spirals such as M 31 ($\alpha = 0.9 \pm 0.1$; Williams et al. 2004) or NGC 1332 (Humphrey & Buote 2004), and also in agreement with the mean slope for nearby spiral galaxies: $\alpha = 0.79 \pm 0.24$ (Colbert et al. 2004), see Fig. 4.17, and $\alpha = 1.04 \pm 0.1$ (Kilgard et al. 2005), see Fig. 4.18. I also overlayed on the diagram (with crosses), the luminosity function for a sample of 247 AGNs following Ueda

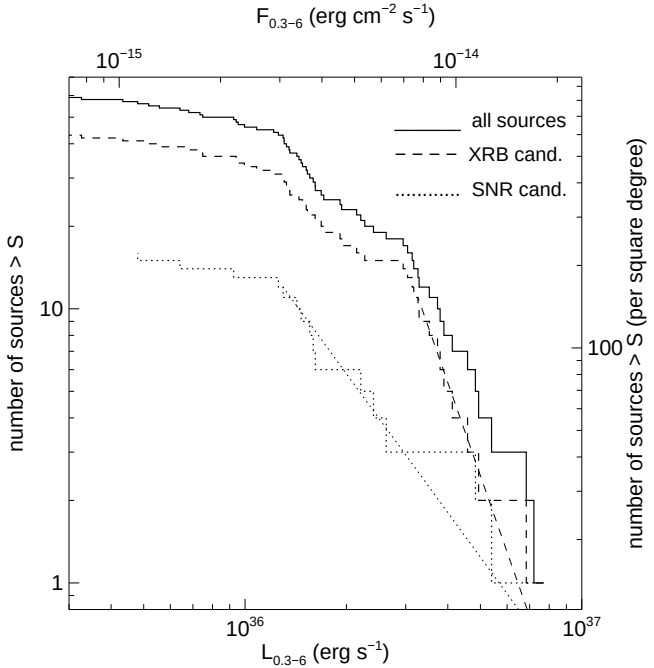

Figure 4.15: $\log N$–$\log S$ diagram of all sources (excluding the 4 brightest) with more than 20 net counts inside the optical disk (solid line), of soft sources with $\mathrm{HR_{soft}} \leq -0.35$ (dotted line), and for sources harder than that (dashed line).

et al. (2003), as already shown in Fig. 4.5 (uppermost black line). Note that energy bands used by Ueda et al. (2003) (2–10 keV) are different from mine (0.3–6.0 keV).

4.6 The central diffuse emission region

I extracted the spectrum of the central diffuse emission region after removing all point sources located in that region. The extracted regions are defined by the `region` task, such that the brightness contour level of the source PSF functions are equal to half of their background flux. I defined the diffuse emission region with a circle of radius 386.″5, centered on $\alpha_{\mathrm{J2000.0}} = 00^{\mathrm{h}}54^{\mathrm{m}}52.^{\mathrm{s}}4$, $\delta_{\mathrm{J2000.0}} = -37^{\circ}41'07.''3$. The background was taken from an annulus with the same center, an inner radius of 386.″5 and outer radius of 711.″1 (see Fig. 4.20).

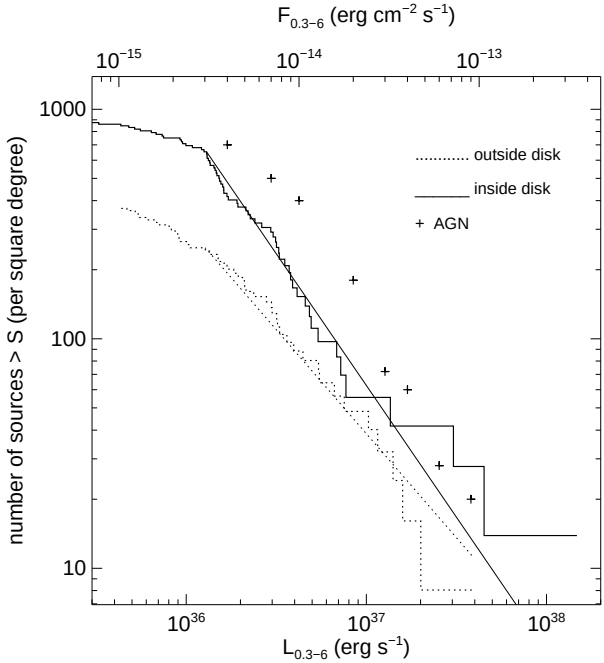

Figure 4.16: $\log N$–$\log S$ diagram of all sources with more than 20 net counts inside the optical disk (solid line) and outside the optical disk (dotted line). The AGN curve from Ueda et al. (2003) is shown with crosses.

Data from all instruments and both revolutions were used to extract the spectrum. Because the spectrum of the diffuse emission region is very soft, I consider only the 0.3–1.3 keV energy band. The Al and Si fluorescence lines present in the MOS background (in the 1.3–1.9 keV band), which cannot be removed properly, are beyond the region of interest. The spectrum can be described ($\chi^2/\mathrm{dof} = 142.5/94$) by thermal emission from a collisionally ionized plasma, as described by XSPEC's APEC (Astrophysical Plasma Emission Code) model with a temperature of $kT = 0.2 \pm 0.01$ keV plus a thermal component with a temperature of $kT = 0.8 \pm 0.1$ keV (see Fig. 4.19). The APEC code uses the atomic data from the companion APED (Astrophysical Plasma Emission Database) to calculate the spectral model from both lines and continuum emissivities for a hot, optically thin plasma in collisional ionization equilibrium (Smith et al. 2001). Using this model I found a 0.3–1.3 keV flux of $F_{0.3\text{–}1.3} = 1.8 \pm 0.1 \times 10^{-13}\,\mathrm{erg\,cm^{-2}\,s^{-1}}$. Similar results are found for the diffuse

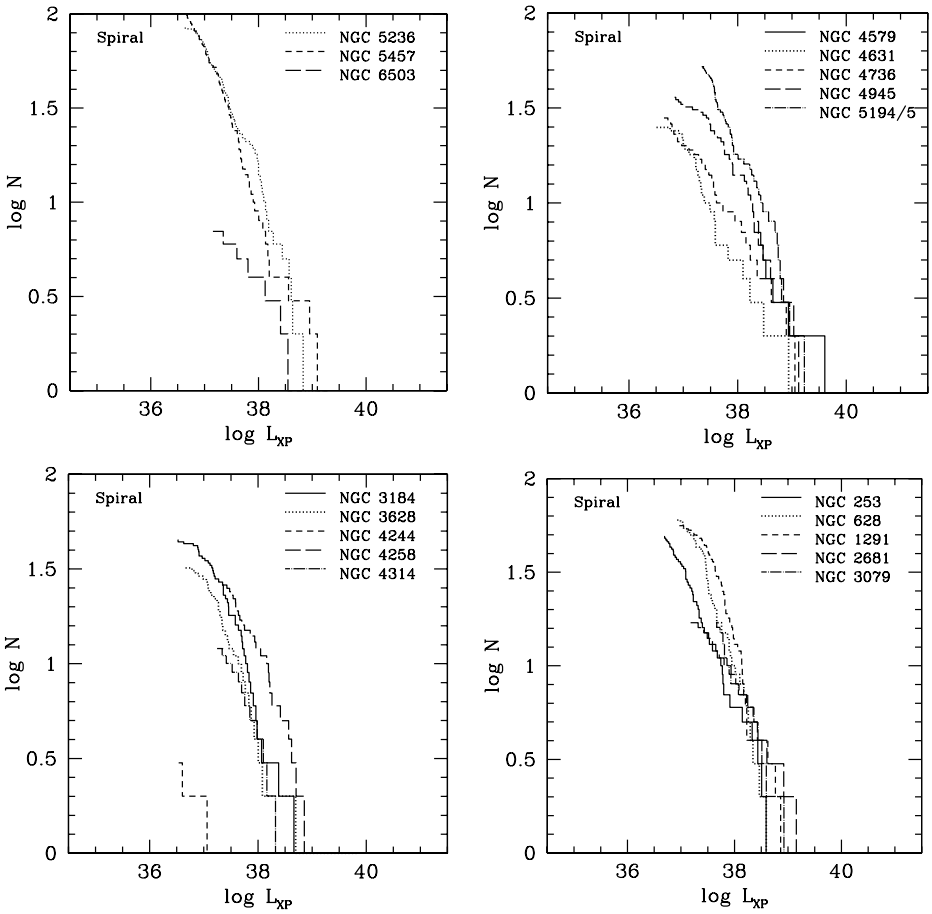

Figure 4.17: $\log N$–$\log S$ diagram for 18 spiral galaxies selected randomly from the nearby (d < 30 Mpc) NGC galaxies (Colbert et al. 2004).

region in nearly face-on spiral galaxy M101 (Kuntz et al. 2003), where the spectrum in the 0.5–2 keV band, is characterized by the sum of two thermal spectra with $kT = 0.20$ keV and $kT = 0.75$ keV.

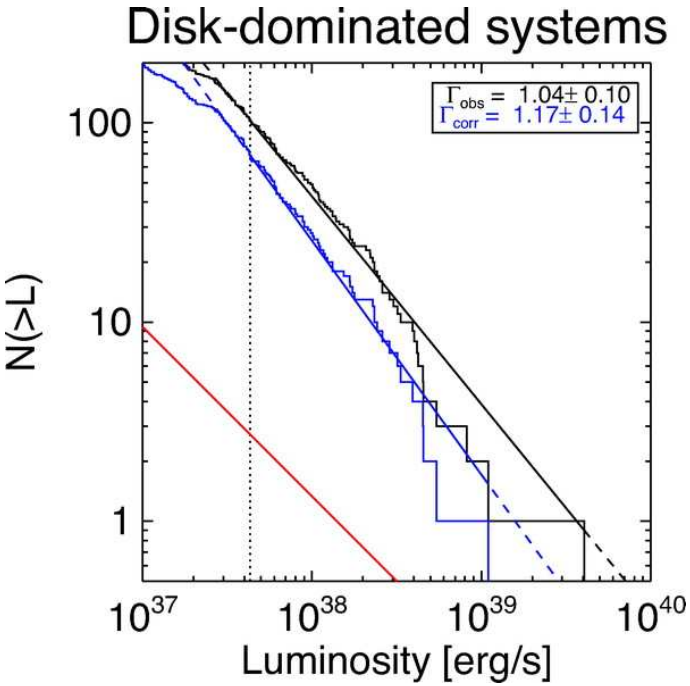

Figure 4.18: $\log N$–$\log S$ diagram for spiral galaxies M74, NGC 3184, M101, and IC 5332 (Kilgard et al. 2005). The black curve indicates the complete data plus background luminosity function and the best-fit single power law. The blue curve indicates the background-subtracted data luminosity function and best-fit single power law. The red curve indicates the ideal background luminosity function (see Kilgard et al. 2005 for more details).

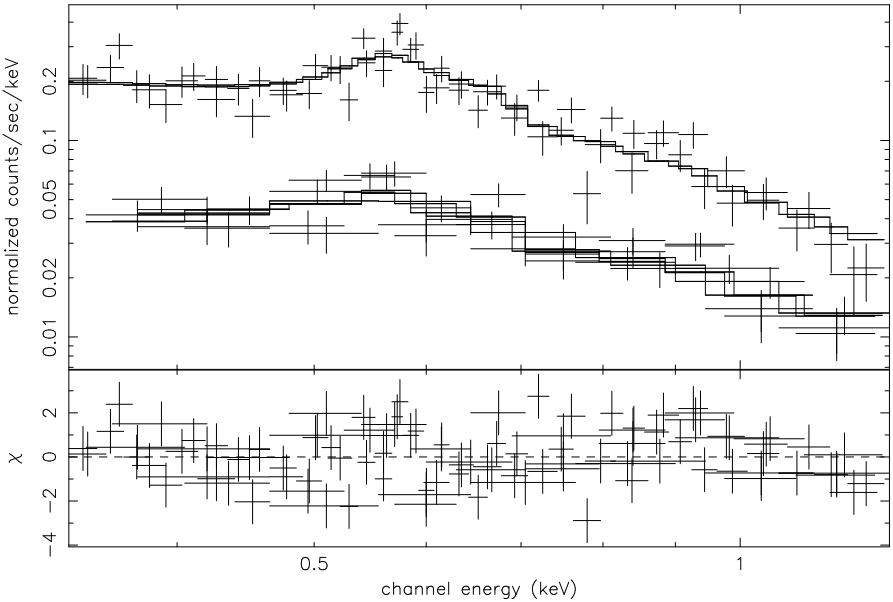

Figure 4.19: top: EPIC pn and MOS spectra of the central diffuse emission region and the best fit spectral model, consisting of the sum of an APEC model, and a bremsstrahlung component; bottom: residuals expressed in σ.

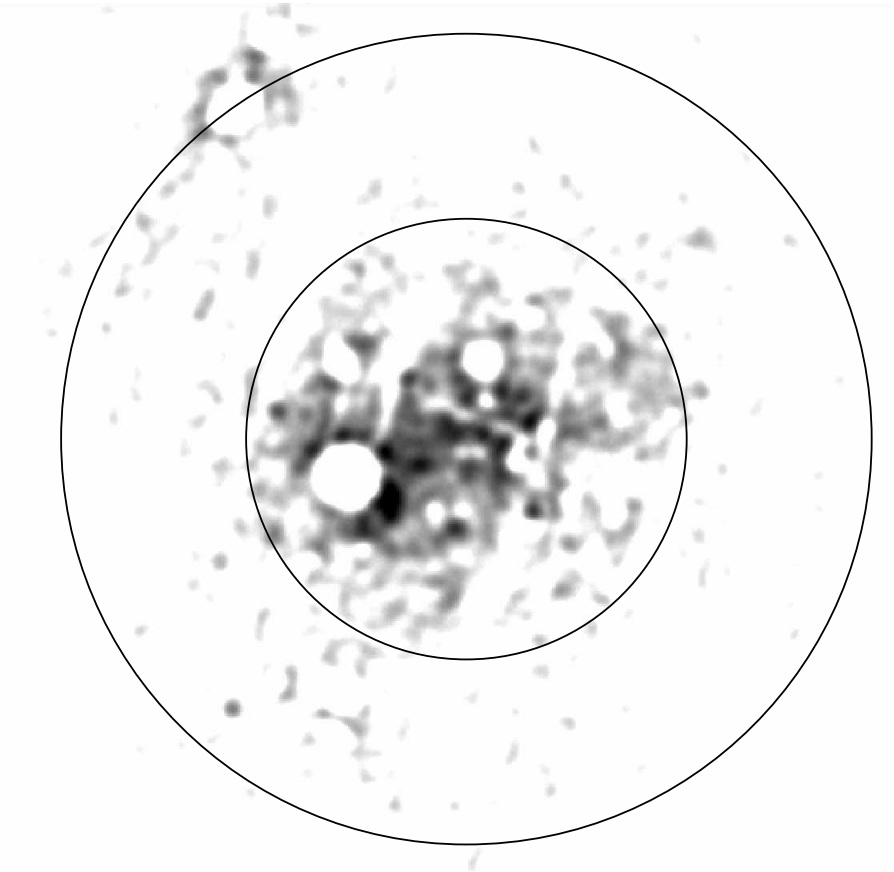

Figure 4.20: Smoothed 0.3–1.3 keV X-ray image of the central region of NGC 300 after removal of detected sources. The circle and annulus show the region for the central diffuse emission area and the associated background, respectively.

CHAPTER 5

Optical counterparts

In this Chapter, I search for the optical counterparts of the 86 sources detected inside the D_{25} disk. Fig. 5.1 shows the optical images centered on the 16 brightest X-ray sources inside the optical disk. Each image is $7\farcs4 \times 7\farcs4$ and centered on the position of the X-ray source (marked with a cross). Comparing the X-ray position with some bright optical objects (e.g., for sources 3, 7, 21, 26, 28, 34, 37 and 38), there appears to be a shift in coordinates. This offset is being corrected by the `eposcorr` task, which correlates the positions of the X-ray source catalogue with the corresponding optical sources. I then selected 21 X-ray sources within the D_{25} disk which have clear optical counterparts.

The correlation algorithm of the `eposcorr` task checks whether there are offsets in RA, DEC and roll angle, optimizing the correlation. These optimum offsets are then used to correct the input positions of the X-ray sources. This algorithm reveals a systematic shift (X-ray − optical) of $-1\farcs25 \pm 0\farcs31$ in right ascension, of $-0\farcs17 \pm 0\farcs31$ in declination, and of $-0\fdg077 \pm 0\fdg27$ for the roll angle.

These offset values are close to values found in the astrometric calibration of *XMM-Newton* by Guainazzi et al. (2004)[1], who find for RA: $-2\farcs52$ (1σ) and $-3\farcs09$ (1σ), and for DEC: $1\farcs19$ and $0\farcs41$, for MOS1 and MOS2 respectively. The final uncertainty in X-ray position results from a combination of the `edetect_chain` output and the error associated with this position offset.

After correcting the X-ray positions, I searched for all possible optical counterparts in the merged BVR optical image, only for sources which have a 1σ position error $\leq 1\farcs5$, and then calculated their fluxes in each of these three optical bands. Photometry was performed with the IDL `idlphot` photometry library available at `http://idlastro.gsfc.nasa.gov/contents.html`, which is a set of IDL procedures adapted from an early Fortran version of the DAOPHOT aperture photometry package. The principles of the algorithms can be found in Stetson (1987) and at `http://nedwww.ipac.caltech.edu/level5/Stetson/Stetson4.html`.

An explanation of the routines used for this work is given below.

[1] `http://xmm.vilspa.esa.es/external/xmm_sw_cal/sas_sci_val/index.shtml`

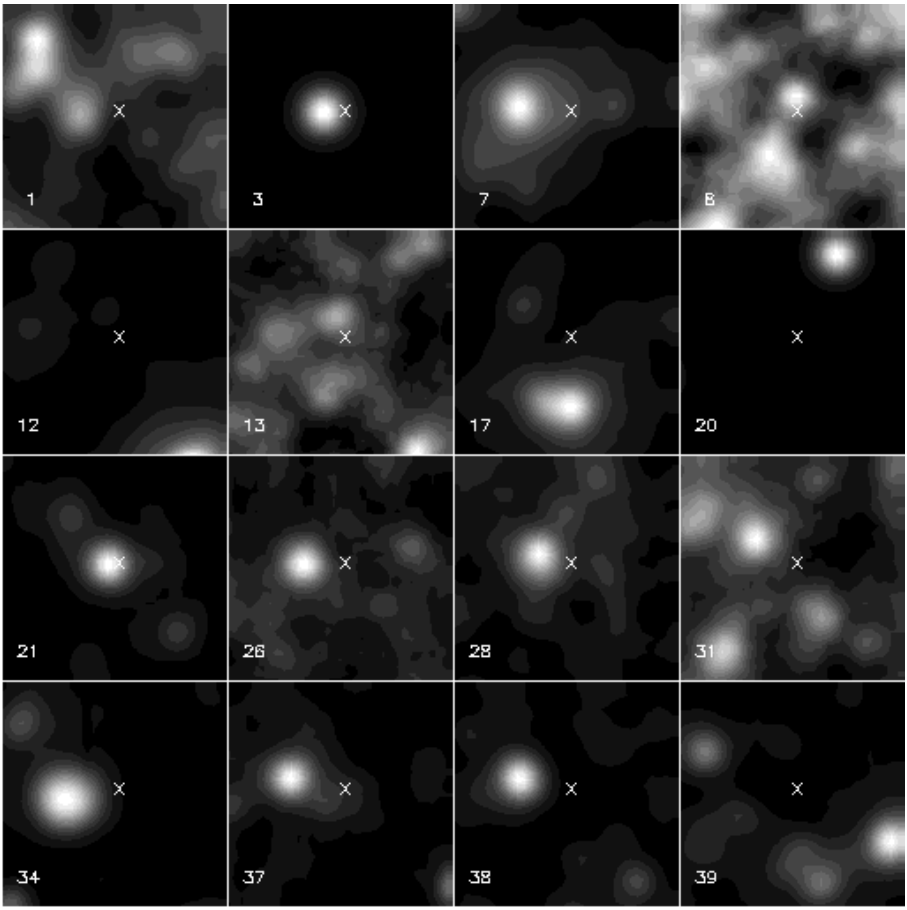

Figure 5.1: $7\farcm4 \times 7\farcm4$ optical images of the region centered on the position of the 16 brightest X-ray sources inside the D_{25} optical disk, before the offset correction. The cross marks the position of the X-ray source.

FIND: The FIND task is used to find star like objects in the frame. It produces an initial list of approximate centroid positions for all single stars that can be distinguished in the image. The star brightness must be higher than the user-defined threshold, which must be taken above the local star brightness, and the source must have approximately the correct diameter and profile for a star image in a frame. An estimate of the full-width at half-maximum (FWHM)

expected for stars in that frame must be given as input. This is easy to estimate by plotting the profile of some bright stars.

The FIND routine then assumes that the stellar profile is a circular Gaussian function with that FWHM, and fits that profile, by means of a least square procedure, to a small region around every single pixel (excluding a narrow border around the frame).

The task also gives a crude estimate of each star's apparent brightness, its sharpness (brightness in the central pixel of the peak as compared to the surrounding pixels) and roundness (second derivative of intensity with respect to the y-direction, as compared to second derivative with respect to x).

GETPSF: GETPSF is used to measure, encode, and store the two-dimensional intensity profile, the point-spread function (PSF), of a typical star in the frame. Note that this PSF is assumed to be independent of the brightness of the star and can therefore be determined from one bright, isolated star. In our case the PSF is represented as a 2-dimensional Gaussian and a lookup table of residuals.

APER: Before performing the nonlinear least-squares profile fits, I must first obtain starting values for the brightness of the star and the local brightness of the sky (an estimate of the centroid position has already been given by FIND). This is done via aperture photometry: the software takes a circular aperture around the estimated position of the star to calculate the total number of counts in that region (APER uses a polygon approximation for the intersection of a circular aperture with a square pixel and normalizes the total area of the sum of the pixels to exactly match the circular area). At the same time, it takes a circular annulus around the position of the star and builds up the histogram of brightness values found in the pixels in that annulus (see Fig 5.2).

The mean and standard deviation of the histogram are computed, and the tails of the sky histogram are excluded. The mean and standard deviation are then recomputed, and the process continues until the mean and standard deviation stop to change. The local sky brightness is defined as the estimated mode of this truncated histogram, and is then substracted from the circular star aperture. The remaining flux is a good estimate of the star brightness.

NSTAR: The last step of the procedure is to fit the model profile obtained by GETPSF to the images of the stars found by the FIND procedure. Assuming that the shape of the profile of each star is now known, the algorithm uses a nonlinear least squares procedure to shift that profile in x and y and determine the local sky background intensity and the intensity amplitude of the profile using the starting parameters derived in the previous steps. The algorithm is able to fit the PSF to each star even if the profiles of several stars overlap somewhat.

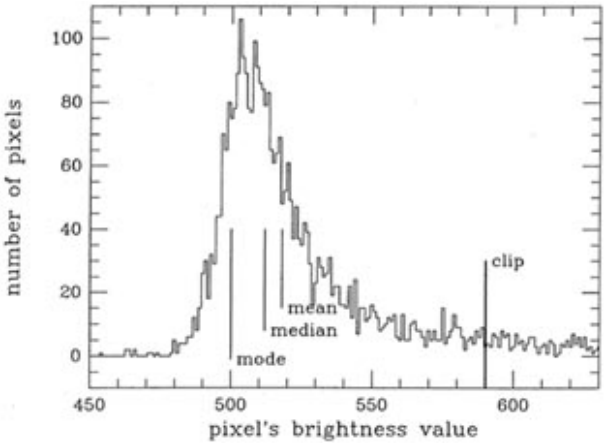

Figure 5.2: Histogram of brightness values found in the pixels in the sky annulus (http://nedwww.ipac.caltech.edu/level5/Stetson/Stetson4.html).

Brightness (B) is then converted to magnitude (M) using:

$$M = C - 2.5 \log(B) \tag{5.1}$$

where C (a constant) is called the zero-point of the image. For my optical images, these zero-points are 24.4, 24.1, 24.5 mag (ref.: Schirmer, 2005, private communication), respectively, for the red, visible and blue band. The corresponding error is difficult to be calculated because the data were taken in very inhomogeneous conditions. It has been estimated to be of the order of $\simeq 0.15$ mag (ref.: Schirmer, 2005, private communication).

To summarize, I generated an initial optical catalogue by searching for sources within the area surrounding the corrected X-ray positions (for which the radius is given by the 2σ error of the position) in the merged optical image using `idlphot`'s `find` procedure and assuming a Gaussian point spread function (PSF). This is done only for sources which have a 1σ position error $\leq 1\farcs5$. This search results in a list of several possible optical counterparts. These source positions are then improved by fitting a measured PSF (as determined from bright optical sources in the image) and the source flux in the B, V, and R bands is determined from the PSF fit after subtracting the background level. Comparing the B and V magnitudes with reference stars given by Pietrzyński et al. (2002b) shows differences of less than 0.15 mag, in agreement with my typical flux uncertainty.

Results are shown in appendix A. Fig. A.1 to Fig. A.6 show the resulting optical

counterparts in the merged optical image, for the 86 X-ray sources detected within the optical disk. Each image is centered on the corrected position of the X-ray source and is $15'' \times 15''$ wide. As further described in Sect. 5.1 below, I also compare these X-ray and optical positions with sources from SIMBAD, the USNO-A2.0 catalogue, and with radio sources from Payne et al. (2004b). I consider sources from these catalogues as possible counterparts if they have a distance less than $5''$ from the corrected X-ray positions for X-ray sources. For SNRs however, as they can extend over $5''$, I consider as counterparts, those SNRs with a distance smaller than $10''$. Finally, as X-ray sources were found with position errors up to $20''$, I choose a maximum distance of $20''$, to consider these sources as counterparts. Catalogue sources having a distance of less than $5''$ from the X-ray position are shown with a box.

5.1 Summary tables

Table 5.1 summarizes all informations collected from the 86 X-ray sources detected inside the D_{25} disk of NGC 300. The first column gives the source ID. The second and third columns give the equatorial sky coordinates of the X-ray sources from the SAS `edetect_chain` task corrected by the `eposcorr` task. The combined positional error (in arcsec) from `edetect_chain` and `eposcorr` is given in column 4. Column 5 lists the detection likelihood and columns 6 and 7 give net counts and count rates (in counts s^{-1}), respectively, and their corresponding uncertainties. Columns 8 and 9 list the softer and harder hardness ratios defined by Eq. (4.3) and their errors. Column 10 and 11 give the 0.3–6.0 keV flux and luminosity (assuming a distance of 1.88 Mpc), expressed in erg cm^{-2} s^{-1} and erg s^{-1}, respectively. Column 12 indicates if the source is variable from one observation with respect to the other, according to the criteria developed in Sect. 4.3.

Table 5.2 summarizes all possible optical counterparts found from the corrected X-ray positions within the 2σ X-ray position error area and only for sources which have a 1σ position error $\leq 1\farcs5$. Column 1 gives the X-ray source ID and the number in brackets designates a label number when several optical counterparts are found within the X-ray position error area. Column 2 and 3 give the equatorial sky coordinates of optical counterparts found by `idlphot`'s `find` procedure. Columns 4, 5, and 6 give the magnitudes for the optical counterparts, in the B, V, and R band respectively, with uncertainties of $\sim$0.15 mag. Column 7 give the logarithm of the X-ray to optical flux ratio, as defined in Section 4.4. Column 8 gives the name and, when available, the reference (within brackets) for possible radio and optical counterpart sources from the USNO-A2.0 catalogue, the radio catalogue of Payne et al. (2004b,PFP2004), and the SIMBAD catalogue which includes the *ROSAT* sources and the following catalogues: Schild et al. (2003b,SCA2003), Read & Pietsch (2001,RP2001),

Pietrzyński et al. (2001b,PGF2001), Pannuti et al. (2000b,PDL2000), Blair & Long (1997b,BL97), Soffner et al. (1996b,SMJ96), Iovino et al. (1996,ICS96), Deharveng et al. (1988b,DCL88), Humphreys & Graham (1986,HG86), Graham (1984,G84).

According to the catalogues, 14 of the X-ray sources detected inside the optical disk have already been observed in X-rays (labelled 'X'), there are 9 SNRs or suspected ones (labelled 'SNR?'), 11 radio sources (labelled 'radio'), from which three are associated with SNRs and 8 are possible AGNs. Other sources match with associations of stars (labelled 'Assoc*'), H II (ionized) regions (labelled 'H II'), with regions close to Cepheid variable stars (labelled 'Cepheid'), or with stars (labelled 'Star'). Many sources also have an USNO-A2.0 optical counterpart (labelled with a number).

As already discussed in Sect. 4.2, the brightest source (#1), which has a luminosity of $3.41 \times 10^{38}\,\mathrm{erg\,s^{-1}}$, has been identified by (source P42) Read & Pietsch (2001) as a possible accreting binary. This source has been found to have a Wolf Rayet star as optical counterpart (labelled 'WR*'). I confirm that this source has a luminosity higher than the Eddington limit for a $1.4\,\mathrm{M_\odot}$ compact object, which may suggest the presence of a black hole X-ray binary. Source number 8 has already been identified by Read & Pietsch (2001) and Kong & Di Stefano (2003b) as a luminous supersoft X-ray source and has no optical counterpart.

Table 5.1: Summary table of the X-ray properties (see text for details.)

ID (1)	$\alpha_{J2000.0}$ (2)	$\delta_{J2000.0}$ (3)	Pos. Err. ($''$) (4)	Lik. (5)	Counts (6)	Ct. rate (7)	Hard HR (8)	Soft HR (9)	$F_{0.3-6}$ (cgs) (10)	$L_{0.3-6}$ (cgs) (11)	Var. (12)
1	00 : 55 : 10.00	−37 : 42 : 12.0	0.45	5.45×10^{4}	$(1.53 \pm 0.01) \times 10^{4}$	$(7.44 \pm 0.06) \times 10^{-2}$	-0.18 ± 0.01	-0.29 ± 0.01	$3.48^{+0.03}_{-0.12} \times 10^{-13}$	1.47×10^{38}	V
3	00 : 55 : 10.86	−37 : 48 : 34.4	0.47	8.30×10^{3}	$(3.16 \pm 0.06) \times 10^{3}$	$(1.61 \pm 0.03) \times 10^{-2}$	-0.21 ± 0.01	-0.30 ± 0.02	$7.15^{+0.14}_{-0.71} \times 10^{-14}$	3.02×10^{37}	
7	00 : 54 : 50.33	−37 : 38 : 49.5	0.47	7.43×10^{3}	$(2.94 \pm 0.06) \times 10^{3}$	$(1.54 \pm 0.03) \times 10^{-2}$	-0.11 ± 0.02	0.28 ± 0.02	$1.07^{+0.04}_{-0.04} \times 10^{-13}$	4.53×10^{37}	V
8	00 : 55 : 10.91	−37 : 38 : 54.3	0.46	3.85×10^{3}	$(1.72 \pm 0.04) \times 10^{3}$	$(8.97 \pm 0.23) \times 10^{-3}$	0.00 ± 0.01	-1.00 ± 0.04	$2.83^{+0.44}_{-2.36} \times 10^{-14}$	1.20×10^{37}	
12	00 : 54 : 40.66	−37 : 40 : 48.9	0.58	1.20×10^{3}	$(6.63 \pm 0.28) \times 10^{2}$	$(3.18 \pm 0.13) \times 10^{-3}$	-0.21 ± 0.02	-0.54 ± 0.05	$1.17^{+0.06}_{-0.10} \times 10^{-14}$	4.93×10^{36}	
13	00 : 55 : 27.50	−37 : 36 : 53.5	0.56	9.50×10^{2}	$(5.38 \pm 0.27) \times 10^{2}$	$(2.73 \pm 0.14) \times 10^{-3}$	-0.11 ± 0.04	0.11 ± 0.04	$1.73^{+0.21}_{-0.12} \times 10^{-14}$	7.31×10^{36}	
17	00 : 54 : 45.22	−37 : 41 : 46.7	0.53	1.45×10^{3}	$(7.79 \pm 0.32) \times 10^{2}$	$(4.11 \pm 0.17) \times 10^{-3}$	-0.16 ± 0.02	-0.66 ± 0.05	$1.62^{+0.07}_{-0.35} \times 10^{-14}$	6.86×10^{36}	
20	00 : 55 : 20.47	−37 : 48 : 10.2	0.69	3.75×10^{2}	$(3.04 \pm 0.20) \times 10^{2}$	$(1.49 \pm 0.10) \times 10^{-3}$	-0.25 ± 0.04	-0.38 ± 0.07	$5.69^{+0.89}_{-0.84} \times 10^{-15}$	2.41×10^{36}	
21	00 : 54 : 33.96	−37 : 44 : 43.2	0.58	9.17×10^{2}	$(5.65 \pm 0.27) \times 10^{2}$	$(2.93 \pm 0.14) \times 10^{-3}$	-0.09 ± 0.04	-0.01 ± 0.04	$1.80^{+0.16}_{-0.15} \times 10^{-14}$	7.59×10^{36}	
26	00 : 55 : 26.23	−37 : 38 : 38.2	0.69	4.01×10^{2}	$(3.01 \pm 0.20) \times 10^{2}$	$(1.60 \pm 0.10) \times 10^{-3}$	-0.06 ± 0.05	0.04 ± 0.05	$1.03^{+0.15}_{-0.10} \times 10^{-14}$	4.35×10^{36}	
28	00 : 54 : 42.56	−37 : 43 : 43.2	0.61	6.38×10^{2}	$(3.98 \pm 0.24) \times 10^{2}$	$(2.01 \pm 0.12) \times 10^{-3}$	-0.12 ± 0.05	0.06 ± 0.05	$1.26^{+0.11}_{-0.16} \times 10^{-14}$	5.33×10^{36}	
31	00 : 54 : 30.57	−37 : 43 : 15.9	0.65	5.11×10^{2}	$(3.26 \pm 0.21) \times 10^{2}$	$(1.69 \pm 0.11) \times 10^{-3}$	-0.06 ± 0.05	0.00 ± 0.05	$1.08^{+0.16}_{-0.13} \times 10^{-14}$	4.55×10^{36}	
34	00 : 55 : 15.39	−37 : 44 : 38.9	0.70	3.78×10^{2}	$(2.30 \pm 0.17) \times 10^{2}$	$(2.04 \pm 0.15) \times 10^{-3}$	-0.14 ± 0.04	-0.69 ± 0.09	$7.34^{+1.70}_{-0.95} \times 10^{-15}$	3.11×10^{36}	
37	00 : 55 : 17.52	−37 : 44 : 55.8	0.66	3.82×10^{2}	$(2.65 \pm 0.19) \times 10^{2}$	$(1.37 \pm 0.10) \times 10^{-3}$	-0.27 ± 0.06	0.09 ± 0.06	$7.34^{+1.05}_{-1.15} \times 10^{-15}$	3.10×10^{36}	
38	00 : 54 : 42.59	−37 : 37 : 32.7	0.69	3.77×10^{2}	$(2.75 \pm 0.20) \times 10^{2}$	$(1.38 \pm 0.10) \times 10^{-3}$	-0.20 ± 0.05	-0.11 ± 0.06	$6.93^{+1.11}_{-0.61} \times 10^{-15}$	2.93×10^{36}	
39	00 : 54 : 49.55	−37 : 40 : 00.7	0.68	3.28×10^{2}	$(2.85 \pm 0.20) \times 10^{2}$	$(1.41 \pm 0.10) \times 10^{-3}$	-0.09 ± 0.06	0.11 ± 0.06	$9.20^{+1.41}_{-1.06} \times 10^{-15}$	3.89×10^{36}	
40	00 : 54 : 13.89	−37 : 37 : 10.8	0.76	2.17×10^{2}	$(1.97 \pm 0.17) \times 10^{2}$	$(1.00 \pm 0.09) \times 10^{-3}$	-0.13 ± 0.07	0.14 ± 0.07	$6.36^{+1.05}_{-0.90} \times 10^{-15}$	2.69×10^{36}	
41	00 : 54 : 48.07	−37 : 46 : 57.4	0.79	3.27×10^{2}	$(2.41 \pm 0.19) \times 10^{2}$	$(1.21 \pm 0.10) \times 10^{-3}$	-0.06 ± 0.06	-0.01 ± 0.06	$7.69^{+1.26}_{-1.05} \times 10^{-15}$	3.25×10^{36}	
42	00 : 54 : 48.11	−37 : 45 : 40.0	0.69	3.71×10^{2}	$(2.62 \pm 0.19) \times 10^{2}$	$(1.29 \pm 0.09) \times 10^{-3}$	-0.07 ± 0.06	0.12 ± 0.06	$8.72^{+1.07}_{-1.14} \times 10^{-15}$	3.69×10^{36}	
43	00 : 54 : 57.28	−37 : 43 : 11.4	0.69	3.38×10^{2}	$(2.81 \pm 0.20) \times 10^{2}$	$(1.46 \pm 0.10) \times 10^{-3}$	-0.05 ± 0.06	0.06 ± 0.06	$9.79^{+1.08}_{-1.24} \times 10^{-15}$	4.14×10^{36}	
46	00 : 55 : 42.91	−37 : 44 : 34.8	0.96	1.33×10^{2}	$(1.16 \pm 0.14) \times 10^{2}$	$(7.61 \pm 0.84) \times 10^{-4}$	-0.13 ± 0.07	-0.54 ± 0.12	$3.11^{+0.80}_{-0.70} \times 10^{-15}$	1.31×10^{36}	
47	00 : 54 : 50.63	−37 : 46 : 00.7	0.69	2.51×10^{2}	$(1.99 \pm 0.17) \times 10^{2}$	$(9.82 \pm 0.82) \times 10^{-4}$	0.01 ± 0.07	0.09 ± 0.07	$7.12^{+0.82}_{-1.05} \times 10^{-15}$	3.01×10^{36}	
48	00 : 54 : 19.97	−37 : 39 : 08.9	0.87	1.63×10^{2}	$(1.61 \pm 0.16) \times 10^{2}$	$(7.56 \pm 0.76) \times 10^{-4}$	-0.06 ± 0.09	0.31 ± 0.08	$5.68^{+0.98}_{-1.01} \times 10^{-15}$	2.40×10^{36}	
50	00 : 55 : 07.67	−37 : 44 : 20.1	0.76	2.13×10^{2}	$(2.01 \pm 0.17) \times 10^{2}$	$(1.03 \pm 0.09) \times 10^{-3}$	0.03 ± 0.08	0.20 ± 0.07	$7.79^{+1.27}_{-1.15} \times 10^{-15}$	3.29×10^{36}	
52	00 : 55 : 42.24	−37 : 40 : 23.7	1.13	9.98×10^{1}	$(7.09 \pm 1.09) \times 10^{1}$	$(8.04 \pm 1.20) \times 10^{-4}$	-0.04 ± 0.07	-0.90 ± 0.19	$3.66^{+0.90}_{-1.50} \times 10^{-15}$	1.55×10^{36}	

Continued

ID (1)	$\alpha_{J2000.0}$ (2)	$\delta_{J2000.0}$ (3)	Pos. Err.(″) (4)	Lik. (5)	Counts (6)	Ct. rate (7)	Hard HR (8)	Soft HR (9)	$F_{0.3-6}$ (cgs) (10)	$L_{0.3-6}$ (cgs) (11)	Var. (12)
54	00 : 54 : 41.04	−37 : 33 : 51.7	0.99	1.39×10^2	$(1.46 \pm 0.14) \times 10^2$	$(8.66 \pm 0.85) \times 10^{-4}$	0.41 ± 0.10	0.11 ± 0.06	$8.53^{+1.40}_{-1.40} \times 10^{-15}$	3.61×10^{36}	
56	00 : 54 : 50.56	−37 : 41 : 27.8	0.78	2.16×10^2	$(2.04 \pm 0.17) \times 10^2$	$(1.06 \pm 0.09) \times 10^{-3}$	-0.15 ± 0.05	-0.47 ± 0.09	$4.58^{+0.62}_{-0.95} \times 10^{-15}$	1.94×10^{36}	
57	00 : 55 : 27.24	−37 : 36 : 13.5	1.06	9.43×10^1	$(1.10 \pm 0.13) \times 10^2$	$(6.83 \pm 0.81) \times 10^{-4}$	-0.16 ± 0.10	0.06 ± 0.10	$4.00^{+0.92}_{-0.77} \times 10^{-15}$	1.69×10^{36}	
60	00 : 54 : 44.38	−37 : 41 : 14.7	0.78	1.65×10^2	$(1.74 \pm 0.16) \times 10^2$	$(9.10 \pm 0.83) \times 10^{-4}$	-0.16 ± 0.05	-0.58 ± 0.10	$3.49^{+0.69}_{-0.71} \times 10^{-15}$	1.48×10^{36}	
64	00 : 55 : 27.16	−37 : 45 : 16.5	0.95	1.04×10^2	$(1.02 \pm 0.13) \times 10^2$	$(6.80 \pm 0.81) \times 10^{-4}$	-0.27 ± 0.10	0.08 ± 0.10	$3.65^{+0.81}_{-1.00} \times 10^{-15}$	1.54×10^{36}	
65	00 : 54 : 51.52	−37 : 35 : 34.5	0.98	1.14×10^2	$(1.01 \pm 0.12) \times 10^2$	$(7.86 \pm 0.97) \times 10^{-4}$	-0.04 ± 0.10	0.02 ± 0.10	$5.25^{+1.03}_{-1.08} \times 10^{-15}$	2.22×10^{36}	
66	00 : 54 : 33.79	−37 : 44 : 26.1	0.94	8.00×10^1	$(2.01 \pm 0.17) \times 10^2$	$(9.95 \pm 0.87) \times 10^{-4}$	-0.01 ± 0.08	0.33 ± 0.07	$7.86^{+1.21}_{-1.28} \times 10^{-15}$	3.32×10^{36}	
67	00 : 54 : 35.93	−37 : 34 : 33.8	1.02	8.91×10^1	$(1.02 \pm 0.13) \times 10^2$	$(5.32 \pm 0.66) \times 10^{-4}$	0.01 ± 0.10	0.04 ± 0.10	$3.69^{+0.89}_{-0.80} \times 10^{-15}$	1.56×10^{36}	
69	00 : 54 : 31.67	−37 : 38 : 27.7	0.98	9.87×10^1	$(9.22 \pm 1.31) \times 10^1$	$(4.63 \pm 0.65) \times 10^{-4}$	-0.15 ± 0.11	0.11 ± 0.12	$2.88^{+0.82}_{-0.75} \times 10^{-15}$	1.22×10^{36}	
71	00 : 55 : 11.28	−37 : 46 : 37.7	0.97	1.01×10^2	$(9.27 \pm 1.24) \times 10^1$	$(5.72 \pm 0.75) \times 10^{-4}$	-0.19 ± 0.12	0.44 ± 0.12	$4.02^{+1.08}_{-0.97} \times 10^{-15}$	1.70×10^{36}	
72	00 : 54 : 37.68	−37 : 42 : 49.6	0.92	1.29×10^2	$(1.34 \pm 0.14) \times 10^2$	$(7.24 \pm 0.75) \times 10^{-4}$	-0.04 ± 0.08	-0.01 ± 0.09	$4.60^{+1.09}_{-0.73} \times 10^{-15}$	1.94×10^{36}	
73	00 : 55 : 31.08	−37 : 37 : 56.1	1.20	5.32×10^1	$(6.68 \pm 1.01) \times 10^1$	$(4.37 \pm 0.64) \times 10^{-4}$	-0.04 ± 0.12	0.10 ± 0.12	$2.95^{+0.95}_{-0.68} \times 10^{-15}$	1.25×10^{36}	
74	00 : 54 : 47.71	−37 : 32 : 57.5	1.45	4.19×10^1	$(4.24 \pm 0.87) \times 10^1$	$(3.25 \pm 0.64) \times 10^{-4}$	0.03 ± 0.16	-0.06 ± 0.16	$2.19^{+0.80}_{-0.70} \times 10^{-15}$	9.24×10^{35}	
79	00 : 54 : 22.13	−37 : 40 : 25.0	1.05	9.44×10^1	$(5.43 \pm 0.99) \times 10^1$	$(4.15 \pm 0.69) \times 10^{-4}$	-0.14 ± 0.10	-0.66 ± 0.19	$1.60^{+0.76}_{-0.48} \times 10^{-15}$	6.76×10^{35}	
84	00 : 54 : 25.03	−37 : 43 : 56.3	1.04	8.13×10^1	$(9.11 \pm 1.23) \times 10^1$	$(5.41 \pm 0.74) \times 10^{-4}$	0.32 ± 0.14	0.31 ± 0.10	$5.35^{+0.99}_{-1.13} \times 10^{-15}$	2.26×10^{36}	
87	00 : 54 : 12.03	−37 : 39 : 51.7	1.09	6.42×10^1	$(8.52 \pm 1.14) \times 10^1$	$(5.00 \pm 0.68) \times 10^{-4}$	-0.12 ± 0.12	0.19 ± 0.11	$3.30^{+0.86}_{-0.79} \times 10^{-15}$	1.40×10^{36}	
88	00 : 54 : 22.44	−37 : 43 : 13.3	1.02	9.19×10^1	$(7.28 \pm 1.09) \times 10^1$	$(8.67 \pm 1.23) \times 10^{-4}$	-0.08 ± 0.08	-0.67 ± 0.16	$3.71^{+1.45}_{-0.77} \times 10^{-15}$	1.57×10^{36}	
90	00 : 54 : 53.28	−37 : 41 : 27.0	0.95	8.94×10^1	$(9.37 \pm 1.27) \times 10^1$	$(5.97 \pm 0.81) \times 10^{-4}$	-0.13 ± 0.10	-0.06 ± 0.12	$3.40^{+0.99}_{-0.85} \times 10^{-15}$	1.44×10^{36}	
91	00 : 54 : 25.32	−37 : 44 : 39.5	1.11	8.24×10^1	$(8.58 \pm 1.20) \times 10^1$	$(5.66 \pm 0.74) \times 10^{-4}$	-0.02 ± 0.10	-0.07 ± 0.11	$3.67^{+0.90}_{-0.87} \times 10^{-15}$	1.55×10^{36}	
92	00 : 54 : 21.04	−37 : 42 : 40.8	1.12	6.19×10^1	$(8.97 \pm 1.16) \times 10^1$	$(4.54 \pm 0.60) \times 10^{-4}$	0.14 ± 0.12	0.32 ± 0.10	$4.00^{+0.85}_{-0.86} \times 10^{-15}$	1.69×10^{36}	
94	00 : 55 : 12.23	−37 : 38 : 23.8	1.10	5.98×10^1	$(7.99 \pm 1.16) \times 10^1$	$(5.76 \pm 0.89) \times 10^{-4}$	-0.11 ± 0.10	-0.34 ± 0.15	$2.79^{+0.91}_{-0.68} \times 10^{-15}$	1.18×10^{36}	
99	00 : 54 : 47.35	−37 : 48 : 26.9	1.13	5.72×10^1	$(5.39 \pm 0.97) \times 10^1$	$(4.55 \pm 0.78) \times 10^{-4}$	0.02 ± 0.15	0.16 ± 0.13	$3.43^{+1.01}_{-0.95} \times 10^{-15}$	1.45×10^{36}	
100	00 : 54 : 12.47	−37 : 43 : 20.7	1.23	4.86×10^1	$(5.79 \pm 1.00) \times 10^1$	$(3.81 \pm 0.63) \times 10^{-4}$	-0.27 ± 0.14	0.19 ± 0.14	$2.11^{+0.82}_{-0.65} \times 10^{-15}$	8.93×10^{35}	
102	00 : 54 : 28.55	−37 : 41 : 29.7	1.04	6.83×10^1	$(1.09 \pm 0.39) \times 10^1$	$(3.78 \pm 1.31) \times 10^{-4}$					
103	00 : 55 : 03.66	−37 : 37 : 40.1	1.00	6.14×10^1	$(8.42 \pm 1.11) \times 10^1$	$(4.16 \pm 0.58) \times 10^{-4}$	0.02 ± 0.10	-0.41 ± 0.13	$2.34^{+0.66}_{-0.59} \times 10^{-15}$	9.88×10^{35}	
107	00 : 54 : 59.02	−37 : 47 : 51.0	1.42	4.69×10^1	$(5.35 \pm 0.96) \times 10^1$	$(4.02 \pm 0.72) \times 10^{-4}$	0.34 ± 0.17	0.24 ± 0.13	$3.97^{+1.08}_{-1.07} \times 10^{-15}$	1.68×10^{36}	

Continued

ID (1)	$\alpha_{J2000.0}$ (2)	$\delta_{J2000.0}$ (3)	Pos. Err.(″) (4)	Lik. (5)	Counts (6)	Ct. rate (7)	Hard HR (8)	Soft HR (9)	$F_{0.3-6}$ (cgs) (10)	$L_{0.3-6}$ (cgs) (11)	Var. (12)
112	00 : 54 : 15.91	−37 : 45 : 07.0	1.42	4.45×10^{1}	$(4.77 \pm 0.89) \times 10^{1}$	$(3.59 \pm 0.69) \times 10^{-4}$	-0.03 ± 0.10	-0.72 ± 0.22	$1.77^{+0.46}_{-0.85} \times 10^{-15}$	7.48×10^{35}	
117	00 : 55 : 13.85	−37 : 47 : 57.8	1.71	2.49×10^{1}	$(3.39 \pm 0.77) \times 10^{1}$	$(3.24 \pm 0.75) \times 10^{-4}$	-0.02 ± 0.19	0.18 ± 0.19			
120	00 : 54 : 53.26	−37 : 43 : 10.8	1.07	5.21×10^{1}	$(7.38 \pm 1.08) \times 10^{1}$	$(4.12 \pm 0.63) \times 10^{-4}$	0.58 ± 0.16	-0.21 ± 0.10	$3.52^{+1.82}_{-0.87} \times 10^{-15}$	1.49×10^{36}	
122	00 : 55 : 29.75	−37 : 37 : 27.4	1.65	1.80×10^{1}	$(7.28 \pm 3.53) \times 10^{0}$	$(1.16 \pm 0.52) \times 10^{-4}$					
123	00 : 55 : 06.00	−37 : 41 : 18.1	1.62	2.37×10^{1}	$(5.79 \pm 3.03) \times 10^{0}$	$(1.67 \pm 0.87) \times 10^{-4}$					
125	00 : 55 : 34.06	−37 : 46 : 35.1	1.66	1.81×10^{1}	$(2.61 \pm 0.65) \times 10^{1}$	$(2.36 \pm 0.65) \times 10^{-4}$	-0.16 ± 0.24	0.30 ± 0.24	$1.62^{+0.93}_{-0.74} \times 10^{-15}$	6.84×10^{35}	
126	00 : 54 : 53.47	−37 : 40 : 28.3	1.42	3.10×10^{1}	$(3.65 \pm 0.80) \times 10^{1}$	$(1.99 \pm 0.45) \times 10^{-4}$	0.02 ± 0.14	-0.52 ± 0.23	$1.06^{+0.45}_{-0.42} \times 10^{-15}$	4.48×10^{35}	
128	00 : 55 : 23.99	−37 : 45 : 24.1	1.51	2.41×10^{1}	$(3.23 \pm 0.74) \times 10^{1}$	$(2.52 \pm 0.57) \times 10^{-4}$	0.27 ± 0.21	0.12 ± 0.16	$2.24^{+0.94}_{-0.77} \times 10^{-15}$	9.46×10^{35}	
132	00 : 54 : 30.56	−37 : 40 : 05.4	1.39	3.09×10^{1}	$(3.68 \pm 0.80) \times 10^{1}$	$(3.29 \pm 0.77) \times 10^{-4}$	0.66 ± 0.26	0.07 ± 0.14	$3.71^{+0.86}_{-1.28} \times 10^{-15}$	1.57×10^{36}	
134	00 : 55 : 14.88	−37 : 48 : 51.2	1.87	1.25×10^{1}	$(1.33 \pm 0.51) \times 10^{1}$	$(2.05 \pm 0.75) \times 10^{-4}$					
135	00 : 54 : 31.31	−37 : 45 : 26.2	1.44	2.91×10^{1}	$(6.26 \pm 3.86) \times 10^{0}$	$(1.06 \pm 0.56) \times 10^{-4}$					
136	00 : 54 : 44.82	−37 : 37 : 42.1	1.38	2.07×10^{1}	$(2.12 \pm 0.62) \times 10^{1}$	$(1.80 \pm 0.56) \times 10^{-4}$	-0.17 ± 0.25	0.20 ± 0.27	$1.15^{+0.76}_{-0.59} \times 10^{-15}$	4.85×10^{35}	
137	00 : 54 : 02.59	−37 : 39 : 31.4	1.96	1.05×10^{1}	$(1.29 \pm 0.44) \times 10^{1}$	$(1.50 \pm 0.50) \times 10^{-4}$					
139	00 : 55 : 07.51	−37 : 45 : 14.6	1.61	2.24×10^{1}	$(3.28 \pm 0.75) \times 10^{1}$	$(2.82 \pm 0.62) \times 10^{-4}$	0.22 ± 0.19	0.06 ± 0.16	$2.32^{+0.99}_{-0.73} \times 10^{-15}$	9.81×10^{35}	
140	00 : 55 : 26.77	−37 : 38 : 12.7	1.84	1.40×10^{1}	$(1.94 \pm 0.54) \times 10^{1}$	$(1.37 \pm 0.36) \times 10^{-4}$					
141	00 : 54 : 56.97	−37 : 47 : 26.7	1.49	2.47×10^{1}	$(1.47 \pm 0.50) \times 10^{1}$	$(2.92 \pm 0.95) \times 10^{-4}$					
142	00 : 54 : 33.17	−37 : 44 : 03.9	1.78	1.85×10^{1}	$(2.04 \pm 0.62) \times 10^{1}$	$(1.71 \pm 0.63) \times 10^{-4}$	0.18 ± 0.31	0.06 ± 0.28	$1.42^{+0.94}_{-0.76} \times 10^{-15}$	6.01×10^{35}	
143	00 : 55 : 31.39	−37 : 40 : 00.1	1.87	1.44×10^{1}	$(1.13 \pm 0.39) \times 10^{1}$	$(1.23 \pm 0.49) \times 10^{-4}$					
145	00 : 55 : 01.11	−37 : 34 : 39.4	2.96	1.19×10^{1}	$(6.33 \pm 3.98) \times 10^{0}$	$(1.09 \pm 0.66) \times 10^{-4}$					
146	00 : 54 : 57.44	−37 : 45 : 36.3	1.49	2.57×10^{1}	$(3.27 \pm 0.74) \times 10^{1}$	$(2.74 \pm 0.60) \times 10^{-4}$	0.05 ± 0.17	-0.05 ± 0.18	$1.92^{+0.75}_{-0.65} \times 10^{-15}$	8.12×10^{35}	
147	00 : 54 : 51.84	−37 : 47 : 08.2	1.76	1.75×10^{1}	$(3.03 \pm 0.67) \times 10^{1}$	$(1.87 \pm 0.43) \times 10^{-4}$	-0.03 ± 0.18	-0.07 ± 0.19	$1.17^{+0.54}_{-0.42} \times 10^{-15}$	4.95×10^{35}	
148	00 : 55 : 03.32	−37 : 45 : 37.6	1.79	1.74×10^{1}	$(2.43 \pm 0.68) \times 10^{1}$	$(1.51 \pm 0.42) \times 10^{-4}$	-0.01 ± 0.20	-0.32 ± 0.25	$8.75^{+4.91}_{-3.99} \times 10^{-16}$	3.70×10^{35}	
150	00 : 55 : 06.32	−37 : 37 : 53.2	1.78	1.51×10^{1}	$(1.67 \pm 0.60) \times 10^{1}$	$(1.21 \pm 0.46) \times 10^{-4}$					
151	00 : 55 : 33.79	−37 : 43 : 11.0	2.74	1.01×10^{1}							
152	00 : 55 : 05.57	−37 : 42 : 41.4	1.79	1.07×10^{1}	$(1.43 \pm 0.56) \times 10^{1}$	$(1.63 \pm 0.63) \times 10^{-4}$					
153	00 : 54 : 07.51	−37 : 41 : 15.6	2.10	1.02×10^{1}							

Continued

ID (1)	$\alpha_{J2000.0}$ (2)	$\delta_{J2000.0}$ (3)	Pos. Err.(″) (4)	Lik. (5)	Counts (6)	Ct. rate (7)	Hard HR (8)	Soft HR (9)	$F_{0.3-6}$ (cgs) (10)	$L_{0.3-6}$ (cgs) (11)	Var. (12)
155	00 : 54 : 56.89	−37 : 43 : 39.3	1.60	1.63×10^{1}	$(2.16 \pm 0.62) \times 10^{1}$	$(1.42 \pm 0.39) \times 10^{-4}$	-0.13 ± 0.22	-0.07 ± 0.23	$8.07^{+4.83}_{-3.78} \times 10^{-16}$	3.41×10^{35}	
156	00 : 54 : 29.92	−37 : 40 : 31.5	1.55	1.46×10^{1}	$(1.21 \pm 0.44) \times 10^{1}$	$(1.41 \pm 0.50) \times 10^{-4}$					
157	00 : 54 : 52.65	−37 : 46 : 00.7	2.23	1.13×10^{1}	$(3.72 \pm 2.27) \times 10^{0}$	$(1.28 \pm 0.76) \times 10^{-4}$					
158	00 : 54 : 53.33	−37 : 44 : 40.1	1.74	1.30×10^{1}	$(1.25 \pm 0.49) \times 10^{1}$	$(1.03 \pm 0.40) \times 10^{-4}$					
159	00 : 54 : 46.21	−37 : 47 : 18.6	1.68	1.45×10^{1}	$(1.14 \pm 0.46) \times 10^{1}$	$(1.12 \pm 0.43) \times 10^{-4}$					
160	00 : 54 : 56.43	−37 : 39 : 38.1	2.03	1.19×10^{1}	$(4.42 \pm 3.09) \times 10^{0}$	$(1.41 \pm 0.88) \times 10^{-4}$					
161	00 : 54 : 41.54	−37 : 43 : 03.9	2.18	1.35×10^{1}	$(3.55 \pm 3.28) \times 10^{0}$	$(1.81 \pm 1.31) \times 10^{-4}$					
162	00 : 54 : 45.95	−37 : 45 : 21.6	1.54	1.27×10^{1}	$(1.98 \pm 0.54) \times 10^{1}$	$(1.90 \pm 0.56) \times 10^{-4}$					
163	00 : 55 : 11.74	−37 : 40 : 14.8	1.69	1.08×10^{1}	$(2.71 \pm 2.30) \times 10^{0}$	$(6.26 \pm 5.30) \times 10^{-5}$					

Table 5.2: Summary table for the optical counterparts (see text for details.)

ID (1)	$\alpha_{J2000.0}$ (2)	$\delta_{J2000.0}$ (3)	mag (B) (4)	mag (V) (5)	mag (R) (6)	$\log(f_X / f_{opt})$ (7)	comments (8)
1 (1)	00 : 55 : 10.0	−37 : 42 : 12.1	22.71	22.53	22.03	1.92	X (RP2001 - P42), WR* (SCA2003 - 41)
3 (1)	00 : 55 : 10.9	−37 : 48 : 34.2	20.62	20.25	19.69	0.32	X (RP2001 - P58), radio (PFP2004), USNO: 0450-00323113
7 (1)	00 : 54 : 50.3	−37 : 38 : 49.4	21.49	20.74	19.88	0.70	X (RP2001 - P32), radio (PFP2004)
8							X (XMMU J005510.7-373855), X (RP2001 - P33)
12							SNR (BL97 - N300-S10), HII (SMJ96 - HII W22), HII (BL97 - N300-H10), radio (PFP2004)
13 (1)	00 : 55 : 27.5	−37 : 36 : 53.0	24.69	24.61	23.55	1.45	X (RP2001 - P25)
17 (1)	00 : 54 : 45.2	−37 : 41 : 45.8	22.76	22.82	21.31	0.71	X (RP2001 - P41), HII (SMJ96 - HII W7), HII (SMJ96 - HII W9), SNR (PDL2000 - SNR 6)
20							SNR (PDL2000 - SNR 15), USNO: 0450-00324001, USNO: 0450-00324043
21 (1)	00 : 54 : 33.9	−37 : 44 : 43.8	21.93	21.40	21.04	0.19	X (RP2001 - P50)
21 (2)	00 : 54 : 34.0	−37 : 44 : 42.3	23.05	22.80	22.63	0.75	
26 (1)	00 : 55 : 26.2	−37 : 38 : 37.9	23.99	23.41	22.71	0.75	X (RP2001 - P30)
28 (1)	00 : 54 : 42.6	−37 : 43 : 43.2	22.53	22.23	21.74	0.36	Cepheid (G84 - 14)
31 (1)	00 : 54 : 30.6	−37 : 43 : 15.4	23.81	23.16	22.72	0.67	
34 (1)	00 : 55 : 15.4	−37 : 44 : 39.1	21.27	21.38	19.70	−0.21	SNR (BL97 - N300-S26), HII (DCL88 - 141), radio (PFP2004)
37 (1)	00 : 55 : 17.6	−37 : 44 : 55.0	22.58	22.17	21.73	0.10	
38 (1)	00 : 54 : 42.6	−37 : 37 : 32.7	21.92	21.48	21.11	−0.20	
39							Assoc* (PGF2001 - AS 56a)
40 (1)	00 : 54 : 13.9	−37 : 37 : 11.5	21.96	21.56	21.10	−0.20	X (RP2001 - P26)
41 (1)	00 : 54 : 48.0	−37 : 46 : 56.9	24.31	24.81	23.92	1.18	X (RP2001 - P54)
42 (1)	00 : 54 : 48.1	−37 : 45 : 39.0	22.47	22.40	21.93	0.27	Cepheid (G84 - 17), X (RP2001 - P51)
43							
46 (1)	00 : 55 : 42.9	−37 : 44 : 35.6	14.52	14.45	14.54	−3.36	X (RP2001 - P48), USNO: 0450-00326180
47							
48 (1)	00 : 54 : 20.0	−37 : 39 : 8.5	24.49	24.21	23.75	0.81	
50 (1)	00 : 55 : 7.6	−37 : 44 : 18.8	23.65	23.14	22.58	0.52	
52 (1)	00 : 55 : 42.2	−37 : 40 : 24.7	24.21	23.11	21.89	0.18	X (RP2001 - P36)
52 (2)	00 : 55 : 42.4	−37 : 40 : 23.6	25.24	24.72	24.15	0.82	
52 (3)	00 : 55 : 42.3	−37 : 40 : 23.0	23.74	24.30	23.48	0.65	
54 (1)	00 : 54 : 41.1	−37 : 33 : 53.7	24.58	24.35	24.12	1.04	radio (PFP2004)
56							HII (SMJ96 - HII C27), radio (PFP2004)
57 (1)	00 : 55 : 27.3	−37 : 36 : 15.2	24.85	24.83	24.10	0.90	
57 (2)	00 : 55 : 27.3	−37 : 36 : 13.2	24.91	24.61	24.07	0.82	
57 (3)	00 : 55 : 27.2	−37 : 36 : 13.1	24.93	24.85	23.98	0.91	
60 (1)	00 : 54 : 44.4	−37 : 41 : 15.7	21.71	21.27	20.71	−0.58	SNR (PDL2000 - SNR 5), X (RP2001 - P41)

Continued

ID (1)	$\alpha_{J2000.0}$ (2)	$\delta_{J2000.0}$ (3)	mag (B) (4)	mag (V) (5)	mag (R) (6)	$\log(f_X / f_{opt})$ (7)	comments (8)
64 (1)	00 : 55 : 27.2	−37 : 45 : 16.8	24.68	24.03	23.77	0.54	
65 (1)	00 : 54 : 51.6	−37 : 35 : 36.0	23.34	23.02	22.89	0.30	
66 (1)	00 : 54 : 33.8	−37 : 44 : 25.2	25.38	24.29	23.42	0.98	X (RP2001 - P50)
67 (1)	00 : 54 : 35.9	−37 : 34 : 33.9	23.99	23.06	22.07	0.16	
69							radio (PFP2004)
71 (1)	00 : 55 : 11.2	−37 : 46 : 40.0	22.31	21.79	21.11	−0.31	USNO: 0450-00323152
72							SNR (PDL2000 - SNR 3)
73 (1)	00 : 55 : 31.2	−37 : 37 : 58.2	22.51	22.09	21.74	−0.32	X (RP2001 - P28)
73 (2)	00 : 55 : 31.3	−37 : 37 : 56.2	23.03	23.17	22.76	0.11	
73 (3)	00 : 55 : 31.1	−37 : 37 : 55.2	23.18	22.94	22.40	0.02	
74 (1)	00 : 54 : 47.8	−37 : 32 : 57.4	26.77	25.93	25.22	1.08	
79 (1)	00 : 54 : 22.2	−37 : 40 : 25.3	21.18	21.16	21.23	−0.96	HII (DCL88 - 10), SNR? (BL97 - N300-S2), USNO: 0450-00318453
79 (2)	00 : 54 : 22.1	−37 : 40 : 24.9	21.05	21.01	21.08	−1.02	
84 (1)	00 : 54 : 25.0	−37 : 43 : 58.0	26.22	26.03	24.91	1.51	
87 (1)	00 : 54 : 12.2	−37 : 39 : 52.6	24.65	24.26	23.94	0.59	
87 (2)	00 : 54 : 12.1	−37 : 39 : 50.3	25.46	26.15	25.67	1.35	
88 (1)	00 : 54 : 22.5	−37 : 43 : 12.2	20.59	19.53	18.47	−1.25	Star (HG86 - 12), USNO: 0450-00318469
90							
91 (1)	00 : 54 : 25.3	−37 : 44 : 41.1	24.56	24.29	23.58	0.65	radio (PFP2004)
91 (2)	00 : 54 : 25.4	−37 : 44 : 39.2	24.67	24.38	23.60	0.69	
92							
94 (1)	00 : 55 : 12.2	−37 : 38 : 23.8	23.53	23.11	22.62	0.06	
99 (1)	00 : 54 : 47.5	−37 : 48 : 27.7	26.32	25.68	24.74	1.18	X (RP2001 - P57)
99 (2)	00 : 54 : 47.4	−37 : 48 : 26.8	26.86	25.89	25.58	1.26	
100 (1)	00 : 54 : 12.5	−37 : 43 : 22.2	25.50	24.48	23.43	0.49	
100 (2)	00 : 54 : 12.4	−37 : 43 : 20.0	25.92	25.01	24.17	0.70	
100 (3)	00 : 54 : 12.6	−37 : 43 : 20.0	25.30	24.18	23.07	0.37	
100 (4)	00 : 54 : 12.5	−37 : 43 : 18.7	25.52	24.21	23.28	0.38	
102 (1)	00 : 54 : 28.4	−37 : 41 : 29.1	22.53	22.65	21.60		HII (BL97 - N300-H3), Assoc* (PGF2001 - AS 14)
103							
107 (1)	00 : 54 : 59.0	−37 : 47 : 52.8	23.83	22.99	21.81	0.16	USNO: 0450-00321929
107 (2)	00 : 54 : 59.0	−37 : 47 : 51.3	24.53	23.72	22.51	0.46	
107 (3)	00 : 54 : 59.0	−37 : 47 : 51.3	24.51	23.69	22.51	0.44	
107 (4)	00 : 54 : 59.2	−37 : 47 : 50.6	24.14	23.66	22.41	0.43	
107 (5)	00 : 54 : 58.9	−37 : 47 : 49.3	23.76	23.38	22.12	0.32	
112 (1)	00 : 54 : 15.7	−37 : 45 : 7.9	25.77	26.49	26.63	1.21	

Continued

ID (1)	$\alpha_{J2000.0}$ (2)	$\delta_{J2000.0}$ (3)	mag (B) (4)	mag (V) (5)	mag (R) (6)	$\log(f_X / f_{opt})$ (7)	comments (8)
112 (2)	00 : 54 : 16.1	−37 : 45 : 7.4	23.62	23.39	22.76	−0.03	
112 (3)	00 : 54 : 15.8	−37 : 45 : 4.4	25.58	25.26	24.42	0.72	
117							
120 (1)	00 : 54 : 53.2	−37 : 43 : 11.3	20.35	19.57	18.84	−1.26	radio (PFP2004)
122							
123							SNR? (BL97 - N300-S19)
125							
126							
128							USNO: 0450-00324361
132 (1)	00 : 54 : 30.7	−37 : 40 : 4.6	24.18	23.08	21.86	0.17	
134							
135 (1)	00 : 54 : 31.3	−37 : 45 : 29.0	25.58	24.68	23.67		
135 (2)	00 : 54 : 31.4	−37 : 45 : 25.7	24.84	24.02	23.31		
136 (1)	00 : 54 : 44.8	−37 : 37 : 40.8	23.49	23.22	22.83	−0.28	
137							
139							
140							X (RP2001 - P30)
141 (1)	00 : 54 : 57.2	−37 : 47 : 28.2	24.38	23.72	22.36		
141 (2)	00 : 54 : 56.9	−37 : 47 : 26.9	25.53	24.49	23.62		
142							
143							
145							USNO: 0450-00322130
146 (1)	00 : 54 : 57.5	−37 : 45 : 39.4	21.83	22.51	22.18	−0.34	
146 (2)	00 : 54 : 57.3	−37 : 45 : 36.2	0.00	24.98	23.18	0.65	
147							
148							
150							
151							SNR? (BL97 - N300-S28), HII (S66b - 80), HII (DCL88 - 159), Star (BGK2002 - A14), radio (PFP2004), USNO: 0450-00325259
152							
153							
155							
156							
157							
158							USNO: 0450-00321373
159							

Continued

ID (1)	$\alpha_{J2000.0}$ (2)	$\delta_{J2000.0}$ (3)	mag (B) (4)	mag (V) (5)	mag (R) (6)	$\log(f_X / f_{opt})$ (7)	comments (8)
160							HII (DCL88 - 99), radio (PFP2004)
161							
162							
163							

Chapter 6

The brightest sources

6.1 *Spectral fitting with XSPEC*

Spectral fitting of X-ray sources is performed using XSPEC (Arnaud 1996). Here I give a summary, see the XSPEC manual (`http://heasarc.gsfc.nasa.gov/docs/xanadu/xspec/manual/node9.html`) for details.

The output of any X-ray measurement does not consist of the actual source spectrum but rather of photons, C, that are falling during the measurement time into a specific intrumental channel, I. This measured spectrum, $C(I)$, is a convolution of the real source spectrum, $f(E)$, which is unknown, and the response of the detector $R(I, E)$ over the energy E:

$$C(I) = \int_0^\infty R(I, E) f(E) dE \tag{6.1}$$

Deriving $f(E)$ by inverting this equation is mathematically not possible, as the solution is unstable. What is done instead is to choose a theoretical model for $f(E)$, which depends on one or more parameters, and fit it to the observed spectrum.

The fitting procedure adjusts the parameters until the convolved theoretical model is close to the observed spectrum. If the fit is not good another model has to be chosen, until one finds the best spectral model, with its corresponding parameters.

The most common fit method used to determine this best-fit model, $C_\mathrm{b}(I)$, is the minimization of the chi-square statistics, χ^2, which is defined by:

$$\chi^2 = \sum \frac{(C(I) - C_\mathrm{b}(I))^2}{\sigma^2(I)} \tag{6.2}$$

where $\sigma(I)$ is the error for channel I, e.g., for Poisson noise, $\sigma(I) = \sqrt{C(I)}$.

The fit is considered good when the reduced chi-square (χ^2/ν, where ν is the number of degrees of freedom) is approximately equal to one. If the reduced χ^2 is much larger

than one, the fit is poor. On the other hand, if the reduced χ^2 is much below one, this indicates that the errors on the data have been over-estimated.

The last point is to determine a confidence interval for each parameter (i.e. a range of values within which one can be confident to find the true value). This interval is computed by varying each parameter value until the χ^2 increases by a particular amount above the minimum, or 'best-fit' value (Lampton et al. 1976).

6.1.1 C(I): The Observed Spectrum

The observed spectrum of a source is actually not only containing the counts of the source but also counts of the background. A local background spectrum has to be subtracted from each source spectrum via some scaling factors.

As shown in Sect 2.2.1 of the XSPEC manual, the background-subtracted count rate is then given by:

$$C(I) = \frac{D(I)}{a_{\rm D}(I)t_{\rm D}} - \frac{b_{\rm D}(I)B(I)}{b_{\rm B}(I)a_{\rm B}(I)t_{\rm B}} \tag{6.3}$$

where $D(I)$ and $B(I)$ are the counts for the source and the background; $t_{\rm D}$ and $t_{\rm B}$ are the corresponding exposure times (given by the EXPOSURE keyword); $b_{\rm D}(I)$ and $b_{\rm B}(I)$ are the respective BACKSCAL (detector area) values; and $a_{\rm D}(I)$ and $a_{\rm B}(I)$ are the respective AREASCAL (effective area) values.

This corrected spectrum, $C(I)$, is the one to which the theoretical model will be fitted.

6.1.2 R(I,E): The Instrumental Response

The characteristics of the detector are given by its instrumental response, $R(I, E)$. This response is proportional to the probability that an incoming photon of energy E will be detected in channel I. This continuous function must be converted to a discrete one, which is the response matrix $R_{\rm D}(I, J)$ for each instrumental channel I and each energy channel J.

The energy channels, E_J, must be defined such that:

$$R_{\rm D}(I, J) = \int_{E_{J-1}}^{E_J} \frac{R(I, E)}{E_J - E_{J-1}}\, dE \tag{6.4}$$

Optionally an auxiliary response file $A_{\rm D}(J)$ can be used. This file characterizes the effective collecting area, which is energy dependent. This function is multiplied with the previous one as follows:

$$R_{\rm D}(I, J) \rightarrow R_{\rm D}(I, J) * A_{\rm D}(J) \tag{6.5}$$

Conventionally, the response is in units of $\rm cm^2$.

6.1.3 $f(E)$: The Model Spectrum

The observed spectrum, $C(I)$, is then defined by:

$$C(I) = \int_{E_{J-1}}^{E_J} R_{\rm D}(I, J)\, A_{\rm D}(J)\, f_{\rm D}(J) dJ \tag{6.6}$$

where $f_{\rm D}(J)$ is the theoretical model spectrum for each energy channel J. If $f(E)$ is the continuous theoretical model, it has first to be converted to the discrete form using:

$$f_D(J) = \int_{E_{J-1}}^{E_J} f(E) dE \tag{6.7}$$

which is in units of photons cm^{-2} s^{-1}.

These theoretical models can be very complex and can consists of several additive components (power-laws, bremsstrahlungs, blackbodys,...) and multiplicative components, which modify the additive components by an energy-dependent factor (photoelectric absorption, ...).

6.2 The four most common astrophysical mechanisms for generating X-rays

There are four dominant physical processes that produce X-rays in an astronomical context. Each of these has a characteristic spectral signature (see Figure 6.1 and 6.2). A more complete description can be found in Charles & Seward (1995), Longair (1992) and Rybicki & Lightman (1979).

6.2.1 Thermal bremsstrahlung

A hot gas which has a temperature above 10^5K (kT = 10 eV) is almost fully ionised. In a gas in thermal equilibrium, the trajectory of the electrons is modified by the electric field of the positive ions. This accelerates the electrons which then emit 'bremsstrahlung' radiation. The shape of this bremsstrahlung radiation spectrum, as a function of energy is very characteristic and, for a Maxwellian electron distribution, depends only on the temperature. When the temperature increases, the velocity of the electrons increases and the energy of the emitted radiation becomes higher.

The spectral shape of the thermal bremsstrahlung is shown in Figure 6.1. The intensity, I, of the radiation at energy, E, and temperature, T, is given by:

$$I(E, T) = AG(E, T) Z^2 n_e n_i (kT)^{-1/2} e^{-E/kT} \tag{6.8}$$

where k is the Boltzmann constant, G is the velocity averaged 'Gaunt factor' (a slowly varying function with value increasing as E decreases), Z is the charge of the positive ions, n_e the electron density, n_i the positive ion density, and A is a constant.

6.2.2 Synchrotron radiation

In the same way as the trajectory of electrons can be modified by the electric field of the positive ions, the trajectory of a fast electron can be modified by a magnetic field. The electron is then accelerated and also emits radiation. This radiation is called 'magnetic bremsstrahlung' or 'synchrotron radiation'. The emitted electromagnetic radiation depends only on the energy of the electrons, the magnetic field strength, B, and the direction of motion relative to the field.

However, in astrophysical contexts, the magnetic field can be somewhat aligned, but particle velocities are expected to be isotropic; so the observed spectrum depends only on the magnetic field strength and the energy of the electrons. This spectrum is described by a power law (see Figure 6.1):

$$I(E) = AE^{-\alpha} \tag{6.9}$$

where A is a constant and α is the spectral index. It is related to the electron distribution index, p, by: $\alpha = (p-1)/2$. The larger the value of α, the softer the spectrum.

6.2.3 Blackbody radiation

A 'black' body is an object that completely absorbs any radiation incident upon it. The object is in thermal equilibrium and characterized by a temperature T. The spectrum radiated by such kind of object is a well-defined continuum which depends only on its temperature. If T increases, the radiation is emitted at higher energies.

The form of the spectrum is shown in Figure 6.1. The intensity, I, of the radiation at energy, E, and temperature, T, is given by the Planck formula:

$$I(E,T) = \frac{2\,E^3}{h^2c^2\ (e^{E/kT}-1)} \tag{6.10}$$

where h is the Planck constant, and c is the speed of light.

6.2.4 Compton scattering

In the ordinary Compton scattering process, high energy photons collide with stationary electrons and transfer some of their energy and momentum to the electrons. No new photons are produced but the same photons come out with less energy and momentum, increasing their wavelength. On the other hand, high energy electrons can scatter on low energy photons. This is called the Inverse Compton Scattering. In this

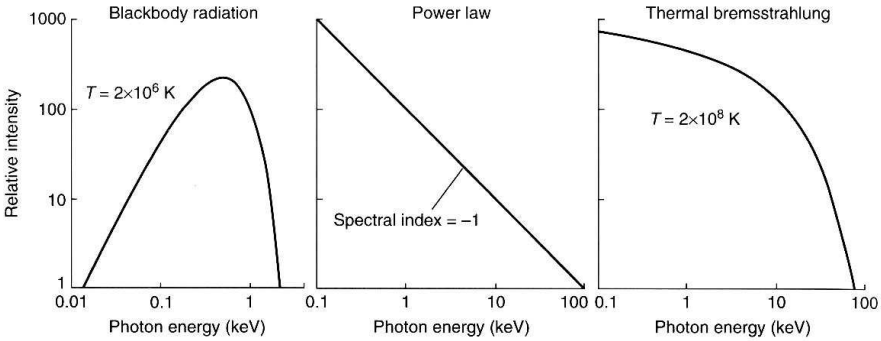

Figure 6.1: Three basic spectra encountered in astrophysics (Charles & Seward 1995). The first is a blackbody spectrum for an object at temperature of 2×10^6 K. The second is a power law with a spectral index of -1. And the third is a thermal bremsstrahlung from a thin and hot gas at temperature of 2×10^8 K.

situation, the photons gain and the electrons loses energy. When electron and photon densities are large enough, the produced spectrum is a continuum.

A typical spectra observed in astrophysical contexts, is the one shown in Fig. 6.2 (Rybicki & Lightman 1979). Considering a thermal distribution of nonrelativistic electrons that experience repeated inverse Compton scattering, the observed spectrum can be described by a power-law with an exponential cutoff:

$$I(x) = \begin{cases} x^3 e^{-x} & \text{for } x \gg 1 \\ x^{3+m} & \text{for } x \ll 1 \end{cases} \tag{6.11}$$

where x is the photon energy $x = h\nu/\mathrm{kT}$ and

$$m = -\frac{3}{2} \pm \sqrt{\frac{9}{4} + \frac{4}{y}} \tag{6.12}$$

$$y = \frac{4kT}{m_e c^2} \max(\tau, \tau^2) \tag{6.13}$$

y is called the Compton parameter and can be defined as the 'average fractional energy change per scattering' multiplied by the 'mean number of scatterings' (Rybicki & Lightman 1979), where τ is the optical thickness of the medium.

The $+(-)$ sign of equation 6.12 is appropriate for $y \gg 1$ ($y \ll 1$), and for $y \sim 1$, one must take a linear combination of the two solutions.

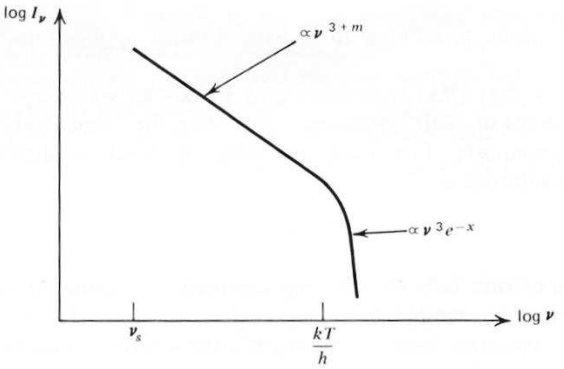

Figure 6.2: The observed emission spectrum produced by the inverse Compton scattering of low energy photons by thermal electrons (Rybicki & Lightman 1979).

6.3 *Spectral fits of the brightest sources*

In the next section I show the results of spectral fitting of the 4 brightest X-ray sources inside the D_{25} optical disk, using XSPEC. I tried several single models (power law, bremsstrahlung or blackbody) and double models composed by a soft component (bremsstrahlung or blackbody) and a hard (power law) component. Results of the spectral fitting are shown in Table 6.1, where PO refers to 'power law', BR to 'bremsstrahlung' and BB to 'blackbody'.

The fits have been made using data from the 3 instruments (pn, MOS1 and MOS2), and both revolutions. The brightest source is the only one for which the hardness ratio has changed significantly between the first and the second observation. So, except for this source, I constrain the parameters of the spectral fitting to be equal for both revolutions. The parameter errors have been estimated using the `error` command of XSPEC.

For each of the sources, the pn-fluxes and luminosities are tabulated separately for the 0.3–6.0 keV (Table 6.2) and 0.3–2.4 keV (Table 6.3) energy bands. The flux uncertainties have been calculated from the spectral fitting after freezing the $N_{\rm H}$ parameter to avoid overestimation of the uncertainties. For source #8, in revolution 192, MOS1 fluxes have been given as the source lies in a pn CCD gap. The 0.3–2.4 keV fluxes and luminosities are compared to the values given by *ROSAT* (Read & Pietsch 2001), after that the luminosities have been recalculated considering a distance to NGC 300 of 1.88 Mpc instead of 2.1 Mpc (Freedman et al. 1992). Figures of the source spectra and the best fitting model, as well as the corresponding residuals, are

also shown.

6.3.1 XMM J005509.9−374212, source #1

Source #1 is a very bright object located within the inner spiral arms of the galaxy (see Fig. 4.1). Its hardness ratio changed significantly between revolution 192 ($HR_{hard} = -0.13 \pm 0.01$, $HR_{soft} = -0.38 \pm 0.02$) and revolution 195 ($HR_{hard} = -0.21 \pm 0.01$, $HR_{soft} = -0.25 \pm 0.01$), indicating that the source became brighter in the medium (1–2 keV) energy band. The best fit is an absorbed model composed of a power law hard component and bremsstrahlung soft component. This source is quite variable: its flux has increased by a factor of ∼2 from the first to the second XMM observation (see Table 6.2 and Table 6.3). Comparing the 0.3–2.4 keV flux with *ROSAT*, the source appears to be fainter with respect to the value found by Read & Pietsch (2001). Note that the Eddington luminosity limit for a $1.4\,M_\odot$ object is $1.82 \times 10^{38}\,erg\,s^{-1}$ and the luminosity of source #1 is found close to and above that. This may suggest the presence of a neutron star X-ray binary with a mass of at least $\sim 1.5\ M_\odot$ or a black hole X-ray binary of several solar masses. Following Read & Pietsch (2001) the source is likely a black hole X-ray binary with a mass they estimated $\sim 5\ M_\odot$ and a luminosity of $2.2 \times 10^{38}\,erg\,s^{-1}$.

From the position of the source in the color-color diagram, it is likely a LMXB. However, a HMXB cannot to be excluded as black hole HMXBs are expected to have similar spectra as the black hole LMXBs and as the source has been found to coincide, from the catalogues, with a Wolf Rayet star (see Table 5.2).

Spectra and spectral fitting of the source according to the best model are shown in Fig. 6.3.

Table 6.1: spectral results

source	model	N_H ($\times 10^{22}$ cm^2)	kT (keV)	Γ	χ^2	dof	χ^2_ν
1 (192)	PO+BR	$0.08^{+0.05}_{-0.04}$	$0.28^{+0.04}_{-0.06}$	$1.78^{+0.23}_{-0.23}$	566.53	495	1.14
(195)		$0.10^{+0.03}_{-0.02}$	$0.43^{+0.11}_{-0.12}$	$2.25^{+0.20}_{-0.19}$			
3	PO+BR	$0.18^{+0.03}_{-0.07}$	$0.28^{+0.15}_{-0.06}$	$2.24^{+0.34}_{-0.45}$	125.82	116	1.08
7	PO	$0.35^{+0.05}_{-0.03}$		$1.91^{+0.12}_{-0.13}$	154.64	110	1.41
8	BB	$0.11^{+0.04}_{-0.04}$	$0.061^{+0.004}_{-0.003}$		73.29	53	1.38

Table 6.2: Flux (in units of $10^{-13}\,\mathrm{erg\,cm^{-2}\,s^{-1}}$) and luminosity (in units of $10^{38}\,\mathrm{erg\,s^{-1}}$) of *XMM-newton* data in the 0.3–6.0 keV energy band.

source		revol. 192	revol. 195
1	flux	$2.24^{+0.22}_{-0.34}$	$4.73^{+0.63}_{-1.20}$
1	lum.	$0.95^{+0.09}_{-0.14}$	$2.00^{+0.27}_{-0.51}$
3	flux	$0.91^{+0.15}_{-0.21}$	$1.21^{+0.15}_{-0.20}$
3	lum.	$0.38^{+0.06}_{-0.09}$	$0.51^{+0.06}_{-0.08}$
7	flux	$1.29^{+0.07}_{-0.08}$	$0.99^{+0.06}_{-0.06}$
7	lum.	$0.55^{+0.03}_{-0.03}$	$0.42^{+0.03}_{-0.03}$
8 (MOS1)	flux	$0.91^{+0.26}_{-0.27}$	$0.44^{+0.10}_{-0.10}$
8 (MOS1)	lum.	$0.38^{+0.11}_{-0.11}$	$0.19^{+0.04}_{-0.04}$

Table 6.3: Flux (in units of $10^{-13}\,\mathrm{erg\,cm^{-2}\,s^{-1}}$) and luminosity (in units of $10^{38}\,\mathrm{erg\,s^{-1}}$) of *XMM-Newton* data in the 0.3–2.4 keV energy band and the 0.1–2.4 keV *ROSAT* values.

source		revol. 192	revol. 195	*ROSAT*
1	flux	$1.61^{+0.20}_{-0.23}$	$3.57^{+0.48}_{-1.01}$	4.22 ± 0.14
1	lum.	$0.69^{+0.08}_{-0.10}$	$1.51^{+0.20}_{-0.43}$	1.78 ± 0.06
3	flux	$0.72^{+0.13}_{-0.14}$	$0.92^{+0.12}_{-0.13}$	1.31 ± 0.08
3	lum.	$0.30^{+0.05}_{-0.06}$	$0.39^{+0.05}_{-0.05}$	0.55 ± 0.03
7	flux	$0.57^{+0.04}_{-0.04}$	$0.44^{+0.03}_{-0.03}$	0.24 ± 0.04
7	lum.	$0.24^{+0.02}_{-0.02}$	$0.19^{+0.01}_{-0.01}$	0.10 ± 0.02
8 (MOS1)	flux	$0.91^{+0.26}_{-0.27}$	$0.44^{+0.09}_{-0.09}$	0.99 ± 0.08
8 (MOS1)	lum.	$0.38^{+0.11}_{-0.11}$	$0.19^{+0.04}_{-0.04}$	0.42 ± 0.03

6.3.2 *XMM J005510.8−374834, source #3*

Source #3 is the second brightest source within the D_{25} optical disk. This source is located at the edge of the disk (see Fig. 4.1). Its hardness ratio $\mathrm{HR_{hard}} = -0.21$ and $\mathrm{HR_{soft}} = -0.30$ (see Table 5.1), is quite similar to source #1. The best fitting model is an absorbed power law plus a bremsstrahlung model. The source luminosity is quite constant within the two revolutions but it is fainter with respect to *ROSAT* data.

Read & Pietsch (2001) suggest that the source is an AGN, but the source seems a bit too soft for that, so I do not exclude the possibility to have an X-ray binary (from its colors, a LMXB). A counterpart is seen in the optical data but except of a radio

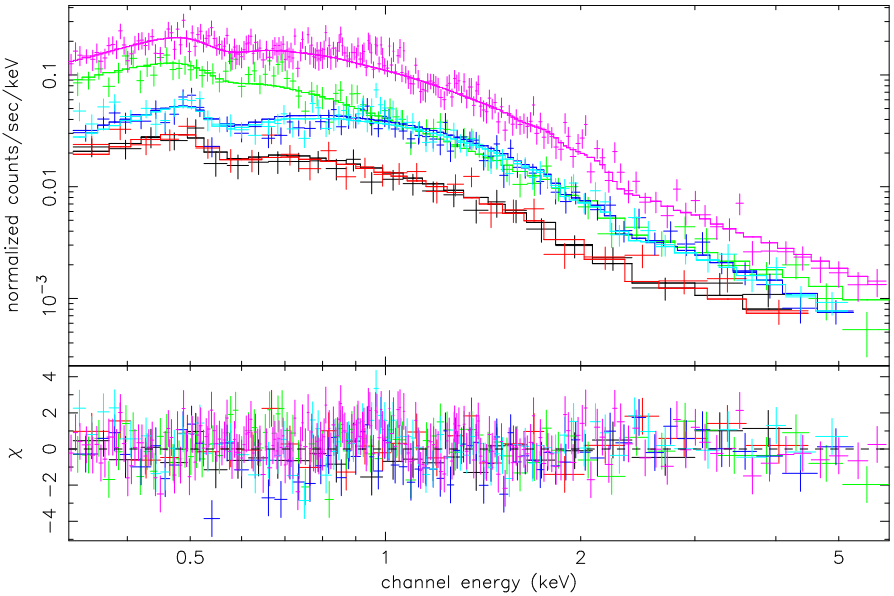

Figure 6.3: pn and MOS spectra of the source XMM J005509.9−374212 (source #1), observed in revolution 192 and 195, and the best fit spectral model, bottom: residuals expressed in σ. Data of MOS1, MOS2 and pn in revolution 192 are shown in black, red and green respectively; data of MOS1, MOS2 and pn in revolution 195 are shown in blue, light blue and magenta respectively.

source no other object seems to be associated. Spectra and spectral fitting are shown in Fig. 6.4.

6.3.3 XMM J005450.2−373849, source #7

Source #7 is the third brightest source within the optical disk. It is located close to the center of the galaxy (see Fig. 4.1). With a hardness ratio of $HR_{hard} = -0.14$ and $HR_{soft} = +0.28$ (see Table 5.1), the source is harder than the previous ones. The best fitting model is an absorbed power law model.

The source flux seems to have slightly decreased between the first and the second revolution, and in *XMM-Newton* data, the source is ∼2 times brighter than in the *ROSAT* observation. A counterpart is seen in optical and radio wavelengths. Thus the source is either a candidate for a background AGN and an accreting binary. This last hypothesis is suggested by Read & Pietsch (2001).

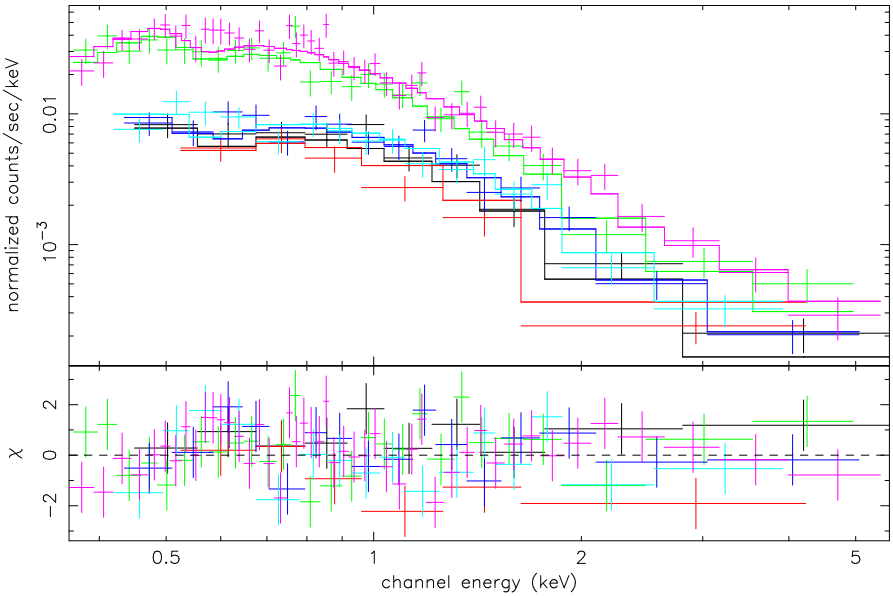

Figure 6.4: pn and MOS spectra of the source XMM J005510.8−374834 (source #3), observed in revolution 192 and 195, and the best fit spectral model, bottom: residuals expressed in σ. Data of MOS1, MOS2 and pn in revolution 192 are shown in black, red and green respectively; data of MOS1, MOS2 and pn in revolution 195 are shown in blue, light blue and magenta respectively.

Spectra and spectral fitting using the best model are shown in Fig. 6.5.

6.3.4 XMM J005510.8−373854, source #8

This source is characterised by an extremely soft spectrum. Its hardness ratios $HR_{hard} = 0.01$ and $HR_{soft} = -0.97$ (see Table 5.1) make this source the softest one of the catalogue. It is located at the very bottom of the color-color diagram (Fig. 4.3). The best fitting model is an absorbed blackbody with a temperature of 61 eV. This source has also been analysed by Kong & Di Stefano (2003a). Their best fitting spectral model for the XMM data is also an absorbed blackbody with a temperature in the range of 57 to 67 eV.

The luminosity decreased by a factor of ∼2 between the first and the second revolution and the *ROSAT* flux is similar to the flux found in revolution 192. Kong & Di Stefano (2003a) measured an unabsorbed luminosity of $9 \times 10^{38}\,\mathrm{erg\,s^{-1}}$ for the first

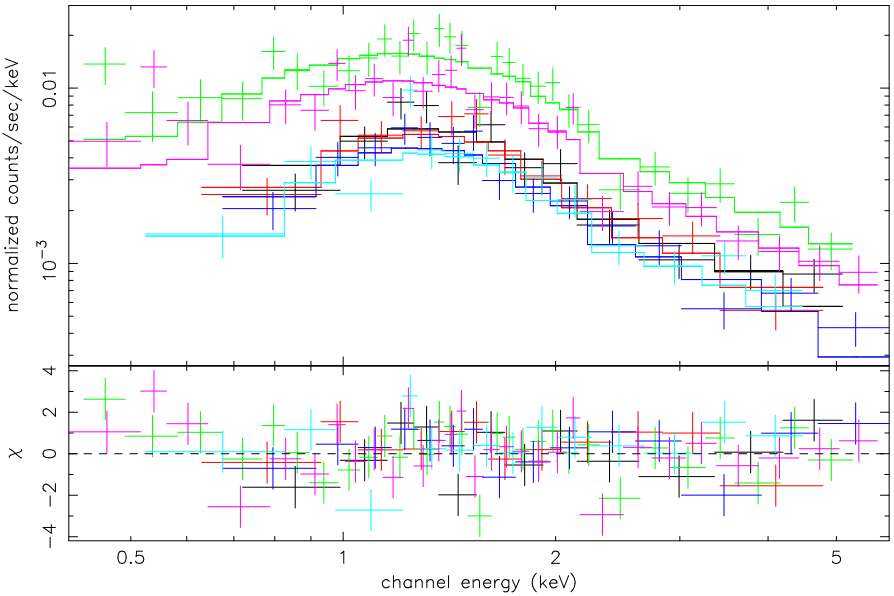

Figure 6.5: pn and MOS spectra of the source XMM J005450.2−373849 (source #7), observed in revolution 192 and 195, and the best fit spectral model, bottom: residuals expressed in σ. Data of MOS1, MOS2 and pn in revolution 192 are shown in black, red and green respectively; data of MOS1, MOS2 and pn in revolution 195 are shown in blue, light blue and magenta respectively.

observation and 1.1×10^{38} erg s^{-1} for the second observation, and 1×10^{39} erg s^{-1} for the *ROSAT* data. They conclude that the source is a SSS and is ultraluminous (i.e., characterized by an unabsorbed luminosity exceeding 1×10^{39} erg s^{-1}). However, for revolution 192, I found a unabsorbed luminosity which is a factor of ~ 2 lower than that, while for revolution 195 my value is similar to what they found. The high luminosity value found by Kong & Di Stefano (2003a) in revolution 192 is likely to be caused by a wrong correction of the presence of the source in the middle of a pn CCD gap.

No counterparts is visible in the optical data and no objects are found close to the position of the X-ray source in any of the catalogues. I agree with the identification made by Kong & Di Stefano (2003a), and proposed by Read & Pietsch (2001), suggesting that the source is a Super Soft Source, but the object seems to be too faint to establish the ultraluminous nature of the source.

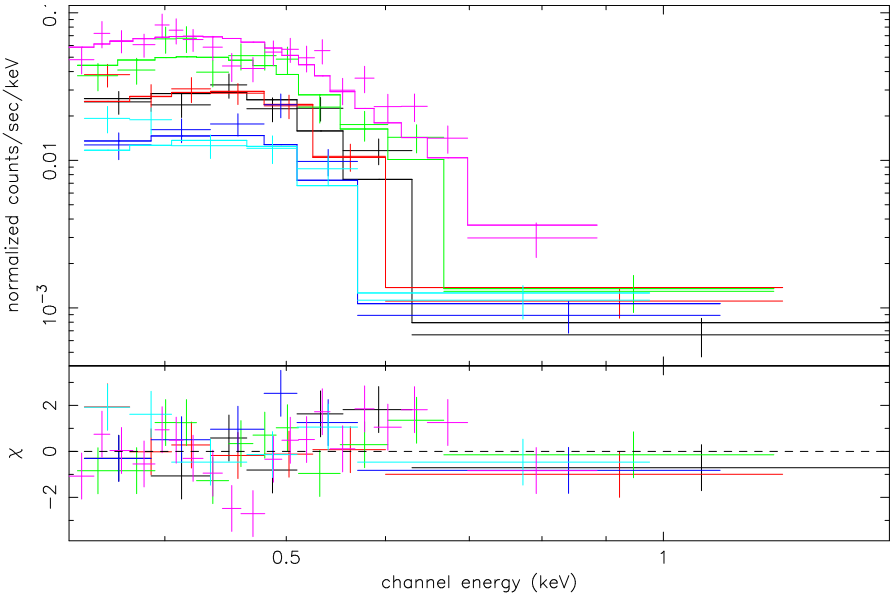

Figure 6.6: pn and MOS spectra of the source XMM J005509.9−374212 (source #8), observed in revolution 192 and 195, and the best fit spectral model, bottom: residuals expressed in σ. Data of MOS1, MOS2 and pn in revolution 192 are shown in black, red and green respectively; data of MOS1, MOS2 and pn in revolution 195 are shown in blue, light blue and magenta respectively.

Spectra and spectral fitting using an absorbed blackbody model are shown in Fig. 6.6.

6.4 *Light curves of the brightest sources*

Fig. 6.7 to 6.10 show the light curves for the 4 brightest sources, separately for revolution 192 and 195, including MOS and PN data after background correction. The gap in the data of revolution 192 for source #1 corresponds to the period of high low energy proton flux. For the other sources, only data before this gap are shown. The time bin size is of 300 sec for the brightest source and 1000 sec for the others.

To test the significance of the sources variability, I fit a constant value to the light curves using the IDL routine `poly_fit`. From the resulting χ^2, I determine the prob-

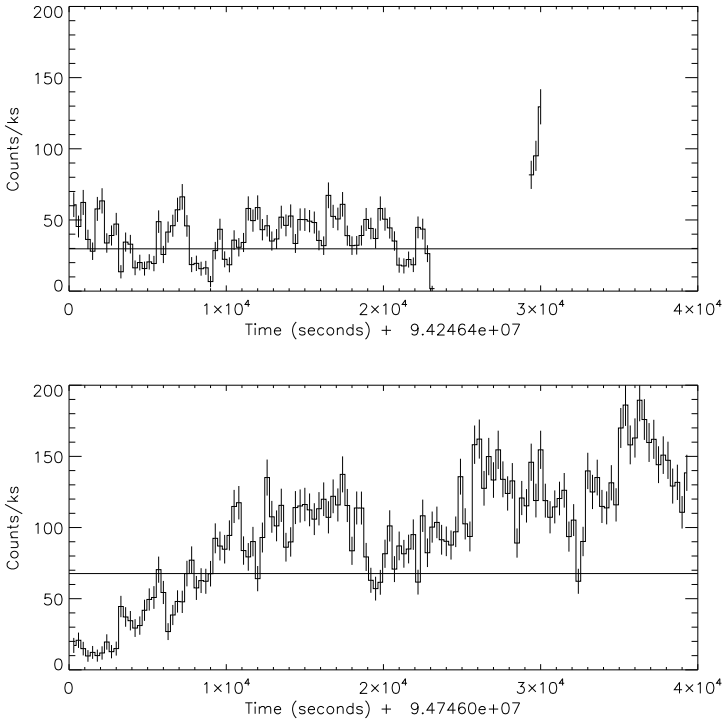

Figure 6.7: pn and MOS light curve of the source XMM_J005509.9-374212 (source #1), observed in revolution 192 (top) and revolution 195 (bottom). The horizontal line shows the fitted mean value.

ability (P) that the source is variable:

$$P = \gamma(\nu/2, \chi^2/2) \tag{6.14}$$

where ν is the number of degrees of freedom, χ^2 is the chi-square value, and γ is the incomplete gamma function:

$$\gamma(a,b) = \frac{1}{\Gamma(a)} \int_b^\infty e^{-t} t^{a-1} dt \tag{6.15}$$

where Γ is the gamma function:

$$\Gamma(n) = \int_0^\infty u^{n-1} e^{-u} du \tag{6.16}$$

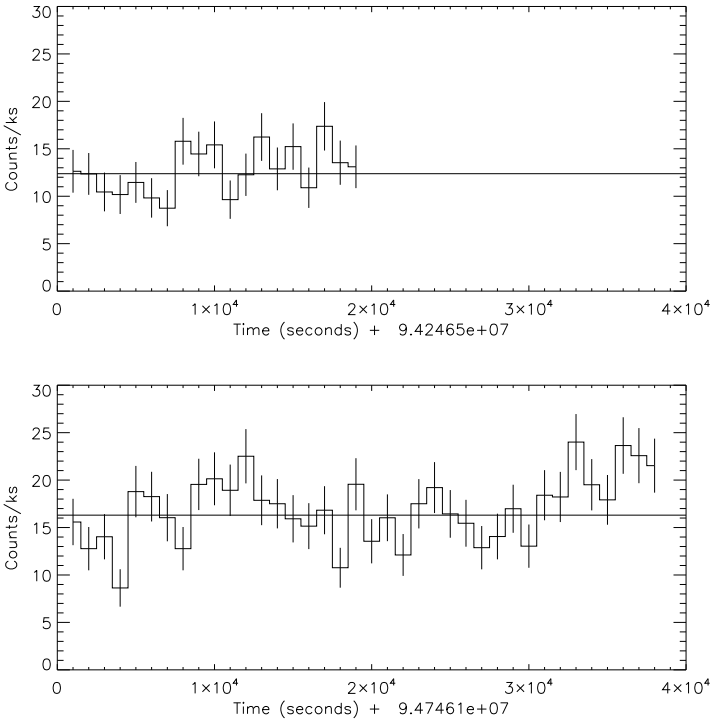

Figure 6.8: pn and MOS light curve of the source XMM_J005510.8-374834 (source #3), observed in revolution 192 (top) and revolution 195 (bottom). The horizontal line shows the fitted mean value.

Results of these fits are shown in Table 6.4. Note that the results depend on the binning size.

The lightcurve of source #1 is quite interesting. During revolution 192 the flux does not present important fluctuations but it increases significantly after the data gap. In revolution 195 the mean flux increases gradually, while large modulations are present. In both cases, the probability of variation is of 100%, and the 1σ error of the mean value are almost as large as the values themselves.

Light curves for source #3 and source #7 do not show large fluctuations in any of the revolutions. For source #3 in both revolutions and source #7 in revolution 195 the relative erros are of ∼1/4–1/5. For source #7 in revolution 192, this value is only of ∼1/9. The probability of variation for source #3 are of 76% and almost 100% for

Table 6.4: Results of the light curves fit with a constant value, the columns show: the source ID, the mean fitted value and its 1σ error, the χ^2 and number of degrees of freedom, and the corresponding probability of variation.

source (revol.)	mean value (cts/ks)	χ^2/dof	Prob. variation (%)
1 (192)	29.72 ± 22.51	736/79	100.00
1 (195)	67.66 ± 51.06	3390/130	100.00
3 (192)	12.38 ± 2.52	22/18	76.30
3 (195)	16.31 ± 3.61	76/37	99.98
7 (192)	16.64 ± 1.81	9/18	3.27
7 (195)	11.66 ± 2.79	62/37	99.42
8 (192)	9.16 ± 2.18	21/18	73.29
8 (195)	6.66 ± 3.03	130/37	100.00

revolution 192 and 195, respectively. For source #7 in its revolution 192 the light curve is well fitted by a constant value (the probability of variation is only 3%), while in its revolution 195 the probability of variation is of 99%.

For source #8 the light curve is relatively flat in revolution 192 and exhibits some hump around 1.5×10^4 ksec from the start of the observation; the relative error is ∼1/4. In revolution 195, the light curve present some modulation, and the relative error increased to ∼1/2. The probability that the flux is variable is of 73% and 100% for revolution 192 and 195 respectively.

The light curves of source #8 were analysed by Kong & Di Stefano (2003a). Using Lomb-Scargle periodograms (Lomb 1976; Scargle 1982), they fond a modulation of 5.4 h with a confidence level above 99.9% in revolution 195. Kong & Di Stefano (2003a) conclude that this modulation correspond to the orbital period of the binary system. However, the data are too short (∼ 11 h) to establish the presence of a periodic signal, and the statistics is too low to perform Lomb-Scargle periodograms.

Analysis of the light curves using periodograms is not possible as the statistics is too low (short exposure times and low count rates). I also searched for short-time periodic modulation using the Epoch-folding and Bayesian methods, but no evident periodicity has been found. Results are shown in Fig. 6.11 to 6.14. Descriptions of both methods are given in Appendix B.

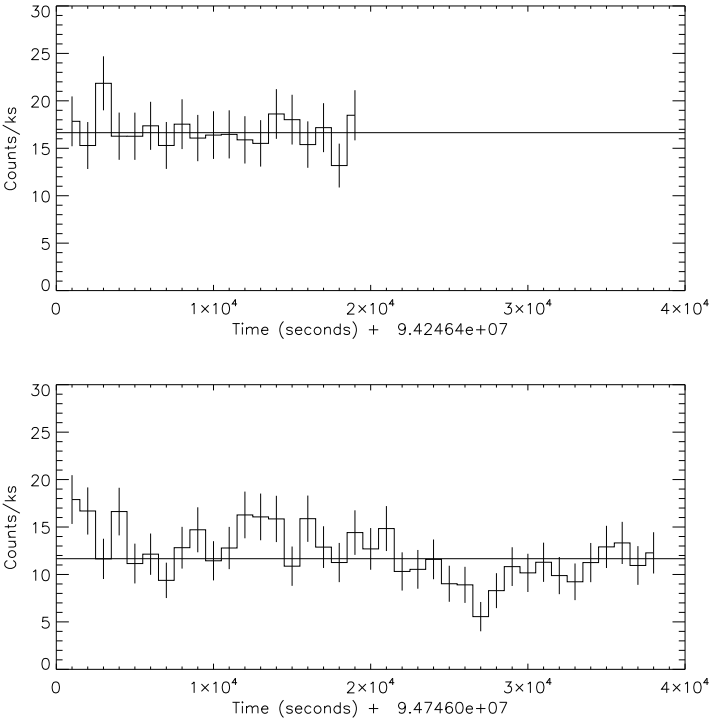

Figure 6.9: pn and MOS light curve of the source XMM_J005450.2-373849 (source #7), observed in revolution 192 (top) and revolution 195 (bottom). The horizontal line shows the fitted mean value.

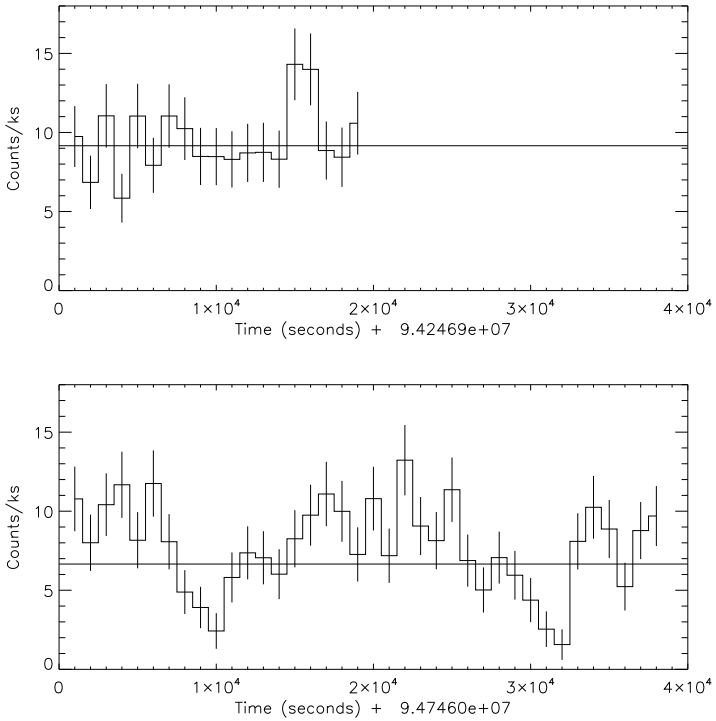

Figure 6.10: pn and MOS light curve of the source XMM_J005510.8-373854 (source #8), observed in revolution 192 (top) and revolution 195 (bottom). The horizontal line shows the fitted mean value.

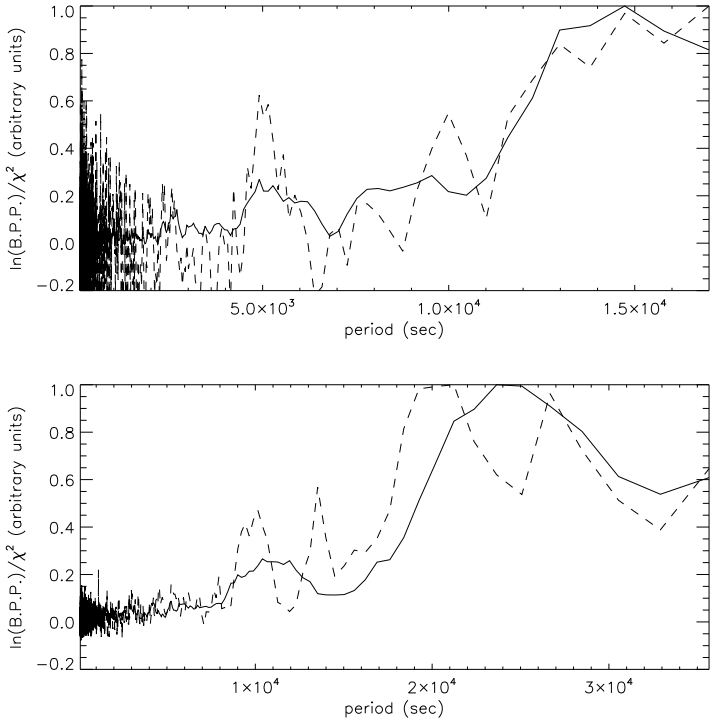

Figure 6.11: Neperian logarithm of the Bayesian posterior probability for the range of periods (full line) and the corresponding chi-square (dashed line), for the pn and MOS data of the source XMM_J005509.9-374212 (source #1), observed in revolution 192 (top) and revolution 195 (bottom). The units are arbitrary.

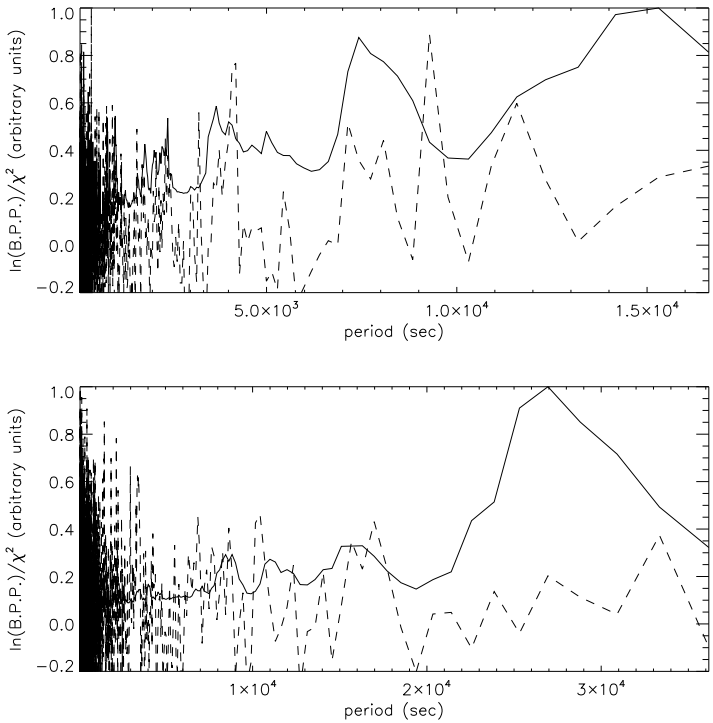

Figure 6.12: Neperian logarithm of the Bayesian posterior probability for the range of periods (full line) and the corresponding chi-square (dashed line), for the pn and MOS data of the source XMM_J005510.8-374834 (source #3), observed in revolution 192 (top) and revolution 195 (bottom). The units are arbitrary.

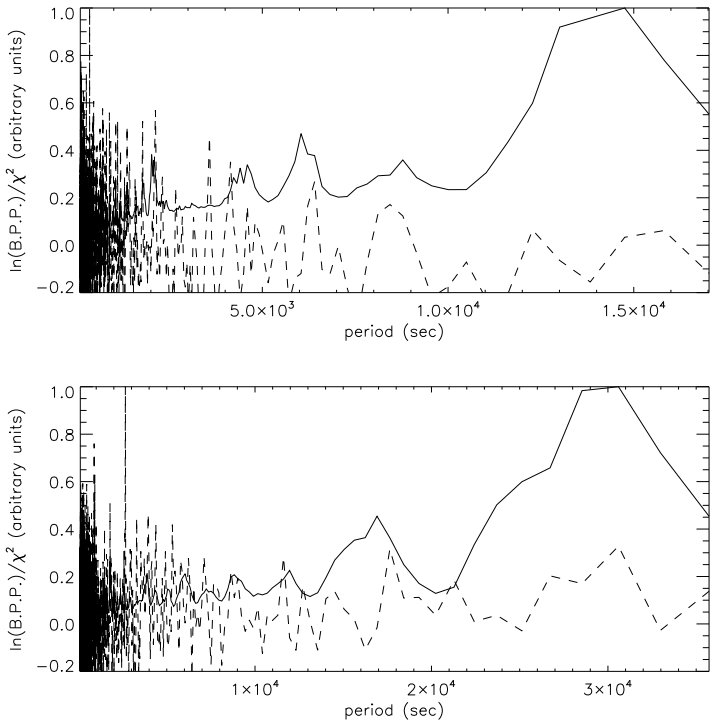

Figure 6.13: Neperian logarithm of the Bayesian posterior probability for the range of periods (full line) and the corresponding chi-square (dashed line), for the pn and MOS data of the source XMM_J005450.2-373849 (source #7), observed in revolution 192 (top) and revolution 195 (bottom). The units are arbitrary.

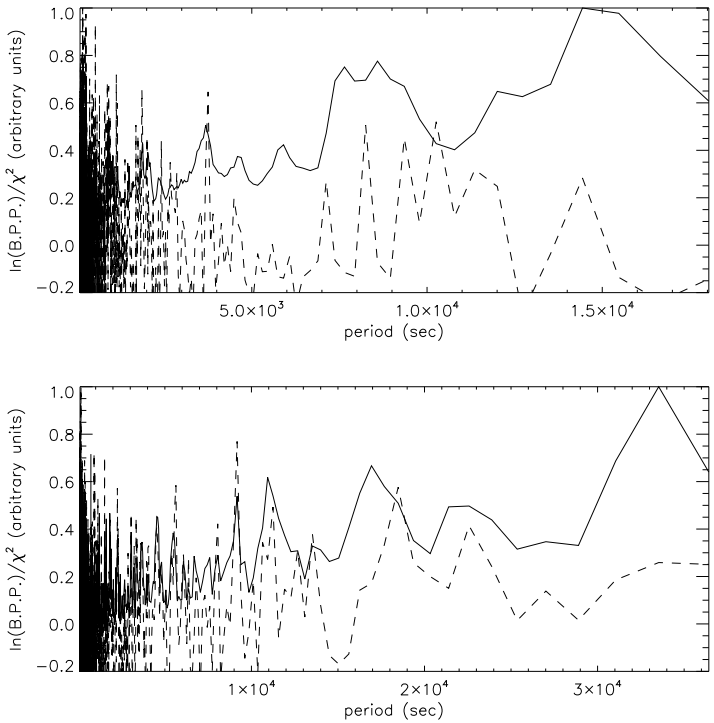

Figure 6.14: Neperian logarithm of the Bayesian posterior probability for the range of periods (full line) and the corresponding chi-square (dashed line), for the pn and MOS data of the source XMM_J005510.8-373854 (source #8), observed in revolution 192 (top) and revolution 195 (bottom). The units are arbitrary.

Chapter 7

Conclusions and future work

7.1 Conclusions

In this PhD work, I have attempted to characterize, classify and, when possible, to identify the X-ray population belonging to the normal spiral galaxy NGC 300. In Chapter 4, I gave global X-ray properties for the 86 sources detected inside the optical disk, above a maximum likelihood threshold of 10 in the 0.3–6 keV energy band. For sources with more than 20 net counts, the color-color diagram (Fig.4.3) is derived and, via a theoretical diagram (Fig.4.4), the corresponding spectral model and flux are determined. These are ranging from 3.49×10^{-13} erg cm^{-2} s^{-1} for the brightest one to 7.09×10^{-16} erg cm^{-2} s^{-1} for the dimmest. Two sources have been found to be variable within the two revolutions (i.e. within 6 days). Their ID numbers are: 1 and 7. Source #1 is the only source for which color changed significantly between the two observations. A summary of all these results can be found in Table 5.1.

From the position of the sources in the color-color diagram, comparing the diagram with those from other galaxies and cross-correlating the objects with catalogues (see Chapter 5), I attempted to classify the sources in 6 categories according to criteria given in Table 4.1. I found 2 foreground stars, 6 AGNs, 1 SSS, 14 SNRs, 39 LMXBs and 9 HMXBs. LMXBs seem thus to be dominant in the X-ray binary population of NGC 300. The two variable sources are all found in the LMXB class. Again this is only an attempt for classification, as there can be overlaps between categories due to similarities of spectra and/or because of absorption. Selection criteria used for other spiral galaxies (Soria & Wu 2003; Jenkins et al. 2005; Prestwich et al. 2003; Pietsch et al. 2005, 2004) are consistent with my data.

The luminosity function of the softer sources (mainly SNRs) and the harder sources (mainly X-ray binaries) have been compared with the luminosity function derived for several classes of galactic objects. The plots show that the softer sources, as the galactic SNRs can be fitted by a power law function. On the other hand, the harder sources, as the galactic LMXBs can be described by a modified power law which

takes into account the gradual steepening of the $\log N$–$\log S$ relation towards higher fluxes. The $\log N$–$\log S$ diagram for all sources inside the optical disk has a slope (1.15±0.17) which is similar to other nearby spiral galaxies (Williams et al. 2004; Humphrey & Buote 2004; Colbert et al. 2004; Kilgard et al. 2005).

I also characterized the central diffuse emission spectrum with a 2-component thermal emission from a collisionally ionized plasma, with temperatures of $kT = 0.2 \pm 0.01\,\mathrm{keV}$ and $kT = 0.8 \pm 0.1\,\mathrm{keV}$. Similar results have been found for the nearly face-on spiral galaxy M101 (Kuntz et al. 2003).

The second part of this work is focused on the optical counterparts of the X-ray sources using wide field images from the ESO archive. I first corrected the X-ray coordinates for a systematic shift between X-ray and optical data: $-1\farcs25 \pm 0\farcs31$ in RA and $-0\farcs17 \pm 0\farcs31$ in DEC. This is close to what has been found from the *XMM-Newton* astrometric calibration (Guainazzi et al. 2004). Using the IDL `idlphot` photometry library, I searched the optical counterparts from the corrected X-ray positions within a 2σ X-ray position area. Coordinates and magnitudes for all optical counterparts have been calculated and are given in Table 5.2.

I then cross-correlated the X-ray sources and optical counterparts with SIMBAD, USNO-A2.0 and radio catalogues. 14 sources had already been observed in X-rays, there are 9 SNRs or suspected SNRs, 11 radio sources, from which 3 are associated with SNRs. Other sources match with associations of stars, H II (ionized) regions, with regions close to Cepheid variable stars, or with stars. The brightest source is found to be associated with a Wolf Rayet star. Many sources have an USNO-A2.0 optical counterpart. The results can also be found in Table 5.2.

In the last part of the work, I focused on the spectral and temporal analysis of the four brightest sources. Source #1, located in the one of the inner spiral arms of the galaxy, is variable in flux and in colors with the 6 days separating the 2 observations. Its flux is close to/higher than the Eddington limit for a 1.4 $M_\odot$ compact object. Its spectrum can be described by a power law and a bremsstrahlung component, and the light curve shows important fluctuations. The source can be a neutron star or a black hole X-ray binary. It is likely a LMXB, but a HMXB cannot be excluded as a Wolf Rayet star is found to coincide with its position.

Source #3, located at the edge of the disk, has a flux which is slightly variable within the 6 days. Its spectrum is also described by a power law and a bremsstrahlung component, and the light curves do not show large fluctuations in any observations. An optical counterpart has been detected and a radio source is correlated from the catalogues. From its relatively soft spectrum, the source is more likely a X-ray binary (LMXB) than a background AGN.

Source #7, located close to the center of the galaxy is a hard source. Its flux is variable within the 6 days and the spectrum can be described by a pure power law. The light curve in revolution 192 is almost constant, while for revolution 195, it is

more variable. As for source #3, a counterpart is seen in the optical data and a radio source is associated. The source can be either a background AGN or an X-ray binary.

Finally, source #8 is characterized by an extremely soft spectrum. This is described by a blackbody model with a temperature of 61 eV. The source is a SSS and no optical counterpart is visible from the ESO images and no object is associated from the catalogues. In revolution 195, there is some modulation of the light curve, but because the observation time of the data is too short, I cannot certify the presence of a periodic signal.

I also searched for short-term periodic signals using the Epoch-folding and Bayesian methods, but no evident periodicities have been found.

7.2 Future work

NGC 300 has been re-observed on 2005 May 22 and another observation is planned for November 2005. These new data will allow me to make deeper analysis of the galaxy. The main topics will be:

1. **Studying the long-term flux evolution of the point sources** will allow to discriminate between transient sources, such as black hole X-ray binaries/LMXBs in outburst, persistent HMXBs, and neutron stars LMXBs. An especially important source is the supersoft source (source #8), which has been shown to be strongly variably on timescales from minutes to years (Kong & Di Stefano 2003a). According to Kong & Di Stefano (2003a), between the 2000 December and the 2001 January observations, the unabsorbed flux of this source changed from a high state value with $L_X \sim 10^{39}$ erg s^{-1} to a lower flux state with $L_X \sim 10^{38}$ erg s^{-1}, where they found a periodic signal of 5.4 hr. Further data are necessary to study these large luminosity variations and the corresponding X-ray spectrum, and to understand the phenomenology of supersoft sources.

2. **Identifying background AGN and spectral analysis**: the contamination of the luminosity function by background AGN is very problematic, especially outside of the bulge. To discriminate between AGN and NGC 300 point sources, I will use spectral variability analysis. State changes and distinct changes of their spectral properties are rare for AGNs but common for XRBs.

3. **Increasing the X-ray inventory of NGC 300 to lower luminosities**. Doubling the total observing time of NGC 300 will push the detection limit to lower luminosities (10^{35} erg s^{-1}) and will increase the number of sources in my catalogue. Source positions and colors for the already-detected sources will also be improved. As in this work, I will use our ESO data to identify optical counterparts and study the multiwavelength properties of these sources.

4. **Studying the galaxy cluster CL0053−37** will be possible thanks to the slightly modified pointing. This cluster has previously been studied using the optical data set (Schirmer et al. 2003). It consists of two condensed sub-clumps which are likely in a pre-collision phase and there is strong evidence for two extended filaments, along which a possible matter infall could occur. This indicates that we see a very young cluster in formation. In the previous XMM observations of NGC 300 only the outermost X-Ray halo of the cluster falls in the field of view, missing the two central clumps and the filaments.

Appendix A

Optical counterpart images

Fig. A.1 to Fig. A.6 show the resulting optical counterparts in the merged optical image, for the 86 X-ray sources detected within the optical disk (see Section 5 for more details.)

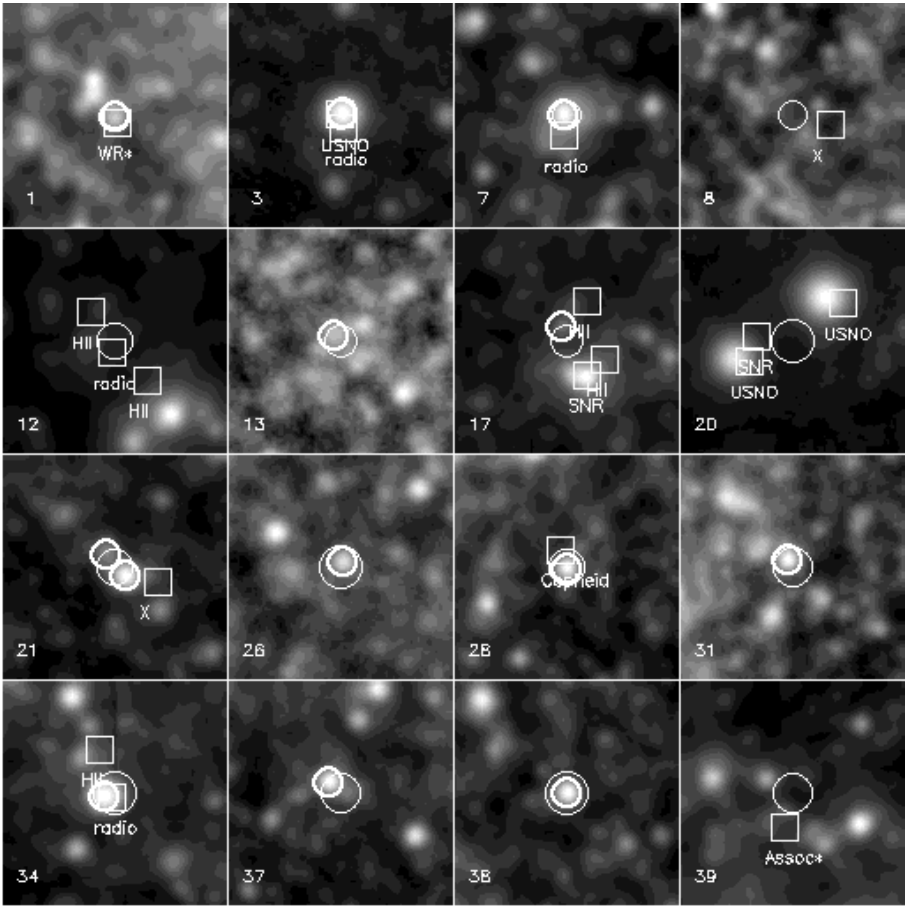

Figure A.1: $15'' \times 15''$ optical images of the region centered on the corrected position of the 16 brightest X-ray sources inside the D_{25} optical disk. The circle indicates the 2σ positional error of the X-ray coordinates, the thicker circles show the optical sources found within the X-ray error circle for X-ray sources which have a 1σ position error $\leq 1\farcs5$. Catalogue sources having a distance of less than $5''$ from the X-ray position are shown with a box.

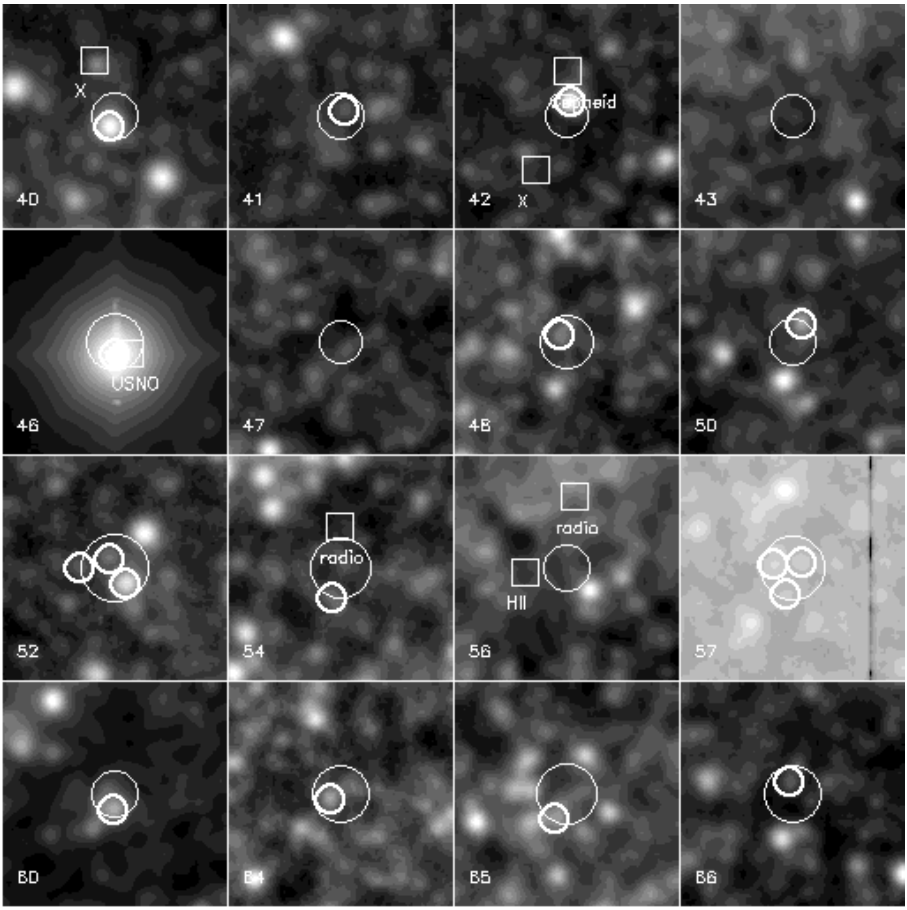

Figure A.2: Same as Fig. A.1 but for the 17th to 32th brightest sources.

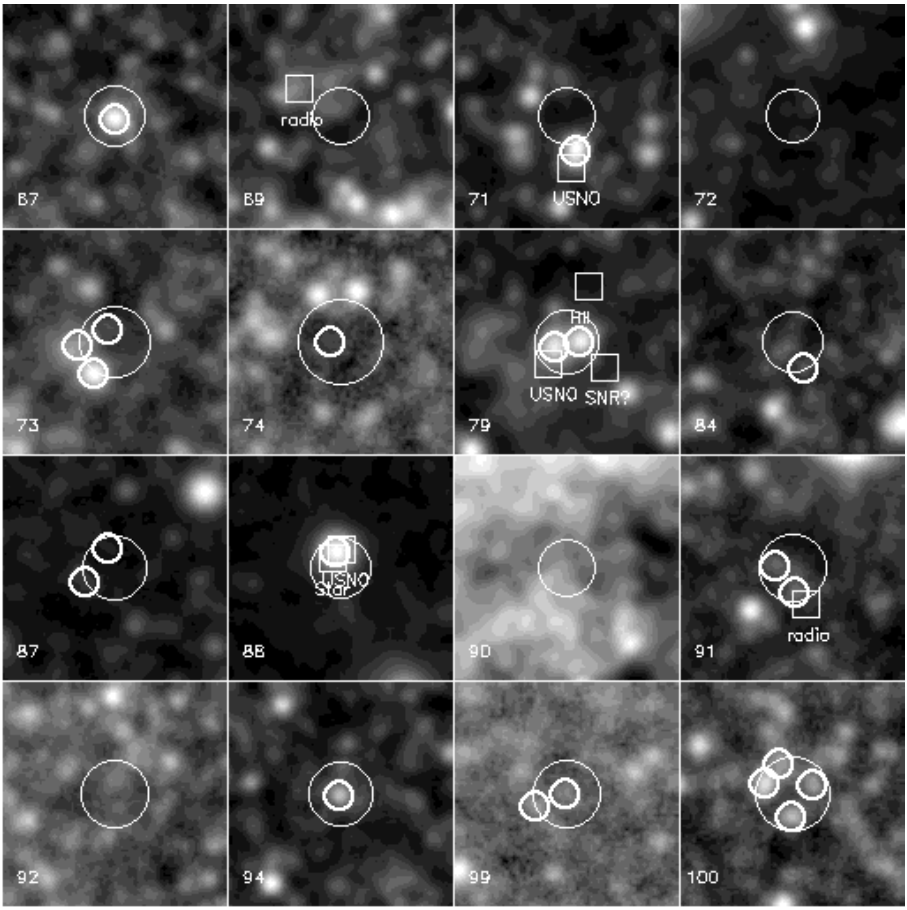

Figure A.3: Same as Fig. A.1 but for the 33th to 48th brightest sources.

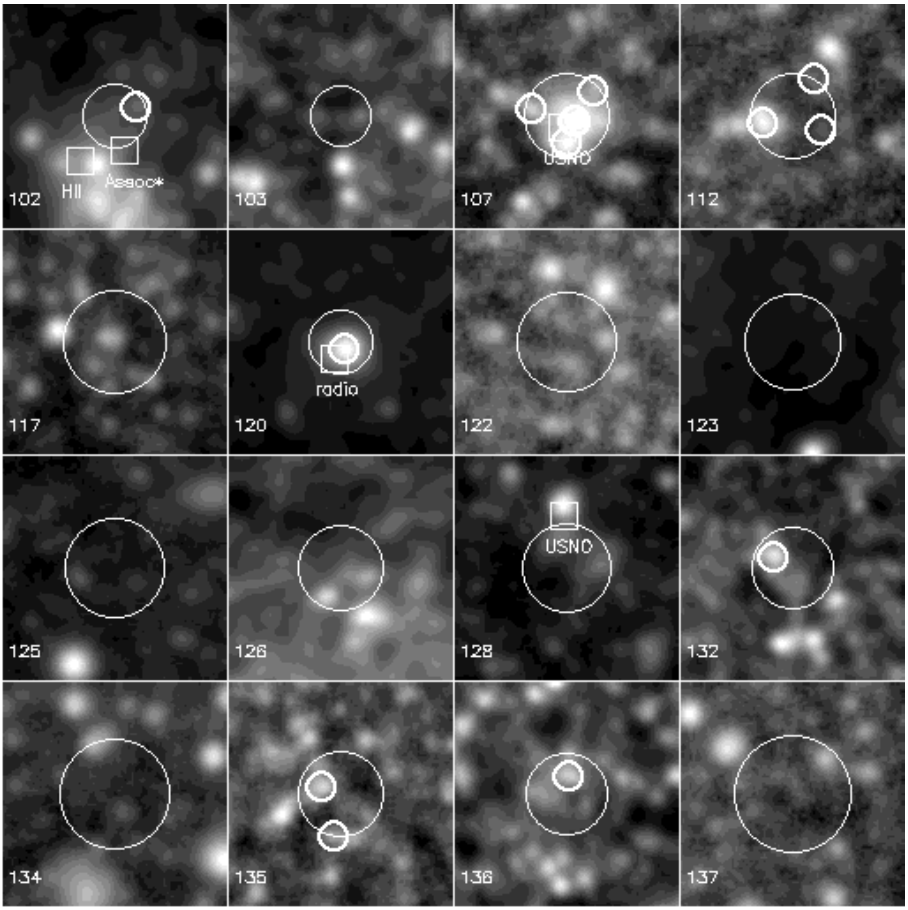

Figure A.4: Same as Fig. A.1 but for the 49th to 64th brightest sources.

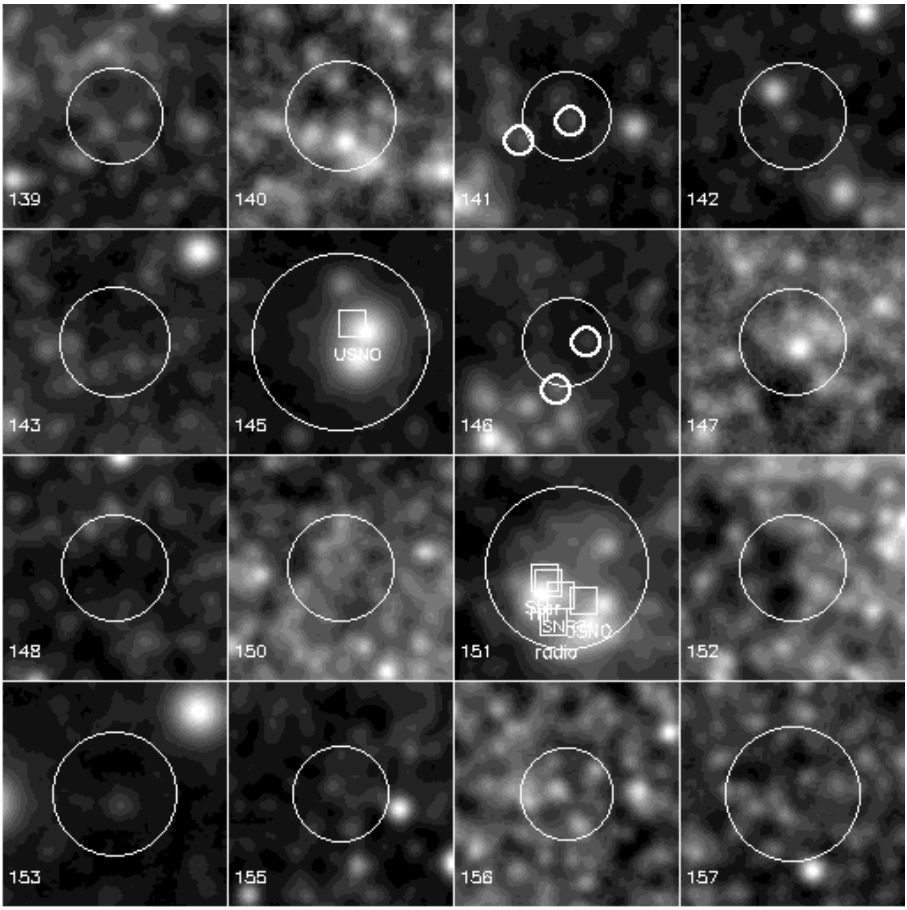

Figure A.5: Same as Fig. A.1 but for the 65th to 80th brightest sources.

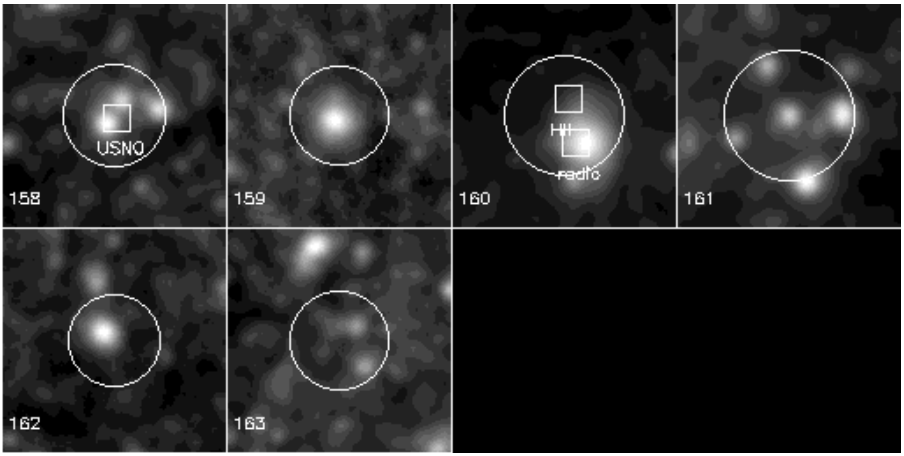

Figure A.6: Same as Fig. A.1 but for the 81th to 86th brightest sources.

Appendix B

Epoch folding and Bayesian methods

Here a description of two methods are given which are used in searching periodic signals in time series: the epoch folding method and a Bayesian periodic signal detection method.

B.1 Epoch folding method to search for periodicities

The epoch folding method is a technique to search for a periodic signal in time series. It is more efficient that the traditional Fourier Transform to find nonsinusoidal pulse shapes, which are characteristic for X-ray pulses. Another advantage of this method is that it is less sensitive to data gaps, and that it can be applied to cases of non evenly sampled data.

The main operation is to fold the data modulo a trial period. Considering a time series of N observations, x_i ($i = 1, \ldots N$), folded at a trial period into M phase bins, then the epoch-folding statistics can be defined by (Davies 1990; Leahy et al. 1983):

$$Q^2 = \sum_{j=1}^{M} \frac{(\bar{x_j} - \bar{x})^2}{\sigma_j^2} \tag{B.1}$$

where $\bar{x_j}$ is the mean of x_i in the jth phase bin, and σ_j^2 is the population variance of $\bar{x}$. The epoch-folding statistic Q^2, for each tested period will have approximately a χ^2 distribution with $M - 1$ degrees of freedom, and a periodicity in the data is indicated by anomalously high value of Q^2.

B.2 Introduction to Bayesian inference

Bayesian methods are an alternative to epoch folding to search for periodic signals. Here I give a short overview of the Bayesian theory and its application to the temporal analysis of data. A good description of Bayesian data analysis can be found in

Gregory (2005) and Loredo (1990).

B.2.1 Frequentist and Bayesian view of defining probabilities

There are two different ways of assigning probabilities, both used in physical science. In conventional statistics, the probability of an event is identified by the long-run relative frequency of occurrence, in a sequence of identical repeats of an experiment. This is commonly called the 'frequentist' view.

In the Bayesian probability theory the definition of 'probability' is much more general. This is regarded as a real number measure of the plausibility of a proposition/hypothesis, given the truth of some a priori information. Of course, none of the probability definition is more correct than the other. The choice for one definition depends on the type of the problem one can encounter, sometimes both approaches are appropriate.

B.2.2 Bayes' Theorem

There are two fundamental mathematical operations for manipulating probabilities. These are the sum rule,

$$p(A \mid B) + p(\bar{A} \mid B) = 1, \tag{B.2}$$

and product rule,

$$p(A, B \mid C) = p(B \mid C)p(A \mid B, C) = p(A \mid C)p(B \mid A, C) \tag{B.3}$$

where the symbols, A, B, C, represent propositions, $\bar{A}$ represents the denial of A, and two symbols separated by a comma ('A, B') means that both propositions are true. The vertical bar, |, is the conditional symbol, indicating what information is assumed to be true for the assignment of a probability.

From a rearrangement of the terms in the product rule, we find that:

$$p(A \mid B, C) = p(A \mid C)\frac{p(B \mid A, C)}{p(B \mid C)} \tag{B.4}$$

This is Bayes' theorem.

Let $A = H$, an hypothesis that we want to test and $B = D$, some data that is relevant to the hypothesis. Let $C = I$, some prior ('a priori') information indicating the way in which H and D are related, and also specifying any alternatives we may have to H. The usual form of the Bayes' theorem then becomes:

$$p(H \mid D, I) = p(H \mid I)\frac{p(D \mid H, I)}{p(D \mid I)} \tag{B.5}$$

Bayes' theorem provides a model for a learning process: it tells us that our posterior ('a posteriori') probability of H, $p(H \mid D, I)$, is obtained by multiplying our prior

probability $p(H \mid I)$ by the probability of the data assuming the truth of the hypothesis, $p(D \mid H, I)$, and dividing it by the probability that we would have seen the data anyway, $p(D \mid I)$. The factor $p(D \mid H, I)$ is also called the likelihood function, $L(H)$, and $p(D \mid I)$ is sometimes called the global likelihood, and usually plays the role of a normalization constant.

Note that 'prior probability,' and 'posterior probability' do not refer to temporal connections, but to logical ones.

B.2.2.1 The Principle of Indifference

The next point consists of deciding how prior probabilities should be assigned. This is done via the Principle of Indifference. This rule is defined for the assignment of probabilities to a finite, discrete set of propositions that are mutually exclusive and exhaustive. The principle asserts that if there is no available evidence providing any reason for considering one proposition to be more or less likely than a second proposition, then one should assign equal probabilities to both propositions. It follows that if one has N mutually exclusive and exhaustive propositions, and no evidence distinguishing them, each proposition should be assigned with a probability of $1/N$.

B.2.3 Parameter estimation and marginalization

We consider a single parameter, θ and assume that a hypothesis is true for some unknown value of this parameter. Let D a proposition asserting that the data are actually observed and I the prior information specifying, for example, how the hypothesis and the data are related. From Bayes's Theorem, we have:

$$p(\theta \mid D, I) = p(\theta \mid I)\frac{p(D \mid \theta, I)}{p(D \mid I)} \tag{B.6}$$

where $p(\theta \mid I)$ is the prior probability for parameter θ and $p(D \mid \theta, I)$ is the corresponding likelihood. Note that $p(D \mid I)$, the global likelihood, plays the role of a normalization constant.

The different values of the parameter θ (θ_1, θ_2,...), must satisfy the condition:

$$p(D \mid I) = \sum_i p(\theta_i \mid I)p(D \mid \theta_i, I), \tag{B.7}$$

or, if θ is a continuous parameter:

$$p(D \mid I) = \int p(\theta \mid I)p(D \mid \theta, I)d\theta. \tag{B.8}$$

B.2.3.1 Marginalization

Consider a problem where we have two parameters, θ and ϕ, but that we are interested only in the parameter θ. The second parameter, ϕ, is called a 'nuisance paramater' and can be eliminated by an operation (integration) called 'marginalization'. The marginal distribution for θ is (Loredo 1990):

$$p(\theta \mid D, I) = \frac{1}{p(D \mid I)} \int p(\phi \mid I) p(\theta \mid \phi, I) p(D \mid \theta, \phi, I) d\phi. \tag{B.9}$$

B.2.4 Model comparison and Ockham's razor

We consider now that N possible models (M_1, M_2,... M_N) can assert that an hypothesis is truth. These models may, for example, differ in form or in number of parameters. From the Bayes theorem, the posterior probability of a model M_i is:

$$p(M_i \mid D, I) = p(M_i \mid I) \frac{p(D \mid M_i, I)}{p(D \mid I)}. \tag{B.10}$$

In the case we have no prior information prefering one model over the others, the prior probability for each model M_i, $p(M_i \mid I)$=1/N.

In a model comparison problem, we focus on the ratio of the posterior probabilities of the models rather than the probabilities themselves. The ratios are called 'odds'. The odds in favor of model M_i over model M_j is written:

$$O_{ij} = \frac{p(M_i \mid D, I)}{p(M_j \mid D, I)} \tag{B.11}$$

$$= \left[\frac{p(M_i \mid I)}{p(M_j \mid I)} \right] \frac{p(D \mid M_i, I)}{p(D \mid M_j, I)} \tag{B.12}$$

$$= \left[\frac{p(M_i \mid I)}{p(M_j \mid I)} \right] \frac{\int d\theta_i p(\theta_i \mid I_i) p(D \mid \theta_i, I_i)}{\int d\theta_j p(\theta_j \mid I_j) p(D \mid \theta_j, I_j)} \tag{B.13}$$

$$= \left[\frac{p(M_i \mid I)}{p(M_j \mid I)} \right] B_{i,j} \tag{B.14}$$

where the factor in brackets is the called 'prior odds', $B_{i,j}$ is called the Bayes factor and, θ_i and θ_j are the parameters of the model M_i and M_j respectively.

This Bayesian calculation automatically includes a quantitative Ockham's razor: 'simple models are automatically preferred unless a more complicated model provides a significantly better fit to the data' (Loredo 1990).

B.2.5 Application: detection of a periodic signal of unknown shape and period in case of Poisson noise

I now will apply the previous analysis to our problem: the search of a periodic signal of unknown shape and period, when dealing with Poisson noise. For this part, I refer to the article of Gregory & Loredo (1992). The same conclusions, but applied in the case of Gaussian noise, can be found in Gregory (1999).

B.2.5.1 The data

We consider N events, arriving at time t_i, with an arbitrary time-dependent rate $r(t)$, over some observing interval of duration T. The data are $D = t_i, i = 1, \dots N$. From the Poisson distribution, the probability to see n events in a small time interval Δt, about time t is (Gregory & Loredo 1992):

$$p_n(t) = \frac{[r(t)\Delta t]^n e^{-r(t)\Delta t}}{n!} \tag{B.15}$$

We have assumed that the rate does not vary substantially within each small time interval Δt, so the average ratio in the interval is approximately equal to the rate at any time within the interval.

B.2.5.2 Constant and periodic models

We define our models for a periodic signal as following: we consider a stepwise function with a constant rate in each of the m bins per period (where $m \geq 2$). As we have different possible value for m, we deal with a class of models M_m. Each of these models has (m+2) parameters: an angular frequency ω (or equivalently a period, P, with $\omega = 2\pi/P$), a phase ϕ specifying the location of the bin boundaries (please note that ϕ does not reffer to the phase of the eventual founded signal), and m values, r_j specifying the rate in each phase bin, with $j = 1, \dots N$.

The value of the subscript j for any particular time t is given by (Gregory & Loredo 1992):

$$j(t) = \text{int}\{1 + m[(\omega t + \phi) \text{mod} 2\pi]/2\pi\} \tag{B.16}$$

where 'int' denotes the integer value of the expression.

For $m = 1$, the data arrive with a constant event rate; we have thus a 'constant' model M_1. The odds ratios in favor of M_m with respect to the constant model M_1, in the case of unknown period and phase is (Gregory & Loredo 1992):

$$O_{m1} = \frac{1}{2\pi\nu \ln(\omega_{hi}/\omega_{lo})} \binom{N+m-1}{N}^{-1} \times \int_{\omega_{lo}}^{\omega_{hi}} \frac{d\omega}{\omega} \int_0^{2\pi} d\phi \frac{m^N}{W_m(\omega, \phi)} \tag{B.17}$$

with

$$W_m(\omega,\phi) = \frac{N!}{n_1!n_2!\ldots n_m!} \tag{B.18}$$

where ω_{hi} and ω_{lo} are the maxima and minima value for ω, $\nu = m_{\max} - 1$, N is the total number of events and $n_j = n_j(\omega,\phi)$ is the number of events that fall into bin j. I refer to Gregory & Loredo (1992) for the full demonstration of these equations.

B.2.5.3 Estimation of the frequency

Assuming the truth for a particular model, M_m, Bayes' theorem, applied for the posterior distribution for the frequency is (Gregory & Loredo (1992), see the article for a full description of the calculation):

$$\begin{aligned} p(\omega \mid D, M_m) &= p(\omega \mid M_m)\frac{p(D|\omega,M_m)}{p(D|M_m)} \\ &= \frac{C}{\omega}\int d\phi \frac{1}{W_m(\omega,\phi)} \end{aligned} \tag{B.19}$$

where C is a normalization constant:

$$C = \left[\int_{\omega_{lo}}^{\omega_{hi}} \frac{d\omega}{\omega}\int_0^{2\pi} d\phi \frac{1}{W_m(\omega,\phi)}\right]^{-1} \tag{B.20}$$

The best frequency can be found, for example, by calculating the posterior mean for ω:

$$\langle\omega\rangle = \int d\omega\omega p(\omega \mid D, M_m) \tag{B.21}$$

The standard deviation is given by:

$$\langle\sigma_\omega\rangle = \sqrt{\langle\omega^2\rangle - \langle\omega\rangle^2} \tag{B.22}$$

B.3 Application on simulated data

I simulated a time serie containing 1280 events, whose light curve is represented in fig B.1. The signal has a periodicity of 10 sec and the data have been simulated such that the pulse profile is described by 10 bins.

I calculated the posterior probability for the period using equation B.19. The tested period goes from 8 to 12 sec using 100 steps and the posital phase, $o = \phi/(2\pi)$, runs from 0 to 1 in 10 steps. I consider a class of models M_m to describe the data, where m, the number of bins is going from 2 to 20. The results are shown in Fig. B.2. The mean

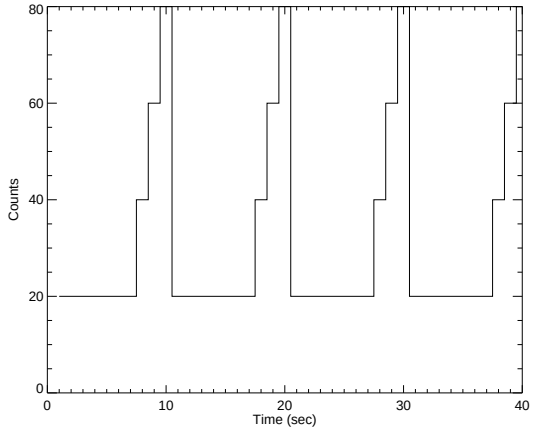

Figure B.1: Light curve of the simulated time serie.

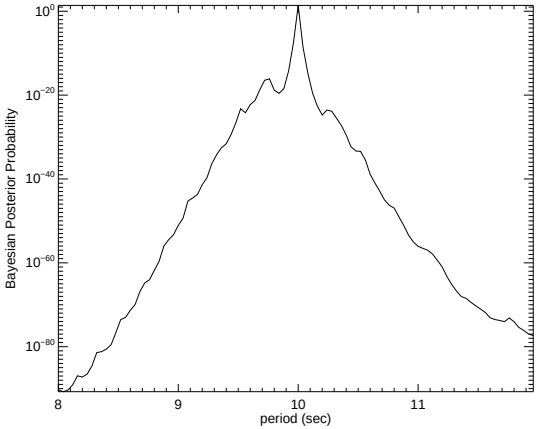

Figure B.2: Bayesian posterior probability for the tested periods.

value for the posterior probability of the period, P, $\langle P \rangle = 10$ sec (with an associated error $\sigma_P = 1.35 \times 10^{-6}$).

Fig. B.3 shows the odds ratio (eq. B.9) as a function of the number of bins, with a maximum at 10 bins. Thanks to these odds ratio, the algorithm find automatically which is the best number number of bins that describe the pulse profile.

I then calculated the posterior probability for data containg 1280 events (4 periods),

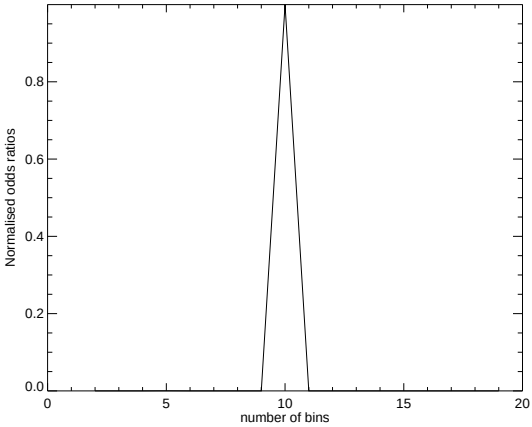

Figure B.3: Odds ratios as a function of the number of bins values.

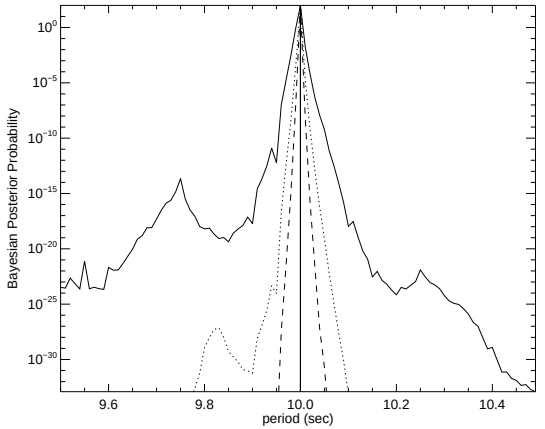

Figure B.4: Bayesian posterior probability for data containg 1280 events (full line), 1920 events (dotted line) and 2560 events (dashed line).

1920 events (6 periods) and 2560 events (8 periods). Results are shown in Fig. B.4. The mean value for the posterior probability of the period is $\langle P \rangle \sim 10$ sec with an associated error $\sigma_P = 8.99 \times 10^{-4}$, $\sigma_P = 1.69 \times 10^{-5}$ and $\sigma_P = 2.67 \times 10^{-7}$ for the 3 event sets, repectively. This indicates that when the statistics increases, the uncertainty associated with the posterior probability decreases rapidly.

Bibliography

Arnaud, K. A. 1996, in ASP Conf. Ser. 101: Astronomical Data Analysis Software and Systems V, 17

Binney, J. & Tremaine, S. 1987, Galactic dynamics (Princeton, NJ, Princeton University Press, 1987, 747 p.)

Blair, W. P. & Long, K. S. 1997a, ApJS, 108, 261

—. 1997b, ApJS, 108, 261

Bradt, H. V. D., Ohashi, T., & Pounds, K. A. 1992, ARA&A, 30, 391

Bresolin, F., Gieren, W., Kudritzki, R., Pietrzyński, G., & Przybilla, N. 2002, ApJ, 567, 277

Breysacher, J., Azzopardi, M., Testor, G., & Muratorio, G. 1997, A&A, 326, 976

Carignan, C. 1985, ApJS, 58, 107

Carpano, S., Wilms, J., Schirmer, M., & Kendziorra, E. 2004, Memorie della Societa Astronomica Italiana, 75, 486

—. 2005, A&A, 443, 103

Charles, P. A. & Seward, F. D. 1995, Exploring the X-ray universe (Cambridge, New York: Cambridge University Press)

Colbert, E. J. M., Heckman, T. M., Ptak, A. F., Strickland, D. K., & Weaver, K. A. 2004, ApJ, 602, 231

Costa, E., Frontera, F., Heise, J., et al. 1997, Nature, 387, 783

Cote, S., Freeman, K. C., Carignan, C., & Quinn, P. J. 1997, AJ, 114, 1313

Crawford, D. F., Jauncey, D. L., & Murdoch, H. S. 1970, ApJ, 162, 405

Davidson, K. & Ostriker, J. P. 1973, ApJ, 179, 585

Davies, S. R. 1990, MNRAS, 244, 93

de Vaucouleurs, G., de Vaucouleurs, A., & Corwin, HG Jr., e. a. 1991, Springer-Verlag, New York

Deharveng, L., Caplan, J., Lequeux, J., et al. 1988a, A&AS, 73, 407

—. 1988b, A&AS, 73, 407

Dickey, J. M. & Lockman, F. J. 1990, ARA&A, 28, 215

Dubus, G., Charles, P. A., Long, K. S., Hakala, P. J., & Kuulkers, E. 1999, MNRAS, 302, 731

Duric, N., Gordon, S. M., Goss, W. M., Viallefond, F., & Lacey, C. 1995, ApJ, 445, 173

Ehle, M., Breitfellner, M., Gonzalez Riestra, R., et al. 2004a, XMM-Newton Users' Handbook, Issue 2.2

Ehle, M., Pollock, A., Talavera, A., et al. 2004b, User's Guide to the XMM-Newton Science Analysis System

ESA. 1999, ESA Bulletin Number 100 (ESA Publications Division, ESTEC, Noordwijk, The Netherlands)

—. 2004, ESA's report to the 35th COSPAR meeting (ESA Publications Division, ESTEC, Noordwijk, The Netherlands)

Fabian, A. C., Pounds, K. A., & Blandford, R. D. 2004, Frontiers of X-ray astronomy (Cambridge University Press, UK)

Finger, M. H., Koh, D. T., Nelson, R. W., et al. 1996, Nature, 381, 291

Forman, W., Jones, C., Cominsky, L., et al. 1978, ApJS, 38, 357

Freedman, W. L., Madore, B. F., Gibson, B. K., et al. 2001, ApJ, 553, 47

Freedman, W. L., Madore, B. F., Hawley, S. L., et al. 1992, ApJ, 396, 80

Giacconi, R. & Gursky, H. 1974, X-ray astronomy (D. Reidel Publishing company, Dordrecht)

Giacconi, R., Gursky, H., Paolini, F. R., & Rossi, B. B. 1962, Physical Review Letters, 9, 439

Gieren, W., Pietrzyński, G., Soszyński, I., et al. 2005, ApJ, 628, 695

Graham, J. A. 1984, AJ, 89, 1332

Gregory, P. C. 1999, ApJ, 520, 361

—. 2005, Bayesian logical data analysis for the physical sciences (Cambridge University Press, UK)

Gregory, P. C. & Loredo, T. J. 1992, ApJ, 398, 146

Greiner, J., Di Stefano, R., Kong, A., & Primini, F. 2004, ApJ, 610, 261

Grimm, H.-J., Gilfanov, M., & Sunyaev, R. 2002, A&A, 391, 923

Guainazzi, M., Gabriel, C., Altieri, B., et al. 2004, XMM-SOC-USR-TN-0009 Issue 1.1

Haberl, F., Filipović, M. D., Pietsch, W., & Kahabka, P. 2000, A&AS, 142, 41

Haberl, F. & Pietsch, W. 1999, A&AS, 139, 277

Holt, S. S., Schlegel, E. M., Hwang, U., & Petre, R. 2003, ApJ, 588, 792

Humphrey, P. J. & Buote, D. A. 2004, ApJ, 612, 848

Humphreys, R. M. & Graham, J. A. 1986, AJ, 91, 522

Hutchings, J. B. & Cowley, A. P. 1991, in The Magellanic Clouds, IAU Symp. 148 (Kluwer Academic Publishers, Dordrecht), 285

Iovino, A., Clowes, R., & Shaver, P. 1996, A&AS, 119, 265

Itoh, H. & Masai, K. 1989, MNRAS, 236, 885

Jenkins, L. P., Roberts, T. P., Warwick, R. S., Kilgard, R. E., & Ward, M. J. 2004, MNRAS, 349, 404

—. 2005, MNRAS, 357, 401

Kaaret, P. 2002, ApJ, 578, 114

Kahabka, P., Pietsch, W., & Hasinger, G. 1994, A&A, 288, 538

Kalogera, V. & Baym, G. 1996, ApJ, 470, L61

Kendziorra, E., Wilms, J., Lamer, G., & Staubert, R. 2001, in New Visions of the X-ray Universe in the XMM-Newton and Chandra Era, ed. F. Jansen et al., ESA SP-488, ESA Publications, Noordwijk, in press

Kilgard, R. E., Cowan, J. J., Garcia, M. R., et al. 2005, ApJS, 159, 214

Kong, A. K. H. & Di Stefano, R. 2003a, ApJ, 590, L13

—. 2003b, ApJ, 590, L13

Kuntz, K. D., Snowden, S. L., Pence, W. D., & Mukai, K. 2003, ApJ, 588, 264

Lamb, F. K., Pethick, C. J., & Pines, D. 1973, ApJ, 184, 271

Lampton, M., Margon, B., & Bowyer, S. 1976, ApJ, 208, 177

Leahy, D. A., Darbro, W., Elsner, R. F., et al. 1983, ApJ, 266, 160

Lewin, W. H. G., van Paradijs, J., & van den Heuvel, E. P. J. 1995, X-ray binaries (Cambridge Astrophysics Series, Cambridge, MA: Cambridge University Press, edited by Lewin, Walter H.G.; Van Paradijs, Jan; Van den Heuvel, Edward P.J.)

Liu, J.-F. & Bregman, J. N. 2005, ApJS, 157, 59

Liu, Q. Z., van Paradijs, J., & van den Heuvel, E. P. J. 2000, A&AS, 147, 25

—. 2001, A&A, 368, 1021

Lomb, N. R. 1976, Ap&SS, 39, 447

Long, K. S., Helfand, D. J., & Grabelsky, D. A. 1981, ApJ, 248, 925

Longair, M. S. 1992, High energy astrophysics. Vol.1: Particles, photons and their detection (Cambridge: Cambridge University Press, 1992, 2nd ed.)

Loredo, T. J. 1990, From Laplace To SN 1987A: Bayesian Inference In Astrophysics (P. F. Fougere (ed), Kluwer Academic Publishers Dordrecht), 81–142

Maccacaro, T., Gioia, I. M., Wolter, A., Zamorani, G., & Stocke, J. T. 1988, ApJ, 326, 680

Makishima, K., Kubota, A., Mizuno, T., et al. 2000, ApJ, 535, 632

Marston, A. P., Elmegreen, D., Elmegreen, B., et al. 1995, ApJ, 438, 663

Mészáros, P., Nagel, W., & Ventura, J. 1980, ApJ, 238, 1066

Mitsuda, K., Inoue, H., Koyama, K., et al. 1984, PASJ, 36, 741

Nagel, W. 1981a, ApJ, 251, 288

—. 1981b, ApJ, 251, 278

Nowak, M. A., Wilms, J., Heindl, W. A., et al. 2001, MNRAS, 320, 316

Pannuti, T. G., Duric, N., Lacey, C. K., et al. 2000a, ApJ, 544, 780

—. 2000b, ApJ, 544, 780

Parmar, A. N., Kahabka, P., Hartmann, H. W., et al. 1997, A&A, 323, L33

Parmar, A. N., Kahabka, P., Hartmann, H. W., Heise, J., & Taylor, B. G. 1998, A&A, 332, 199

Parmar, A. N., Sidoli, L., Oosterbroek, T., et al. 2001, A&A, 368, 420

Payne, J. L., Filipović, M. D., Pannuti, T. G., et al. 2004a, A&A, 425, 443

—. 2004b, A&A, 425, 443

Pietrzyński, G., Gieren, W., Fouqué, P., & Pont, F. 2001a, A&A, 371, 497

—. 2001b, A&A, 371, 497

—. 2002a, AJ, 123, 789

Pietrzyński, G., Gieren, W., & Udalski, A. 2002b, PASP, 114, 298

Pietsch, W., Freyberg, M., & Haberl, F. 2005, A&A, 434, 483

Pietsch, W., Misanovic, Z., Haberl, F., et al. 2004, A&A, 426, 11

Prestwich, A. H., Irwin, J. A., Kilgard, R. E., et al. 2003, ApJ, 595, 719

Pringle, J. E. & Rees, M. J. 1972, A&A, 21, 1

Read, A. M. & Pietsch, W. 2001, A&A, 373, 473

Rhoades, C. E. & Ruffini, R. 1974, Physical Review Letters, 32, 324

Rybicki, G. B. & Lightman, A. P. 1979, Radiative processes in astrophysics (New York, Wiley-Interscience, 1979. 393 p.)

Sasaki, M., Haberl, F., & Pietsch, W. 2000a, A&AS, 143, 391

—. 2000b, A&AS, 147, 75

Scargle, J. D. 1982, ApJ, 263, 835

Schild, H., Crowther, P. A., Abbott, J. B., & Schmutz, W. 2003a, A&A, 397, 859

—. 2003b, A&A, 397, 859

Schild, H. & Testor, G. 1991, A&A, 243, 115

Schirmer, M., Erben, T., Schneider, P., et al. 2003, A&A, 407, 869

Schlegel, E. M. & Pannuti, T. G. 2003, AJ, 125, 3025

Shakura, N. I. & Sunyaev, R. A. 1973, A&A, 24, 337

Smith, R. K., Brickhouse, N. S., Liedahl, D. A., & Raymond, J. C. 2001, ApJ, 556, L91

Soffner, T., Mendez, R. H., Jacoby, G. H., et al. 1996a, A&A, 306, 9

—. 1996b, A&A, 306, 9

Soria, R. & Wu, K. 2003, A&A, 410, 53

Stephenson, F. R. & Green, D. A. 2002, Historical supernovae and their remnants, by F. Richard Stephenson and David A. Green. International series in astronomy and astrophysics, vol. 5. Oxford: Clarendon Press, 2002

Stetson, P. B. 1987, PASP, 99, 191

Strüder, L., Briel, U., Dennerl, K., et al. 2001, A&A, 365, L18

Supper, R., Hasinger, G., Pietsch, W., et al. 1997, A&A, 317, 328

Swartz, D. A., Ghosh, K. K., Suleimanov, V., Tennant, A. F., & Wu, K. 2002, ApJ, 574, 382

Terashima, Y. & Wilson, A. S. 2004, ApJ, 601, 735

Trinchieri, G. & Fabbiano, G. 1991, ApJ, 382, 82

Trinchieri, G., Fabbiano, G., & Peres, G. 1988, ApJ, 325, 531

Trudolyubov, S. & Priedhorsky, W. 2005, in X-Ray and Radio Connections (eds. L.O. Sjouwerman and K.K Dyer) Published electronically by NRAO, http://www.aoc.nrao.edu/events/xraydio Held 3-6 February 2004 in Santa Fe, New Mexico, USA

Trümper, J., Hasinger, G., Aschenbach, B., Braeuninger, H., & Briel, U. G. 1991, Nature, 349, 579

Tully, R. B. 1988, Nearby galaxies catalog (Cambridge and New York, Cambridge University Press, 1988, 221 p.)

Turner, M. J. L., Abbey, A., Arnaud, M., et al. 2001, A&A, 365, L27

Ueda, Y., Akiyama, M., Ohta, K., & Miyaji, T. 2003, ApJ, 598, 886

van den Heuvel, E. P. J. 1999, in Highlights in X-ray Astronomy, 57

van den Heuvel, E. P. J., Bhattacharya, D., Nomoto, K., & Rappaport, S. A. 1992, A&A, 262, 97

van der Heyden, K. J., Bleeker, J. A. M., & Kaastra, J. S. 2004, A&A, 421, 1031

van Paradijs, J. & Verbunt, F. 1984, in High Energy Transients in Astrophysics, AIP Conference Proceedings, 115, 49

Verbunt, F., Bunk, W. H., Ritter, H., & Pfeffermann, E. 1997, A&A, 327, 602

Wang, Q., Hamilton, T., Helfand, D. J., & Wu, X. 1991, ApJ, 374, 475

Wang, Y.-M. & Welter, G. L. 1981, A&A, 102, 97

Warner, B. 1995, Cataclysmic variable stars (Cambridge Astrophysics Series, Cambridge, New York: Cambridge University Press)

White, N. E., Kaluzienski, J. L., & Swank, J. H. 1984, in High Energy Transients in Astrophysics, AIP Conference Proceedings, 115, 31

Williams, B. F., Garcia, M. R., Kong, A. K. H., et al. 2004, ApJ, 609, 735

Wilms, J., Nowak, M. A., Pottschmidt, K., et al. 2001, MNRAS, 320, 327

Wolf, C. J. E. & Rayet, G. 1876, Comptes Rendus, 65, 292

Wood, K. S., Meekins, J. F., Yentis, D. J., et al. 1984, ApJS, 56, 507

Yokogawa, J., Imanishi, K., Tsujimoto, M., et al. 2000, ApJS, 128, 491

Zezas, A. & Fabbiano, G. 2002, ApJ, 577, 726

Acknowledgements

I should first of all like to thank Prof. Dr. Rüdiger Staubert for receiving me so kindly at the Institute, for giving me the opportunity to pursue this PhD thesis and for his good advices. I also wish to thank Dr. Eckhard Kendziorra for introducing me to the 'XMM-Newton world', for explaining the tools of data processing and for giving me so much excellent advice throughout the duration of my work.

A special thank you must go to Dr. Jörn Wilms who taught me a great deal about X-ray astronomy and data processing. I thank him particularly for dedicating so much time and energy to the realisation of this work, for giving me the tools and desire to continue to evolve.

I should also like to thank Mischa Schirmer for his nice collaboration and the rest of the Institute, including Prof. Dr. Andrea Santangelo, Prof. Dr. Klaus Werner, my office mate Ljuba, the old and the new students and PhD students, as well as the admins, for making me feel so welcome in the Institute and helping me directly or indirectly in bringing this work to fruition.

Next, I must thank my friend, Massimiliano, who has been so patient with me these last years. He has helped me enormously to handle a LINUX computer, has sacrificed many week-ends and evenings to allow me to work and has been a pillar of support during the more difficult moments.

Last but not least I must thank my family who have given me so much love and encouragement, in spite of the distance between us.

Curriculum Vitae

Personal data

18.05.1978	Born in Etterbeek (Brussels, Belgium). Nationality: Belgian.

Secondary School

09.1990–06.1996	Lycée Emile Jacqmain (Brussels). Main subjects: Greek-Latin + Mathematics.

University

09.1996–06.2000	Université Libre de Bruxelles. Major Subjects: Experimental Physics + Astrophysics. Degree: Graduate in Physical Science. Title of the Diploma Thesis: *Photometric observations of cataclysmic variables V795 Her, AH Her and DW UMa.*

Previous employments

10.2000–09.2001	Researcher at the Royal Observatory of Belgium (Brussels), working on: *The influence of the atmosphere on Earth rotation at semi-diurnal frequency.*
11.2001–09.2002	Young Graduate Trainee at the ESA (ESTEC, Noordwijk, The Netherlands). Title of the work: *Planetary Transit Detection with EDDINGTON. Optimal Filtering and Bayesian Maximum Likelihood Detection.*

PhD thesis

10.2002–12.2005	PhD thesis performed at the Institut für Astronomie und Astrophysik (IAAT, Universität Tübingen, Germany). Title: *X-ray properties of NGC 300 point sources detected with XMM-Newton, and their optical counterparts.* Supervisors: Priv. Doz. Dr. J. Wilms and Prof. Dr. R. Staubert.

Academic instructors:

J. Wilms, R. Staubert, K. Werner, A. Santangelo, M. Arnould, A. Jorissen., Y. Busegnies, M. Haelterman, P. Broekaert, F. Masin, P. Gaspard, J.M. Frère, M. Henneaux,

Ch. Schomblond, M. Mareschal, C. Leclercq-Willain, M. Herman, J. Sacton,
Ch. Joachain, R. Deltour, Ph. Boulanger, G. Wilquet, C. Vander Velde,
Ph. Vincke, F. Binon, N. Cerf, E. Kestemont, J. Liévin, Ph. Emplit, I. Stengers,
J.P. Gossez, L. Brenig, J. Doyen, L. Lemaire, H.D. Hurwitz, F. Buekenhout.